Layer-Specific Connectivity Analysis with High-Resolution Functional MRI in Human Brain

by

Yun Wang

A dissertation submitted to the Graduate Faculty of
Auburn University
in partial fulfillment of the
requirements for the Degree of
Doctor of Philosophy

Auburn, Alabama
December 10, 2016

Keywords: High-resolution fMRI, Layer, Functional Connectivity, Effective Connectivity, Blind Deconvolution, Granger Causality

Copyright 2016 by Yun Wang

Approved by

Gopikrishna Deshpande, Chair, Associate Professor, Department of Electrical & Computer Engineering
Thomas S. Denney Jr., Professor, Department of Electrical & Computer Engineering
Jeffrey Katz, Alumni Professor, Department of Psychology
Jennifer Robinson, Assistant Professor, Department of Psychology

Abstract

Functional magnetic resonance imaging (fMRI) has been increasingly used for understanding the human brain connectome. In this work, we utilized high-resolution fMRI to investigate the sensitivity of layer-specific connectivity methods, including functional connectivity (FC) and effective connectivity (EC), to connectional architecture at sub-millimeter spatial scale under different human brain states. The human neocortical graymatter contains cytoarchitectonically distinct layers, with notable differences in their structural connectivity with the rest of the brain. While this has traditionally been done using invasive techniques, recent improvements in the spatial resolution of anatomical and functional MRI may enable non-invasive investigation of the connectional architecture at the laminar level.

Before the connectivity analysis, we applied a surface-based laminar analysis pipeline to process high-resolution, sub-millimeter MRI data obtained at 7T, and to delineate different layers of the human cortex. Because of the inter-subject and spatial variability of the hemodynamic response function (HRF), we performed blind deconvolution of vertex-based fMRI data to obtain underlying later neural signals from all layers. We demonstrated that the post-deconvolution connectivity analysis in the latent neural space aligned more closely with the underlying anatomical connections compared to connectivity obtained from original fMRI data.

Using high-resolution resting state fMRI, we tested general hypotheses. First, given that functional connectivity is anchored and constrained by the structural connectome, we hypothesized that pathways between different layers, which have been shown to have a structural basis in

invasive studies must have higher functional (synchronized and undirected) connectivity inferred from layer-resolved fMRI. Second, unidirectional anatomical projections at the layer level, which support feedback and feedforward interactions must be inferred using effective (directional, time-lagged) connectivity derived from layer resolved fMRI.

We found these specific results in support of the first hypothesis: 1) FC between the entire thalamus and cortical layers I and VI was significantly stronger than between the thalamus and other layers. Further, FC between somatosensory thalamus (ventral posterolateral nucleus, VPL) and layers IV, VI of the primary somatosensory cortex were stronger than with other layers; 2) Inter-hemispheric cortico-cortical FC between homologous regions in superficial layers (layer I-III) was stronger compared to deep layers (layer V-VI). These findings are in agreement with structural connections inferred from previous invasive studies. These findings demonstrate for the first time that resting state fMRI is sensitive to structural connections between cortical layers, specifically in thalamocortical and cortico-cortical networks.

In order to test the second hypothesis, we propose an experimental and analysis framework, which enables noninvasive functional characterization of layer-specific cortical microcircuits. Specifically, we illustrate this framework by characterizing layer-specific directional functional pathways in the corticogeniculate network of the human visual system by obtaining sub-millimeter fMRI at 7T using a task that engages the magnocellular pathway between LGN and the primary visual cortex. Our results showed that: (i) center-surround inhibition in magnocellular neurons within LGN (lateral geniculate nucleus) is detectable using localized fMRI responses within LGN; (ii) feedforward (LGN→ Layers VI/IV, Layer IV→ Layer VI) and feedback (Layer VI→ LGN) functional pathways, known to exist from invasive animal studies, can be inferred using dynamic directional connectivity models of fMRI and could potentially explain the mechanism underlying

center-surround inhibition as well as gain control by Layer-VI in the human visual system. Our framework is domain-neutral, and could potentially be employed to investigate the layer-specific cortical microcircuits in other systems related to cognition, memory and language.

In summary, we demonstrate layer-specific connectivity analysis with high-resolution functional MRI obtained at 7T is a powerful non-invasive technique to unveil the connectional architecture at submillimeter spatial scale in human brain.

Acknowledgements

I would like to express my deepest gratitude to my advisor, Dr. Gopikrishna Deshpande, who gave me enormous guidance and inspiration during this research work. He taught me how to think critically and motivated me to conduct innovative scientific research. Moreover, he spent a lot of time on proofreading my papers and gave me excellent suggestions. I would like to thank Dr. Thomas Denney for his help and financial support with the task fMRI project. I would like to thank Dr. Jennifer Robinson for sharing high-resolution resting state fMRI data, and gave me extremely valuable suggestions. I thank Dr. Jeffrey Katz for his help with experimental design. Without the support, insightful suggestions from my PhD committee members, I would not have been able to complete this work.

Also, I would like to thank Dr. Salibi Nouha, who helped me optimize the multiband sequence on 7 Tesla scanner. I thank Dr. Ronald Beyers for his unlimited help with scanner problems. I really appreciate the help with MRI data analysis from my current lab member Sinan Zhao, and previous members: Kathik Ramakrishnan, Hao Jia, and Sereenath Kyathanahally. I would like to thank the department of Electrical Engineering for providing me with the graduate teaching assistant fellowship, since I would not be able to finish the education without the financial support.

I thank my parents and my big brother from my deep heart, who always give me unlimited support with my education. Here, I would like to thank my beloved husband, Tuo Shi. He is always there with me no matter what happens.

Table of contents

List of Figures

List of Tables

List of Abbreviations

BBR	Boundary-based Registration
BET	Brain Extraction Tool
BOLD	Blood Oxygen Level Dependent
cpd	Cycle per Degree
CSF	Cerebrospinal Fluid
DCM	Dynamic Causal Modeling
DGC	Dynamic Granger Causality
EC	Effective Connectivity
EPI	Echo Planar Imaging
FC	Functional Connectivity
fMRI	Functional Magnetic Resonance Imaging
FWHM	Full-Width at Half-Max
GC	Granger Causality
GLM	General Linear Model

HRF	Hemodynamic Response Function
iPAT	In-plane Phase-encode Acceleration Factor
LGN	Lateral Geniculate Nucleus
MB	Multiband
MRI	Magnetic Resonance Imaging
MNI	Montreal Neurological Institute
magnocellular LGN	Magnocellular Neurons of LGN
MVAR	Multivariate Vector Autoregressive Model
OFC	Orbitofrontal Cortex
PSF	Point Spread Function
PE	Parameter Estimate
TTP	Time-to-Peak
TR	Repetition Time
TE	Echo Time
3D	Three-Dimension
V1	Primary Visual Cortex

Chapter 1 Introduction

1.1 Basics of MRI and fMRI

Magnetic Resonance Imaging (MRI) has become a popular standard tool to map the brain structure, since it can provide high-resolution images with very good contrast between different types of brain tissues, e.g., gray matter, white matter. The mechanism behind MRI is: each nucleus of a hydrogen nucleus can be treated as a small magnet. When the subject lays inside a strong magnetic field of an MRI scanner, all hydrogen nuclei within the body will align with this magnetic field, however, with the application of a right radio frequency (RF) magnetic pulse, those nuclei will absorb energy and create a weak MR signal, which can be detected by the RF coils in the MRI system. MRI is a sensitive tool for detecting anatomical changes in the human brain. Recently, ultra-high field MRI has been increasingly demanded since it can provide increased signal noise ratio (SNR), and the high resolution shows more anatomical details at submillimeter level.

Functional magnetic resonance imaging (fMRI) has been widely used for the study of the human brain activity. It measures the blood oxygenation level dependent signal (BOLD) in the brain, discovered by Ogawa [1], an indirect way to measure the changes in blood flow in response to the neural activity. The BOLD is modulated by the local vascular distribution and the activation-induced hemodynamics changes. When neural activity increases in a specific region, the BOLD also increases correspondingly. Because it is a non-invasive safe technique that does not require any surgery, injection, or radiation, fMRI is becoming a popular and dominant tool to study the neural basis of the human cognition such as emotion, sensation, decision, etc., and help the psychiatrists and neurologists to investigate and diagnose related mental diseases.

Research over the last decade has established that BOLD contrast depends not only on blood oxygenation but also on CBF and CBV, representing a complex response controlled by several parameters. Despite this complexity, much progress has been made toward quantitatively elucidating various aspects of the BOLD signal and the way it relates to the hemodynamic and metabolic changes occurring in response to elevated neuronal activity [2]. The BOLD signal increases about 2 sec after the neural activity; it then reaches a plateau at about 5 – 8 sec. It will plateau if the neural activity continues. Once the neural activity stops, the signal returns to baseline 8 to 11 sec later (Figure 1.1). Finally, a transient change referred to as the undershot can be observed. Maximal variance is observed between subjects and minimal variance between scans of the same subject [3]. The change in the MR signal from neuronal activity is called the hemodynamic response. However, within subject variance increases when comparing several areas – i.e. the shape of the hemodynamic response is influenced by the vasculature and the task and these effects differ from one area to the other.

The spatial resolution of an fMRI study refers to how well it discriminates between nearby locations. It is measured by the size of voxels, as in MRI. A voxel is a three-dimensional rectangular cuboid, whose dimensions are set by the slice thickness, the area of a slice, and the grid imposed on the slice by the scanning process. Full-brain studies use larger voxels, while those that focus on specific regions of interest typically use smaller sizes. Sizes range from 4 to 5 mm to 1 mm. smaller voxels contain fewer neurons on average, incorporate less blood flow, and hence have less signal than larger voxels. Smaller voxels also take longer to scan, since scanning time directly rises with the number of voxels per slice and the number of slices. This can lead both to discomfort for the subject inside the scanner and to loss of the magnetization signal. A voxel typically contains a few million neurons and tens of billions of synapses with the actual number

depending on voxel size and the area of the brain being imaged. Temporal resolution is the smallest time period of neural activity reliably separated out by fMRI. One element deciding this is the sampling time, the TR, such as 1 or 2 seconds. FMRI has a typically poor resolution in general.

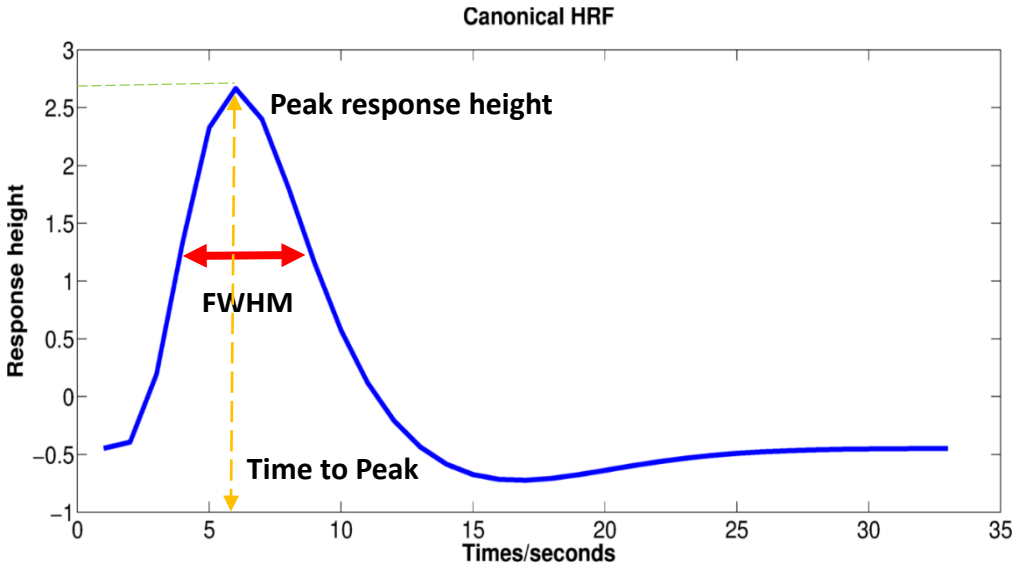

Figure 1.1 *Canonical Hemodynamic response.*

1.2 Columnar Organization of the Cerebral Cortex

The cerebral cortex is the outer sheer layer of neural tissues in the brain, composed of gray matter – the cell bodies and capillaries. Around two-thirds of the cerebral cortex is folded. A fold is called gyrus, and a fissure is called a sulcus. The most recently developed part of cerebral cortex is termed neocortex, which can be differentiated into six layers. Those neurons in different layers are vertically connected, forming cortical columns. Cortical columns represent a basic unit of computation, which consists of a cluster of neurons with similar features spanning from the pial surface to the white surface [4]. The Laminar organization in cortical columns is its most prominent anatomical characteristics. Physiological and anatomical studies have found that each layer

contains different types of cells, and has different connection patterns with other layers under dissimilar brain states in cortical columns [4]–[15].

The thickness of cerebral cortex ranges from about 2 mm to about 4 mm. Functional columns extend through the entire depth of the cortex, and is a fraction of 1 mm in diameter. Layer organization shows the following general tendencies. The six layers can be can be classified into three categories: superficial layers (layer I-III), middle layer (IV), and deep layers (V-VI).

The superficial layers consist of layers I to III. The superficial layers are the primary origin and termination of intracortical connections, which are either associational (i.e., with other areas of the same hemisphere), or commissural (i.e., connections to the opposite hemisphere, primarily through the corpus callosum). The superficial portion of the cortex is highly developed in humans and permits communication between one portion of the cortex and other regions. The middle layer, layer IV, receives thalamocortical connections, especially from the specific thalamic nuclei. This is most prominent in the primary sensory cortices. The deep layers, Layer V and VI, are primary connections between cerebral cortex and subcortical regions. The cortical layers are not simply stacked one over the other; there exists characteristic connections between different layers and neuronal types, which span all the thickness of the cortex.

Our knowledge about cortical laminar-specific connections is mostly derived from invasive studies including histology, anatomical tract tracing, electrophysiology, and lesion methods [5], [6], [9], [10], [16], [17], given that non-invasive modalities such as functional magnetic resonance imaging (fMRI) have typically lacked the resolution to resolve layer-specific differences.

It is essential and urgent to explore and investigate the laminar connectional architectures for neuronal computations. However, the efficiency of those invasive methods is pretty low.

Because those methods restricted to a small region where the cortex is flat. Therefore, only a few sites can been simultaneously recorded and investigated in the brain, and it is not possible to study the laminar connectional architecture over the folded cortex area.

1.3 Motivation

Recent developments in high-field MRI have enabled the possibility to investigate fMRI signal and functional architecture in human brain at submillimeter resolution [18]–[20]. High-field MRI (7T scanner) are capable of achieving higher signal to noise ratio than lower-field scanner, e.g., 3T scanner, and higher spatial resolution. Studies have shown that high-resolution fMRI can noninvasively map the spatial patterns of orientation columns within visual cortex, indicating the specificity of hemodynamic response in cortical columns [21]. Subsequently, the fMRI activation was shown to change as a function of laminar depth [22]–[25]. The laminar fMRI analysis can improve our understanding of cortical activity at laminar level and how different layers connect in cortical columns ,e.g., the top-down activity during the perceptual processing [26], [27]. Moreover, The cortical layers can be resolved and constructed as transvers that are perpendicular to each other. In addition, reliable methods have been developed to obtain cortical parcellation in the native space of individual subjects [28]–[32]. Laminar fMRI can improve our understanding of cortical spatial activation in task-fMRI studies [24]–[26], [33]–[36].

However, to date, layer-specific connectional architecture has not been explored with laminar fMRI, since many technical challenges need to be surmounted in order to examine the fMRI signal as well as the associated connectional architecture at the laminar level.

In this dissertation, our motivation is to investigate whether popular connectivity methods for investigating the connectome of the brain, such as functional connectivity and effective connectivity, are sensitive to layer-specific connectional architecture using high-resolution laminar fMRI.

1.4 Organization of This Dissertation

The first chapter gives some introduction about relevant background knowledge about MRI, fMRI, the columnar organization of human cerebral cortex, and our motivation for this dissertation. In chapter 2, we explained the general methods used commonly in chapter 3 and chapter 4 of this dissertation, including procedures of fMRI preprocessing, cortical surface reconstruction, and blind deconvolution.

In chapter 3, we investigated whether resting state functional connectivity (FC) is sensitive to layer-specific connectional architecture with high-resolution fMRI. Previous invasive studies indicate that human neocortical graymatter contains cytoarchitectonically distinct layers, with notable differences in their structural connectivity with the rest of the brain. Given recent improvements in the spatial resolution of anatomical and functional magnetic resonance imaging (fMRI), we hypothesize that resting-state functional connectivity (FC) derived from fMRI is sensitive to layer-specific connectional architecture. Using sub-millimeter resting-state fMRI data obtained at 7T, we found that: 1) FC between the thalamus and cortical layers I and VI was significantly stronger than between the thalamus and other layers; 2) Inter-hemispheric cortico-cortical FC between homologous regions in superficial layers (layer I-III) was stronger compared to deep layers (layer V-VI). These findings are in agreement with structural connections inferred

from previous invasive studies. Our results demonstrate for the first time that resting state fMRI is sensitive to structural connections between cortical layers, specifically in thalamocortical and cortico-cortical networks.

In chapter 4, we propose an experimental and analysis framework, which enables noninvasive functional characterization of layer-specific cortical microcircuits. Specifically, we illustrate this framework by characterizing layer-specific functional pathways in the corticogeniculate network of the human visual system by obtaining sub-millimeter fMRI at 7T using a task that engages the magnocellular pathway between LGN and the primary visual cortex. Our results showed that: (i) center-surround inhibition in magnocellular neurons within LGN (lateral geniculate nucleus) is detectable using localized fMRI responses within LGN; (ii) feedforward (LGN→ Layers VI/IV, Layer IV→ Layer VI) and feedback (Layer-VI→LGN) functional pathways, known to exist from invasive animal studies, can be inferred using dynamic directional connectivity models of fMRI and could potentially explain the mechanism underlying center-surround inhibition as well as gain control by Layer-VI in the human visual system. Our framework is domain-neutral, and could potentially be employed to investigate the layer-specific cortical microcircuits in other systems related to cognition, memory and language. Chapter 5 contains concluding remarks.

Chapter 2 General Data Analysis Methods

This chapter contains general methods that are used commonly in the next few chapters, including some procedures of functional MRI preprocessing, cortical surface reconstructions, and deconvolution.

2.1 FMRI Data Pre-processing

Just as a movie shoot outside the stage, requires cutting and editing before the release in the cinema, MRI data requires some preprocessing operations before the analysis of the data. A few software packages, e.g. Statistical Parametric Mapping (http://www.fil.ion.ucl.ac.uk/spm/) – SPM, FMRIB Software Library (FSL)[37], are very popular and used in this dissertation to preprocess our resting-state or task fMRI data. In Chapter 3, we used SPM toolbox to preprocess fMRI data, and in chapter 4, FSL was used. Each has its own advantages and limitation.

First, slice timing correction is generally performed for typical fMRI. MRI uses echo planar imaging (EPI), in which a three-dimensional is built up from a series of 2D slices. The slices are acquired in an interleaved order in this dissertation (every other slice is acquired sequentially, e.g., 1, 3, 5, 7…..2, 4, 6, 8…..). The 2D acquisition represents the data of different parts of image are acquired systematically at different time points. Therefore, it is very common to perform slice timing. The popular approach to slice time correction is choosing a reference slice (the middle slice usually, but any slice can be used) and then interpolating the fMRI data in all other slices to match the timing of the reference one. This can address the timing acquisition mismatch between different slices [38], [39]. In chapter 3, we applied this typical slice timing technique to our resting state fMRI data because of 3 seconds of TR. But, fast TR with multiband sequences (simultaneous

acquisition of multiple slices) reduces the need for slice timing correction since the difference of slice acquisition time is much smaller than typical fMRI acquisition time. In chapter 4, the TR of our task fMRI data is 1.5 second with multiband factor 3. Therefore, we chosen not to correct slice timing in the preprocessing for task fMRI data [40].

Second, motion correction (realignment) is always an important step in the preprocessing of any fMRI data sets. Subjects always move their head in the scanner (e.g., due to wallowing, or task caused movement), and these motions can lead to disruptive effects on fMRI data. The standard motion correction techniques are designed to correct those wholesome movements of the data, by realigning all other images to a single reference image. Motion correction algorithms, can be generally described with a rigid body transformation, which use a within-modality cost function. The cost function should be sensitive to the correlation of voxel intensities between a target image and the reference image. In SPM, the least-square cost function is used to measure the similarity [41], and in FSL, normalized correlation ratio (named MCFLIRT in FSL) is calculated to describe the linear relationship between voxel intensities in two different images [37], [42].

Third, frequencies in fMRI data are generally considered as noise when they are very low frequency bands (<0.01Hz). The extremely low frequency bands result from scanner drifts, coin interferences or slow metabolic oscillations such as heartbeat. Therefore, those low frequencies and slow drifts are needed to remove from every voxel of fMRI data with a high-pass filter.

To mention here, spatial smoothing and spatial normalization were not performed. Spatial smoothing negates the advantages gained by smaller voxels sizes. Also, spatial smoothing is employed in traditional general linear model based activation analysis in order to satisfy the assumptions of random field theory. We did not perform those kinds of analysis and hence found it unnecessary to spatially smooth the data. Also, the Freesurfer analysis pipeline (details in next

part of this chapter) enables individual-specific cortical parcellation from which we extracted the time series used in the analysis. Therefore, we found that spatially normalizing the data into a common space and incurring the costs of blurring and registration errors associated with such a procedure was unnecessary and may be counter-productive for the small voxel size we had and the type of analysis we planned.

2.2 Automated Cortical Surface Reconstruction

To enable the investigation of the connectional architecture at columnar and laminar level with MRI technique, an accurate and explicit model of cortical surface in individual subjects is a radical factor. In this dissertation, we used FreeSurfer [43] (http://freesurfer.net/), which includes a set of tools providing functionality of automated cortical surface reconstruction, and cortical parcellation in individual space [44], [45].

The cortical surface reconstruction is a very complex procedure, which can be broken into thirty-one processing stages for fully automated reconstruction with FreeSurfer pipeline. To be simple, we can categorize those steps into three main parts. First, intensity normalization needs to be performed to correct image intensity variation of the same tissue, which is caused by the corruption of magnetic susceptibility artifacts and field inhomogeneities. Once with intensity-normalized image, the subsequent step is skull stripping. The second part is segmenting MRI volume into different tissue types, which is based on the geometric structure of gray/white matter interface. Finally, a surface tessellation is constructed by using triangles (a triangle is a polygon with three edges and three vertices) to represent the face, which separates voxels classified as white matter from other classified voxels, e.g., gray matter, CSF. Additional deformation will produce a smoothed version of white/gray matter interface and pial surface. In this dissertation,

we call the white/gray matter interface as white matter surface. More detailed information can be found [31], [44]–[46].

However, this standard pipeline conforms the MRI data to an isotropic resolution of $1mm^3$. Because our MRI data had an isotropic resolution less than $1mm^3$ in this dissertation, we applied Lüsebrink's method [47] to process our $0.6mm^3$ isotropic resolution data. This method avoids downsampling high-resolution MRI data through software modification of FreeSurfer's standard processing pipeline. And eventually, we reconstructed white matter surface and pial surface based on original MRI resolution of $0.6mm^3$. The surfaces generated by FreeSurfer are represented in the form of triangular meshes, and each triangle has three vertices. Each vertex on the surface was associated with multiple geometry features: mean curvature of the cortical surface, mean curvature of the inflated cortical surface, and average convexity of the cortical surface. Also, a set of 3D coordinates of these surfaces gives position of the vertices.

Once we obtained the white matter and pial surfaces (Figure 2.1), the laminar profiles were delineated within the cortical gray matter. They were constructed at fixed relative distance between the white matter and pial surfaces, determined from the thickness map [24]. The position of each vertex on intermediate surfaces depends on the position of the correponding vertex on the white matter surface. This method of reconstructing intermediate laminar surfaces is called equidistant laminae [24], [25], [48], [49]. We adpoted this method in Chapter 3 and chapter 4 for surface-based laminar analysis.

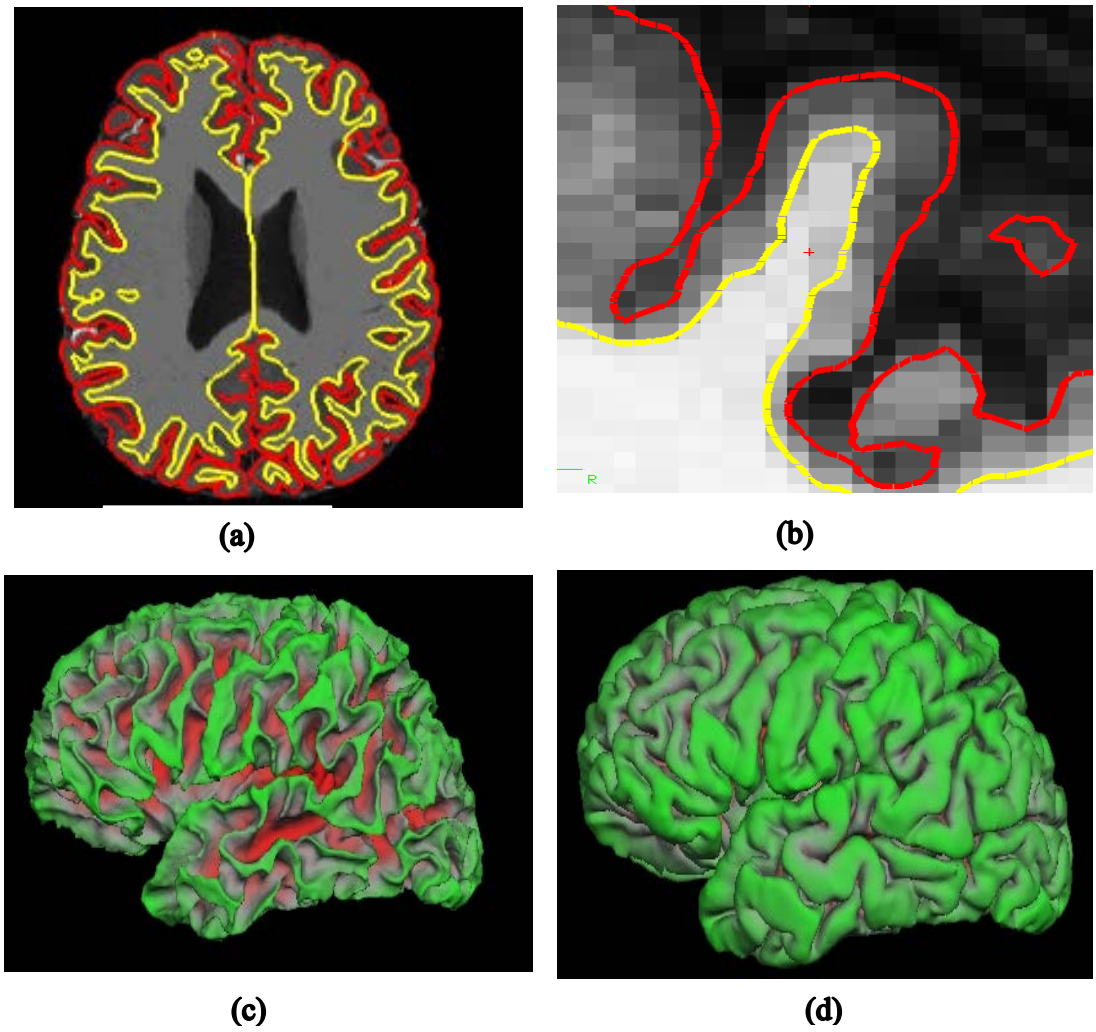

Figure 2.1. *(a) White/Gray matter interface(yellow) and Gray/Pial interface(red);(b) thickness between two boundaries (c) White matter surface, green represents gyrus and red for sulcus (d) Pial surface.*

Additionally, we need to align the fMRI volumes to those intermediate laminar surfaces in order to enable the analysis of laminar fMRI signal. Gray/white matter boundary in the EPI volume is easily identified automatically. We employed a method called boundary-based registration (BBR) [50] in this dissertation. It identified the interface between gray matter and white matter in the EPI data and then calculated a 12 degrees of freedom affine transformation, which registers the interface in EPI data to the corresponding surface reconstruction from the anatomical data. After the registration, the results were visually inspected for each subject and manually edited, if needed [50].

2.3 Blind Deconvolution

After extracting raw BOLD signal, blind deconvolution is performed to recover the truly latent neuronal signal, because BOLD signal is not a direct measure of neural activity, instead it arises from the interaction of blood flow, blood volume, and blood oxygenation in response to changes in neuronal activity. Changes in blood flow are behind the actual timing of neuronal activity. Conventionally, BOLD signal can represented as a blurred and delayed version of neural signal. BOLD fMRI signal can be modeled as the result of the convolution of latent neural response and the Hemodynamic Response Function (HRF). Also, the HRF varies across brain regions as well as across individuals [3], [51]. Recent studies have shown the variability of hemodynamic response can be a confounding factor for connectivity analysis, since it is difficult to confidently infer connectivity from raw BOLD signal [52], [53]. In this dissertation, we feed our fMRI data into a certain blind deconvolution model to recover latent neuronal signal before any connectivity analysis. In chapter 3, we adopt Wu's method [54] to perform vertex by vertex blind deconvolution for our resting state data. In brief, this method models resting-state fMRI as spontaneous event-

related signal using point process, and estimate vertex-specific HRF using Weiner deconvolution (details in chapter 3). In chapter 4, We employed a recently validated framework based on the Cubature Kalman filter and smoother to invert a nonlinear hemodynamic model [55]. Even though this model is highly parameterized, recent research indicates that it does not overfit the data [56].

2.4 Brain Connectivity

In this dissertation, we employed different connectivity techniques – functional connectivity and effective connectivity, with our laminar fMRI data to investigate and verify those well-known layer-specific connections at submillimeter spatial resolution obtained at 7 Tesla MRI scanner.

Brain connectivity refers to the correlation between brain regions, and it can arise from a number of reasons (Figure 2.2).

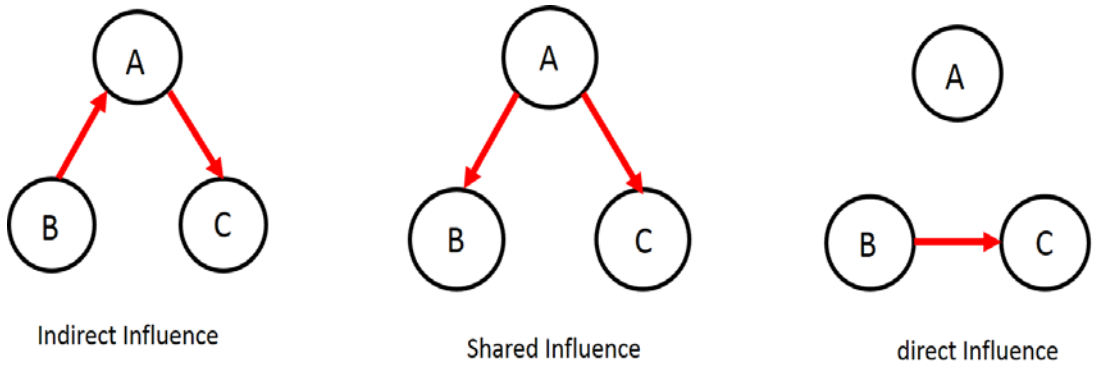

Figure 2.2. *Different ways of brain connectivity between two regions. Either indirect influence (left panel), shared influence (middle panel), or direct influence (right panel).*

Functional connectivity have been a very popular invasive method to analyze cortical circuit based on resting-state fMRI at both region and voxel level. Functional connectivity is defined as statistical dependency among different brain regions. However, the correlation may due

to various reasons, e.g., the correlation may result from stimulus-locked transients evoked by a common input or reflect the direct stimulus through synaptic connections, corresponding left and middle panel in Figure 2.2 [57], [58]. In chapter 3, we used functional connectivity method, which provides evidence regarding how activity covaries across layers or regions. Though the correlation does not necessarily imply a direct causal relation between regions, the presence of a correlation can definitely imply potential causal relationships.

In chapter 4, we employed an effective connectivity technique – dynamic granger causality (DGC), which corresponds to directed causal inference (Right Panel Figure 2.2). This is crucial to resolve the information flow between neuron populations.

Chapter 3 Resting State fMRI Connectivity is Sensitive to Layer-specific Connectional Architecture in Humans

3.1 Introduction

The most distinct feature of the mammalian cerebral cortex is its laminar structure, comprised of cortical columns. A cortical column is a unit of complex information processing. It consists of processing chains that overlap, linking multiple inputs to multiple other outputs[4]. A single column of cerebral cortical gray matter normally has six layers. Different layers in the column have distinct distribution and types of neurons as well as separate connections with other cortical and subcortical regions. Our knowledge about cortical laminar-specific connections is mostly derived from invasive studies including histology, anatomical tract tracing, electrophysiology, and lesion methods[5]–[10], given that non-invasive modalities such as magnetic resonance imaging (MRI), both anatomical and functional, have typically lacked the resolution to resolve layer-specific differences.

However, recent developments in ultra high field fMRI makes it feasible to examine the blood oxygen level dependent (BOLD) signal from cortical and subcortical regions with sub-millimeter resolution. With such resolution, cortical layers can be resolved reasonably although some amount of partial voluming still exists. In addition, reliable methods have been developed to obtain cortical parcellation in the native space of individual subjects[28]–[32]. In the recent past, laminar fMRI studies have investigated the spatial sensitivity of high-field fMRI to the neuronal

response at the submillimeter level[22], [24]–[26], [34], [36], [59]–[62], primarily using activation paradigms[24]–[26], [33]–[36]. The sensitivity of laminar fMRI has enabled us to understand the columnar profile of cortical activation at a finer spatial scale in the cerebral cortex. However, these investigations were only in the context of laminar fMRI activation (not resting state) within specific brain regions for specific stimuli (example: primary visual cortex with visual stimuli), most often achieved with partial brain coverage (unlike whole brain coverage used in conventional resting state fMRI studies) at ultra-high fields (7T for humans and >7T in case of animal studies).

One popular noninvasive method of analyzing cortical circuits at the voxel-level is functional connectivity based on resting state fMRI [63]. Resting state functional connectivity (FC) has been shown to be sensitive to alterations in neural circuits in various mental disorders [64]–[69] as well as correlated with behavioral performance in healthy individuals [70]–[72]. Recent literature employing resting state fMRI based characterization of the human brain's functional connectome suggests that resting state fMRI is grounded in underlying anatomical connections[73]–[76]. For example, simulations have shown that spatially distinct functional networks emerge in resting state data when they are constrained by the structural connectome[77], [78]. The close correspondence between functional and structural connectivity has also been confirmed with fMRI and diffusion tensor imaging (DTI) data[79]. This has been further confirmed in case reports of deficient inter-hemispheric functional connectivity in subjects with complete agenesis of the corpus callosum[80]. However, it is noteworthy that resting state functional connectivity can be sensitive to multi-synaptic interactions, and hence, regions that are not directly connected structurally could still be functionally connected. These data suggest that if two regions have a direct structural connection, then they should also be functionally connected, but the opposite may not be true. Consequently, one could expect a strong functional connection

between regions that are also directly connected structurally. In this work, our objective is to extend this concept from mesoscale connections between brain regions to rather microscale connections between different cortical layers in these regions. Attempts to do so have been scarce in the literature. Below, we present past few attempts in this direction. Layer-specific connections between the primary visual cortex layers II/III and middle temporal area layer IV were detected with high-resolution resting-state fMRI through functional connectivity analysis[61]. The default mode network under resting state was clearly seen across six layers by seed-based functional connectivity analysis after removing depth-dependent physiological noise [81]. Also, a recent study showed the existence of temporal correlation of resting state hemodynamic signals derived from optical imaging at submillimeter column scale in the visual cortex [82]. These studies suggest that functional connectivity could be a potentially useful method to investigate the laminar connectional architecture at the functional level. However, it is yet unclear whether resting-state functional connectivity (FC) is in fact stronger along structural pathways that connect different layers of brain regions compared to say, other possible connections between layers that do not have a direct structural projection between them. In order to test these possibilities, many technical challenges need to be surmounted that we discuss below in order to provide motivation for the methodological choices we have made.

The major limitation of fMRI is that it is an indirect measure of neural activity because it measures changes in blood oxygenation level that is modulated by the local vascular distribution (vessel size) and the activation-induced hemodynamics changes [24]. BOLD fMRI signal can be modeled as the result of the convolution of a latent neural response and the Hemodynamic Response Function (HRF). At the voxel-level, the HRF varies across brain regions as well as across individuals [3], [51]. Some animal and human MRI studies at high-field have shown that the

response height and time-to-peak (TTP) of the HRF varies with cortical depth [25], [83]–[87]. It was shown that the deep layers have faster and narrower hemodynamic response compared to the superficial layers. Also, at the laminar level, gradient-echo BOLD signal has relatively poor laminar specificity, because it is more sensitive to larger vessels [88]. However, a recent investigation of the spatial point spread function (PSF) for the BOLD response showed that the laminar PSF of the gradient-echo BOLD signal had a "flat-tail" characteristic across layers, with the tail running to the pial surface [89]. This indicates that lower layers contribute signal to any given layer in gradient-echo BOLD. While spin echo BOLD may provide better spatial laminar specificity, one may lose sensitivity to the BOLD effect when using a spin echo. Investigations into the laminar specificity of BOLD as well as HRF variability across cortical layers have invariably used task-based paradigms and cannot be readily generalized to resting state given that neurovascular coupling likely operates under a different regime in resting state (see extension of Buxton's balloon model to resting state conditions in [90]).

Many studies have characterized the effect of HRF variability across regions and subjects [3], [91], as well as the impact of HRF variability across layers [25], [83]–[87]. However, all of these studies investigated the impact of HRF variability in the context of detecting activation (and not in the context of characterizing functional connectivity). And, inter-subject and spatial variability of the HRF could potentially give rise to a scenario wherein the BOLD fMRI time series from any given two regions are synchronized while the underlying neural response is not, thus giving high correlation while the true correlation between latent neural variables is low. The opposite scenario, wherein the underlying neuronal variables are synchronized while the BOLD fMRI time series are not, is also equally possible (see supplementary Figure S1 for illustration of these scenarios). Therefore, we need to extract the underlying latent neural response to get reliable

estimates of FC between layers of different regions. The readers are referred to Rangaprakash et al for more details on the effects of HRF variability on functional connectivity[92].

In this study, we applied a surface-based laminar analysis pipeline available in FreeSurfer (https://surfer.nmr.mgh.harvard.edu/) to process high-resolution anatomical data with a 0.6mm isotropic resolution and to delineate the six layers of the cortex [45], [47]. To investigate whether FC is sensitive to layer-specific connectional architecture, we examined this aspect with high-resolution resting state fMRI data (voxels with 0.85mm in-plane resolution) obtained at 7T. A simple blind deconvolution technique [93] was used to obtain the latent neural signals for each layer. Specifically, we tested the following hypotheses thalamocortical and cortico-cortical layer-specific microcircuits derived from previous invasive anatomical studies (Figure. 3.1): 1) FC between the entire thalamus and cortical layers I and VI must be significantly greater than between the whole thalamus and other layers. This follows from evidence in rat brain tracing studies that show that regions across the cortex receive inputs to layer I from M-type thalamic neurons distributed in most thalamic nuclei [94]–[99]. Pyramidal neurons in layer-VI are known to target all thalamic nuclei. Further, FC between somatosensory thalamus (ventral posterolateral nucleus, VPL) and layer IV, VI of the primary somatosensory cortex (S1), must be stronger than other layers. This follows from the well-known C-type thalamic neurons in VPL that primarily target layer IV in the primary somatosensory cortex, and then corticothalamic pyramidal neurons in layer VI project back to C-type thalamic neurons in VPL [100], [101]; 2) Inter-hemispheric cortico-cortical FC (i.e. between the left and right brain regions of the same area) in superficial layers (layer I-III) must be higher compared to deep layers (layer V-VI). This follows from evidence in rodents that 80% of the cell bodies of those callosal projecting neurons are distributed in layer II and layer III, with only 20% in layers V and VI [102], [103]. Other studies have claimed that layers

I through III are the main target of interhemispheric cortico-cortical afferents, while some suggest that layer III is the main source of cortico-cortical efferents [104]–[106]. Taken together, it makes sense to hypothesize higher cortico-cortical FC in superficial layers compared to deeper layers.

We found that resting state functional connectivity at the laminar level, to a great extent, were in sync with the hypotheses stated above. To the best of our knowledge, we are the first to show that fine-grained layer-specific thalamocortical and corticocortical anatomical connections between cortical layers are reflected by stronger resting state functional connectivity in these pathways.

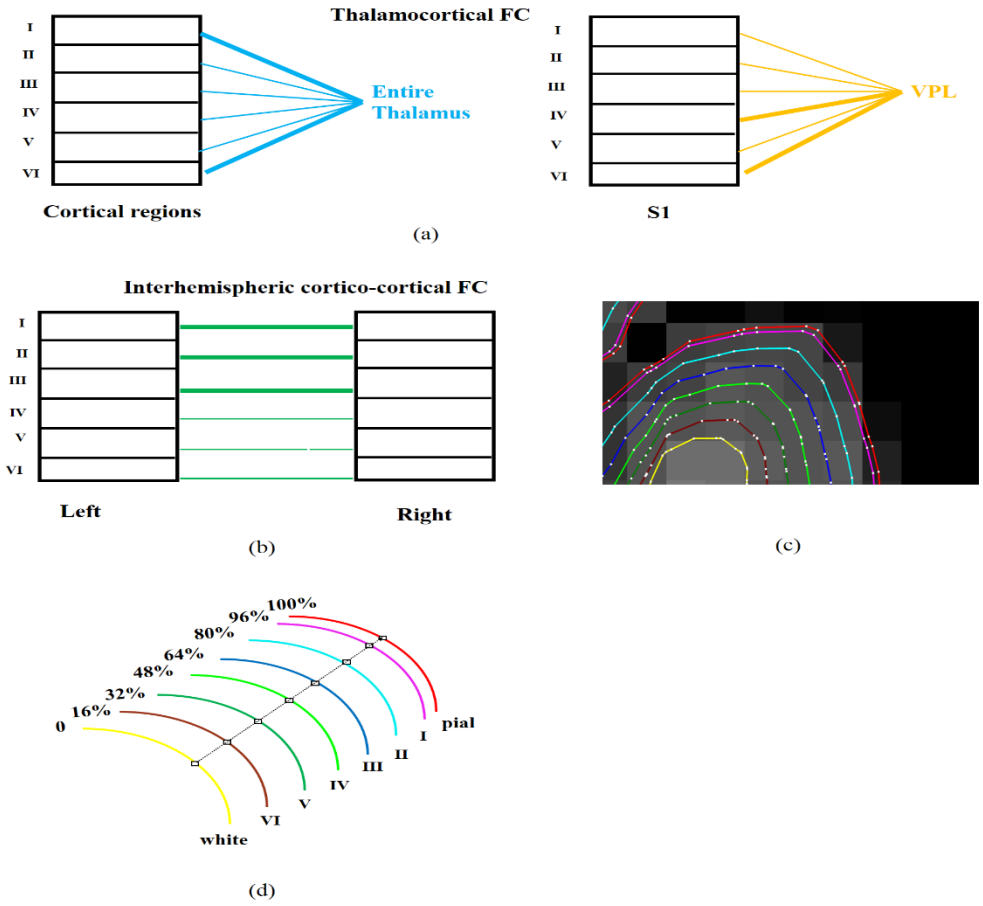

Figure 3.1 *An illustration of our functional hypotheses that were motivated by previous invasive anatomical tract tracing studies. The width of the lines represent the strength of the connections. (a)Thalamocortical hypotheses: We hypothesized that FC between the entire thalamus and cortical layers I and VI will be significantly stronger than between the thalamus and other layers (blue, left panel). Further, FC between somatosensory thalamus (ventral posterolateral nucleus, VPL) and layers IV, VI of the primary somatosensory cortex (S1) will be stronger than with other layers (yellow, right panel). (b) Cortico-cortical hypothesis: Inter-hemispheric cortico-cortical FC between homologous regions in superficial layers (layer I-III) will be stronger compared to that in deeper layers (layer V-VI). (c) 6 surfaces plus white matter and pial surface overlayed on anatomical MRI (white matter surface: yellow, layer VI surface: brown, layer V: green, layer IV: lime, layer III: blue, layer II:, cyan, layer I: purple, and pial surface: red ; the white dots are the vertices on these surfaces). (d) An illustration of the relative distance of 6 intermediate surfaces to white matter surface.*

3.2 Methods

3.2.1 Data Acquisition

All subjects were provided informed consent, and the experimental protocols were approved by the Auburn University Institutional Review Board. High resolution resting state fMRI data was obtained from twenty healthy individuals using an EPI sequence with the following parameters: 37 slices acquired parallel to the AC-PC line, 0.85 mm× 0.85 mm× 1.5 mm voxels, TR/TE: 3,000/28ms, 70º flip angle, base/phase resolution 234/100, A→P phase encode direction, iPAT GRAPPA acceleration factor=3, interleaved acquisition, 100 time points. Data were acquired on a Siemens 7T MAGNETOM outfitted with a 32-channel head coil by Nova Medical (Wilmington, MA).

A whole-brain high-resolution three-dimensional (3D) MPRAGE sequence (256 slices, 0.6 mm × 0.6 mm × 0.6 mm, TR/TE: 2,200/2.8, 7º flip angle, base/phase resolution 384/100%, collected in an ascending fashion, acquisition time=14:06) was used to acquire anatomical data.

3.2.2 Functional MRI data preprocessing

Slicing time correction was applied, and all functional MRI data were motion corrected using rigid body registration using SPM software (http://www.fil.ion.ucl.ac.uk/spm/). Next, linear trends were removed from each voxel time series. We also removed the nuisance variance in the data, comprised of mean time series from ventricular CSF, white matter, as well as six motion parameters. Importantly, spatial smoothing and spatial normalization were not performed. Spatial

smoothing negates the advantages gained by smaller voxels sizes. Also, spatial smoothing is employed in traditional general linear model based activation analysis in order to satisfy the assumptions of random field theory. We did not perform those kinds of analysis and hence found it unnecessary to spatially smooth the data. Next, the Freesurfer analysis pipeline enables individual-specific cortical parcellation from which we extracted the time series used in the analysis. Therefore, we found that spatially normalizing the data into a common space and incurring the costs of blurring and registration errors associated with such a procedure was unnecessary and may be counter-productive for the small voxel size we had and the type of analysis we planned.

3.2.3 Surface-based MRI analysis

Cortical surface reconstruction of the cerebral cortex from magnetic resonance images is a major step in the quantitative analysis of the human brain structure. Cortical reconstruction approaches with Freesurfer are optimized for standard resolution (~1mm) data. However, in this work, we applied Lüsebrink's method to preprocess high-resolution anatomical MRI data with our original 0.6mm isotropic resolution using FreeSurfer 6 beta version [107]. The white/gray and gray/CSF interfaces, as well as cortical thickness maps were automatically generated with FreeSurfer (Figure 3.1). The surfaces generated by Freesurfer are represented in the form of triangular meshes, and each triangle has three vertices. Also, a set of 3D coordinates of these surfaces gives position of the vertices.

Once we obtained the white matter and pial surfaces, the laminar profiles were delineated within the cortical gray matter. They were constructed at fixed relative distance between the white

matter and pial surfaces, determined from cortical thickness [24]. The position of each vertex on intermediate surfaces depends on the position of the correponding vertex on the white matter surface (Figure 3.1). The first intermediate surface was located at 16% of cortical thickness away from the white matter surface, then at 32%,48%, 64%, 80%, and 96% depths, giving us a total of 6 layers (Figure 3.1). Additionally, cortical regions defined on the inflated surface were automatically obtained from the Desikan-Killiany (DK) Atlas [29]. The thalamus was identified in MRI volume data using automatic subcortical segmentation proposed by Fischl et al [46].

3.2.4 Registration of functional MRI to anatomical MRI

To enable the analysis of laminar fMRI, we need to align the fMRI volumes to those intermediate laminar surfaces. Apparently, Gray/white matter boundary in the EPI volume is easily identified automatically. We employed a method called boundary-based registration (BBR) [50]. It identified the interface between gray matter and white matter in the EPI data and then calculated a 12 degrees of freedom affine transformation, which registers the interface in EPI data to the corresponding surface reconstruction from the anatomical data (Figure 3.2). After the registration, the results were visually inspected for each subject and manually edited, if needed [50].

3.2.5 Extraction of functional MRI data from different layers

The preprocessed fMRI volume data were then transformed onto the six laminar surface reconstructions using the transformation matrix obtained in the previous step above. An average time series was extracted from the whole thalamus. This was done because our first hypothesis involved the M-type thalamus cells distributed in each nucleus of thalamus [94]–[99]. Next, time

series from each vertex in 34 lateral cortical ROIs in the DK atlas [29] were extracted, separately for left and right hemispheres in each subject. The 68 ROIs' whole time series corresponding to the cortical ROIs were extracted for each of the 6 layers (Figure 3.2).

3.2.6 Blind Deconvolution

After the time series in the preprocessed functional data were transformed onto the six laminar surface reconstructions, we performed vertex by vertex (a vertex is a point on a triangle surface as explained before, see Figure 3.1 (b) blind deconvolution [93] to get each vertex's latent neural response and HRF.

Hemodynamic deconvolution of the BOLD signal is under the assumption that the relationship between a latent neural signal and the BOLD response can be modeled as a linear and time invariant system, which can be described as follows:

$$y(t) = x(t) \otimes h(t) + e(t) \qquad (1)$$

Where $y(t)$ denotes the observed BOLD signal, $x(t)$ donates the underlying latent neural signal and $h(t)$ and $e(t)$ represent the HRF and the noise term in the measurement, respectively. Since the three terms in right side are unobservable quantities, we consider the neuron activity term $x(t)$ as a simple on-off model with series of delta functions $\hat{x}(t)$ as:

$$\hat{x}(t) = \sum_{\tau=0}^{\infty} \delta(t - \tau) \qquad (2)$$

Note that the delta functions modeling the events exist at random times, which essentially amounts to modeling the resting state data as an event-related paradigm with randomly occurring events. Then the HRF $h(t)$ is fitted by using a canonical HRF (two gamma functions) and two

derivatives (temporal derivative and dispersion derivative). The parameters of $h(t)$ are allowed to vary to for each time series. The approximation $\check{x}(t)$of the latent neural signal can be obtained from the observed data using a Wiener filter as described below:

$$\check{x}(t) = d(t) \otimes y(t) \qquad (3)$$

Where $\otimes$ denotes convolution. Applying Fourier transforms to $h(t)$, $y(t)$, $e(t)$, and $d(t)$, respectively, we get $H(\omega)$, $Y(\omega)$, $E(\omega)$, and $D(\omega)$. $D(\omega)$ can be expressed as follows

$$D(\omega) = \frac{H^*(\omega)}{|H(\omega)|^2 + |E(\omega)|^2} \qquad (4)$$

Where $*$ denotes complex conjugate. The estimate $\check{x}(t)$ of the latent neural signals $x(t)$ is then given by

$$\check{x}(t) = \mathcal{F}^{-1}\{D(\omega)Y(\omega)\} = \mathcal{F}^{-1}\left\{\frac{H^*(\omega)Y(\omega)}{|H(\omega)|^2 + |E(\omega)|^2}\right\} \quad (5)$$

In Equation 5, $\mathcal{F}^{-1}$ is the inverse Fourier transform operator. Since the measurement noise $e(t)$ is assumed to be white, the covariance of the noise term must be 0. For task-related fMRI, the stimulus function provides the prior information about neural activity and a generative model whose inversion corresponds to deconvolution. Here, resting state fMRI is considered as a spontaneous event-related signal, and these events can be reflected by relatively large amplitude BOLD signal peaks [93], [108]. Therefore, the time series from each vertex was evaluated against a given amplitude threshold around the local maximum (threshold was set to 1 since the input time

series were normalized) to obtain a set of estimated onsets (the timing of delta functions) for these pseudo-events. In order to get the delay τ (the delay between the peak of fMRI and the peak of neural signal), we searched all integers between [0 8] based on a previous study that reported 4-8 second latencies in the gray matter [109]. Then the optimal integer was chosen as τ for which the covariance of noise $cov(y(t) - \hat{x}(t) \otimes h(t))$ was smallest, to obtain the set of onsets. Subsequently, the vertex-by-vertex HRF was fitted and extracted with these pseudo-events. The readers are referred to Tagliazucchi et al., 2012 and Wu et al., 2013 for further details on the deconvolution method.

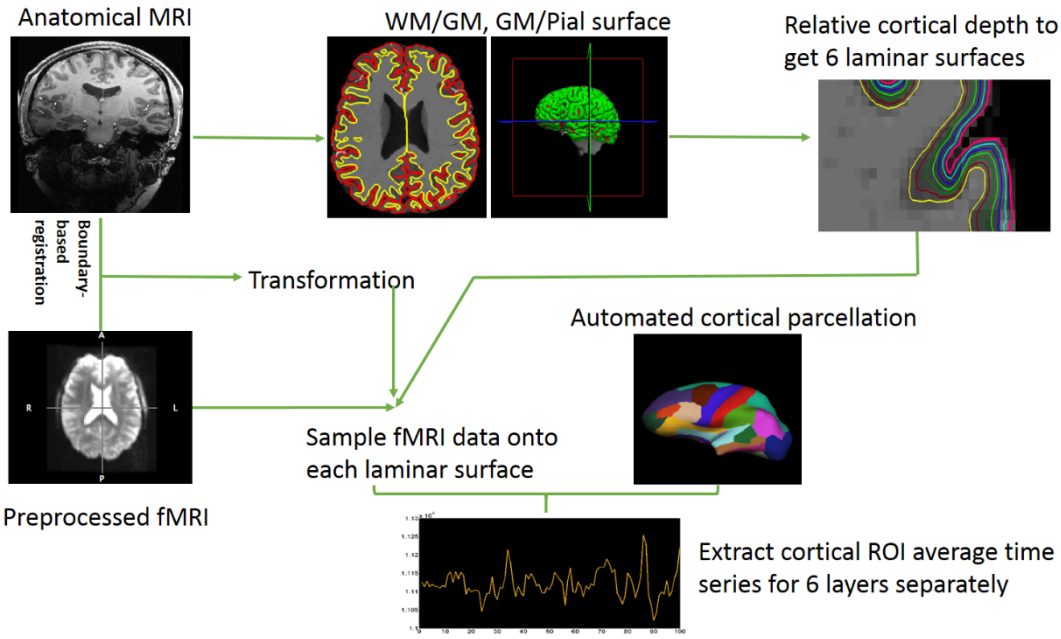

Figure 3.2 *A schematic illustrating the laminar analysis pipeline for extracting mean time series from the six cortical layers for all 68 brain regions in the Desikan-Killiany atlas* [29].

3.3 Results

3.3.1 Functional connectivity across cortical regions between layers

The mean correlation between deconvolved time series in a given layer with those in all layers (for every pair of regions) did not show any significant difference between layers (Figure 3.3). This demonstrates that global connectivity differences between layers were absent.

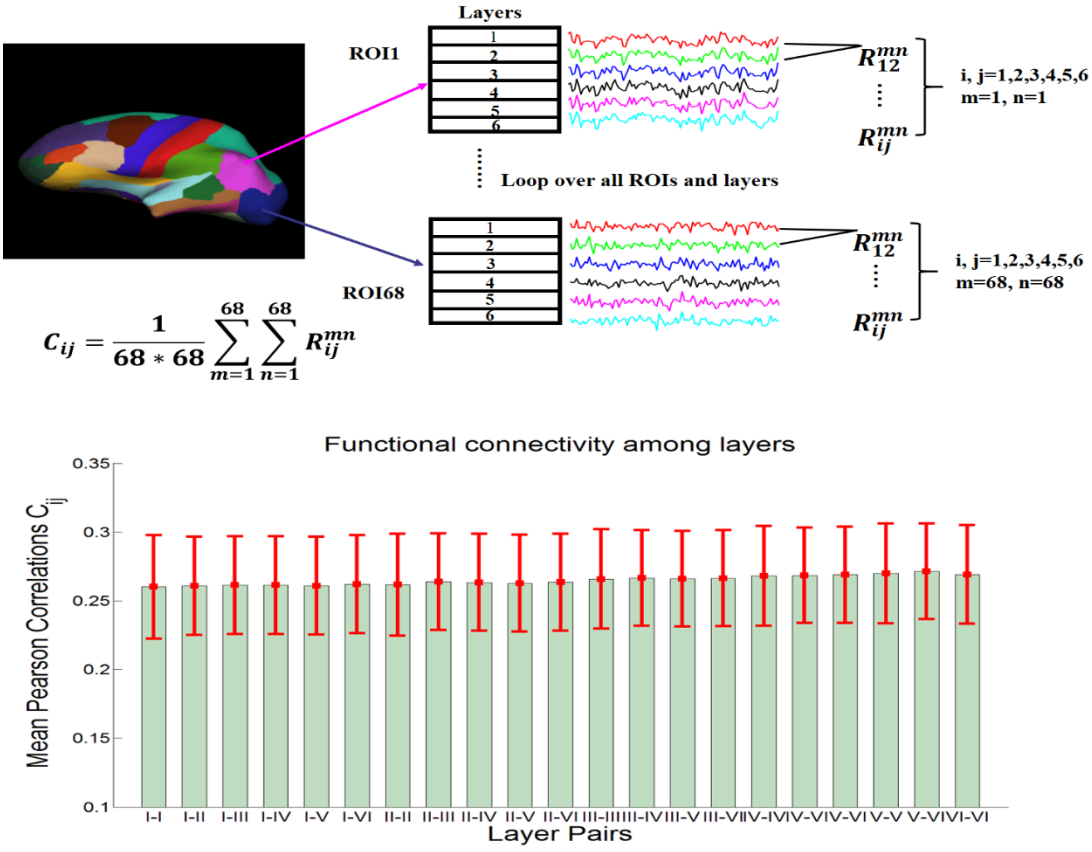

Figure 3.3 *Top: An illustration of the method for calculating FC between all layers across all cortical regions in order to investigate global trends (i, j represents layer number; m, n represents regions, and C_{ij} represents the mean Pearson's correlation between two given layers calculated across all cortical regions). Bottom: The mean Pearson correlation values between a given layer and all layers across all cortical regions in the Desikan-Killiany* [29] *atlas. No significant differences were found. 21 pairs are included. The error bar indicates the calculated standard error.*

3.3.2 Hypotheses testing before deconvolution

In order to test the thalamocotical hypothesis, we computed the Pearson's correlation between the mean time series extracted from 68 ROIs in each layer with the mean time series extracted from the entire thalamus. For testing the specific VPL↔S1 connectivity hypothesis, the Pearson's correlation between the mean time series from primary somatosensory cortex (S1) and the VPL. For testing the cortico-cortical hypothesis, we estimated the mean interhemispheric correlations only between homologous regions in each layer. The functional connectivity pattern for thalamocortical connections showed that the mean Pearson's correlation between layer I and the entire thalamus was strongest across the cortex (Figure 3.4(a)), and was significantly (FDR corrected $p<0.05$) greater than the correlation between the thalamus and layers II-VI. Although layer IV showed a trend to be more strongly connected to the thalamus, it did not reach significance. In contrast, VPL↔S1 connectivity was significantly stronger in layer IV than in layers I, V, and VI (Figure 3.4(b)). Then we examined the interhemispheric corticocortical connections for all 68 cortical regions for each layer (i.e. between the left and right brain regions of the same area). We found that the interhemispheric corticocortical mean correlation for layer III was significantly greater than layer VI ((Figure 3.4 (c)).

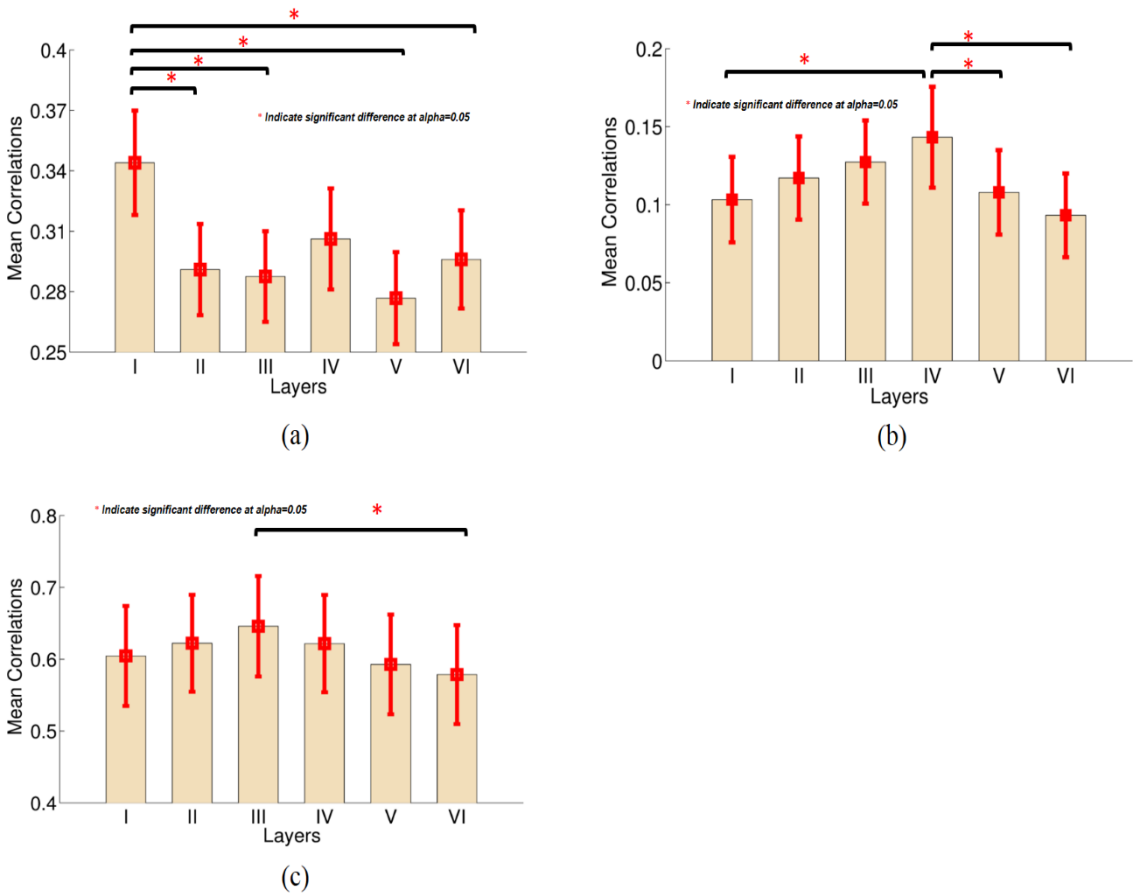

Figure 3.4 *(a) Mean thalamocortical FC values between the entire thalamus and all cortical layers estimated before blind deconvolution; (b) The mean FC between the somatosensory thalamus (VPL) and six different layers of primary somatosensory cortex before blind deconvolution; (c) The mean interhemispheric cortico-cortical laminar FC values estimated before blind deconvolution. The * indicates significant difference with p (corrected) <0.05, the error bar indicates the estimated standard deviation.*

3.3.3 Laminar HRF differences

The hemodynamic response could be different between regions across subjects and it has been previously shown that this might impact the estimates of connectivity obtained between such regions [51], [91]. To assess the laminar variability of HRF and recover the neural response, we performed blind deconvolution before functional connectivity analysis. To assess the effect of deconvolution, we compared the shape of region-specific HRFs across six layers (Figure 3.5). Three parameters of region-specific HRFs we examined were response height, time-to-peak, and full-width at half-max (FWHM). The means and standard deviations of the three parameters were calculated separately for each layer across all subjects. As an illustration, we show the region-specific HRF results for left orbitofrontal cortex (Figure 3.5 (a)-(d)) and primary somatosensory cortex (Figure 3.5 (e)-(h)), which are two of the 68 parcellation regions.

After one-way analysis of variance (ANOVA) for response height ($p=0.0469$), time-to-peak ($p=0.0026$), and FWHM ($p=0.0268$) of region-specific HRF separately, we found response height as well as time to peak and FWHM were significantly different across the layers ($p<0.05$ FDR corrected) for left orbitofrontal cortex. In addition, the three parameters were distinct across layers for left primary somatosensory cortex as well ($p=0.0035$ for response height, $p=0.0014$ for time-to-peak, and $p=0.0312$ for FWHM). Furthermore, multiple comparison of means in one-way ANOVA was employed for each parameter. Here, for the left orbitofrontal cortex, we found that the response height and FWHM of layer I was significantly ($p<0.05$ corrected) larger than for layer VI, and time to peak of layers I, II, and III was significantly ($p<0.05$ corrected) larger than layer VI. For primary somatosensory cortex, we found that the response height and time to peak of layer I were significantly ($p<0.05$ corrected) larger than for layer III-VI, and at the same time, the

response height and time to peak of layer VI were significantly smaller ($p<0.05$ corrected) than layer II. Moreover, FWHM of layer I was significantly ($p<0.05$ corrected) wider than layer VI.

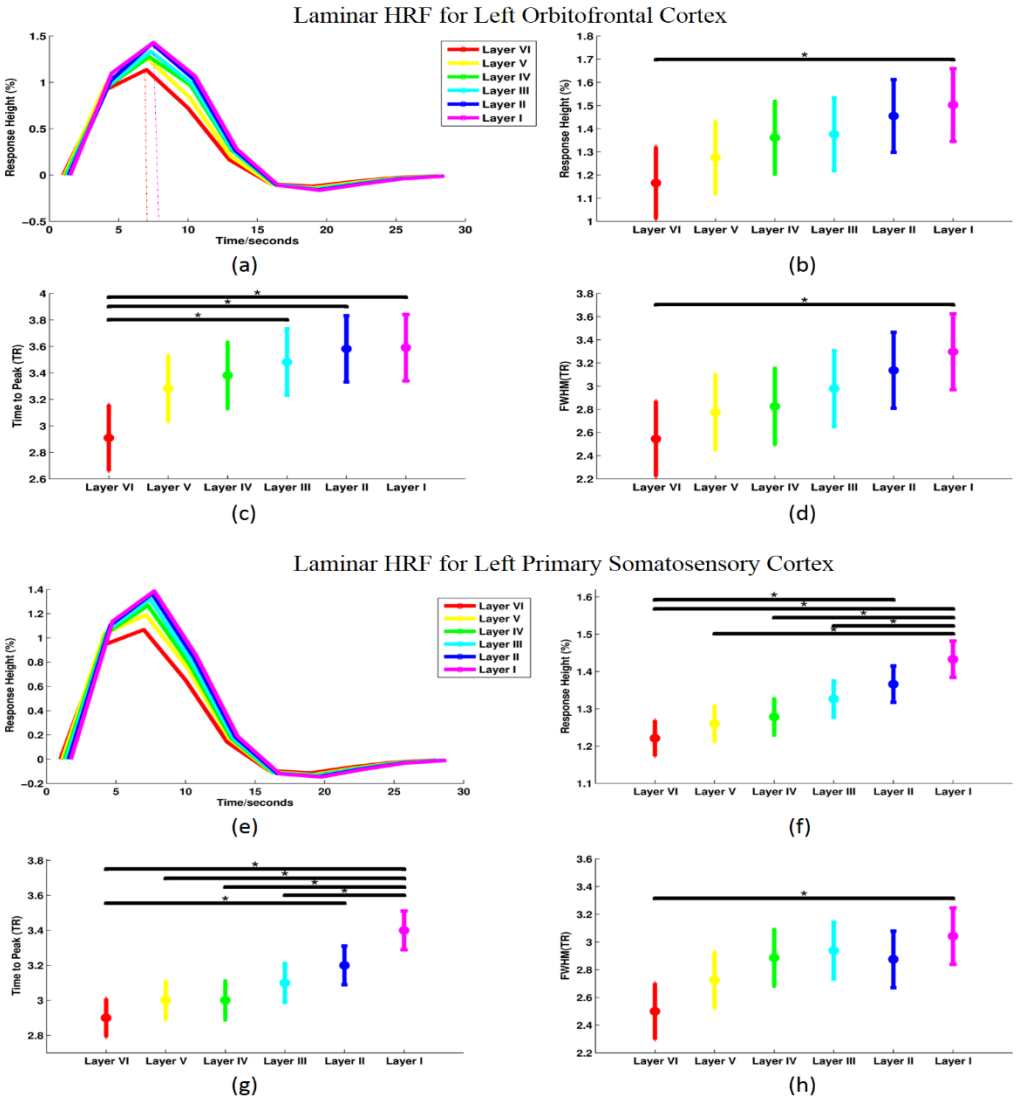

Figure 3.5 *Region-specific HRF plot and multiple comparisons across the layers for left orbitofrontal cortex (OFC) (panel (a)-(d)) and left primary somatosensory cortex (S1) (panel (e)-(f)). The mean left OFC (a) and left S1 (e) HRF plot for six layers separately. Layer VI (red), layer V (yellow), layer IV (green), layer III (cyan), layer II (blue), and layer I (purple); multiple comparisons across the layers of left OFC (b) and left S1(f) for response height; time to peak multiple comparisons across layers of left OFC (c) and left S1 (g); FWHM multiple comparisons across the layers of left OFC (d) and left S1 (h). The * indicates significant difference with p (corrected) <0.05. The error bar indicates the calculated standard deviation.*

To investigate whether this is a general fact for all region-specific laminar HRFs, we performed similar analyses for all other 66 regions and summarized the results in Figure 3.6. 66 out of 68 regions had significant difference ($p<0.05$ corrected) across the layers for the response height, 62 out of 68 regions for time to peak, and 36 regions for FWHM. In summary, the HRF varies across cortical layers in many brain regions and it is necessary to recover the latent neural signal at each layer before performing connectivity analysis.

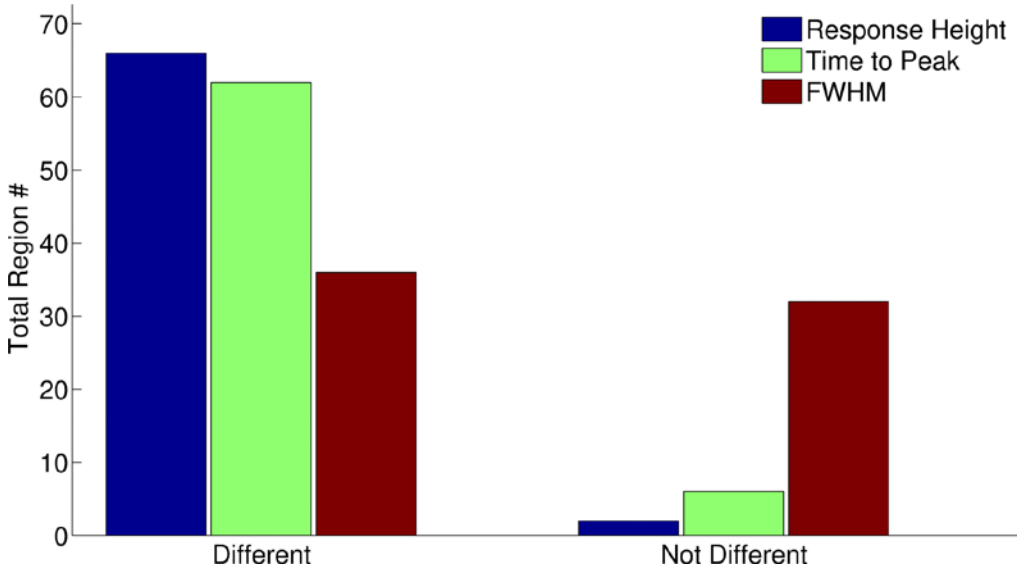

Figure 3.6 *Summary of one-way ANOVA analysis performed on HRF parameters (response height, time to peak, and FWHM) for 68 regions. 66 out of 68 region had significant difference across the layers for the response height, 62 out of 68 regions for time to peak, and 36 regions for FWHM at $p<0.05$.*

3.3.4 Individual-level FC difference before and after deconvolution

We estimated individual-level mean connectivity values of all possible connectivity paths between the 68 ROIs and the results for all 20 subjects, obtained with both deconvolved and non-deconvolved data, are shown in Figure 3.7. The differences in connectivity due to deconvolution are plotted at the bottom part of Figure 3.7, showing the magnitude of change caused by HRF variability in each subject. The group average non-deconvolved FC value was 0.033 higher than deconvolved FC value. A paired t-test between non-deconvolved FC and deconvolved FC returned a high statistical significance for all paths (p=0.0012).

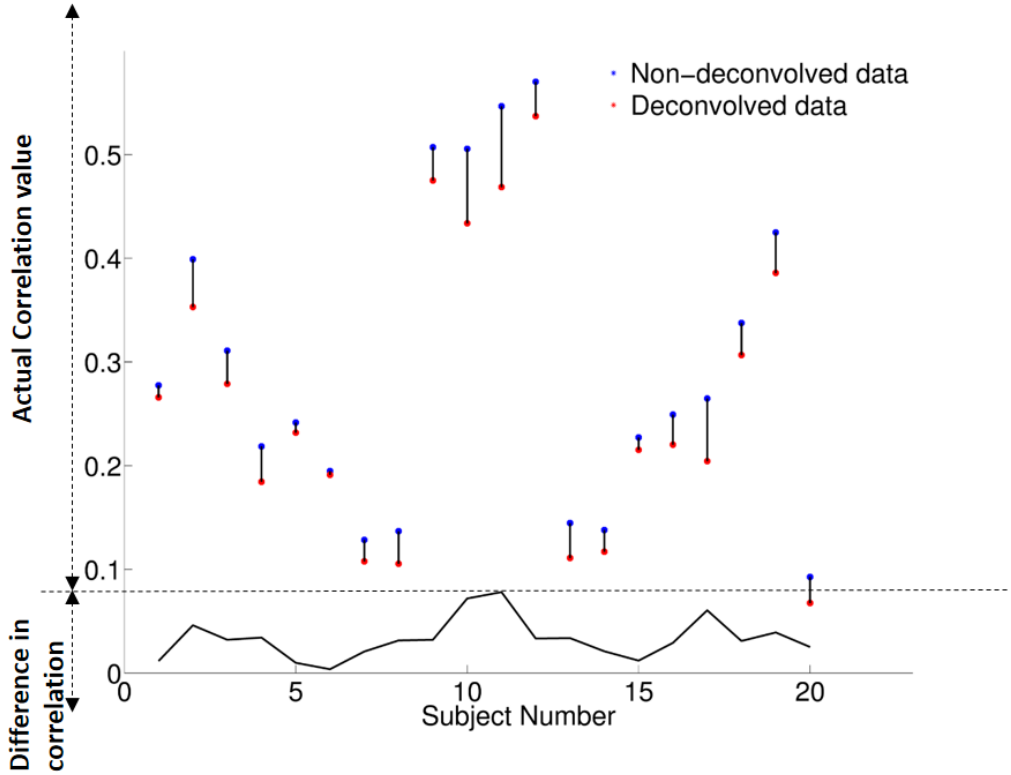

Figure 3.7 *The comparison of the individual-level average FC values before and after deconvolution for all paths. Blue represents FC values with non-deconvolved data, and red for FC values after deconvolution.*

3.3.5 Hypotheses testing after deconvolution

Results obtained after deconvolution, i.e. those estimated from latent neural signals, were more in sync with our hypotheses. As we can see from Figure 3.8 (a), FC between the entire thalamus and Layer I across the cortex was significantly greater than the FC between the entire thalamus and layers II-VI (FDR corrected $p<0.05$). Also, FC between the entire thalamus and Layer VI was significantly higher than FC between the entire thalamus and layers II, III, and V. In contrast, the FC between sensory core thalamus (VPL) and layers IV, VI of S1 was significantly stronger than between VPL and layers I, II, III, and V (Figure 3.8 (b)).

Finally, we examined the interhemispheric corticocortical FCs for each layer (i.e. between the left and right brain regions of the same area) and compared the FC results before deconvolution (Figure 3.4 (c)) with FC results after deconvolution (Figure 3.8 (c)). Before deconvolution, only the interhemispheric corticocortical FCs for layer III were significantly greater than layer VI (Figure 3.4 (c)). But after deconvolution, FCs between homologous regions in layers I-III were significantly greater than in layers IV-VI (Figure 3.8 (c)). Generally speaking, the inter-hemispheric mean correlations in superficial layers were higher compared to those deeper layers [106].

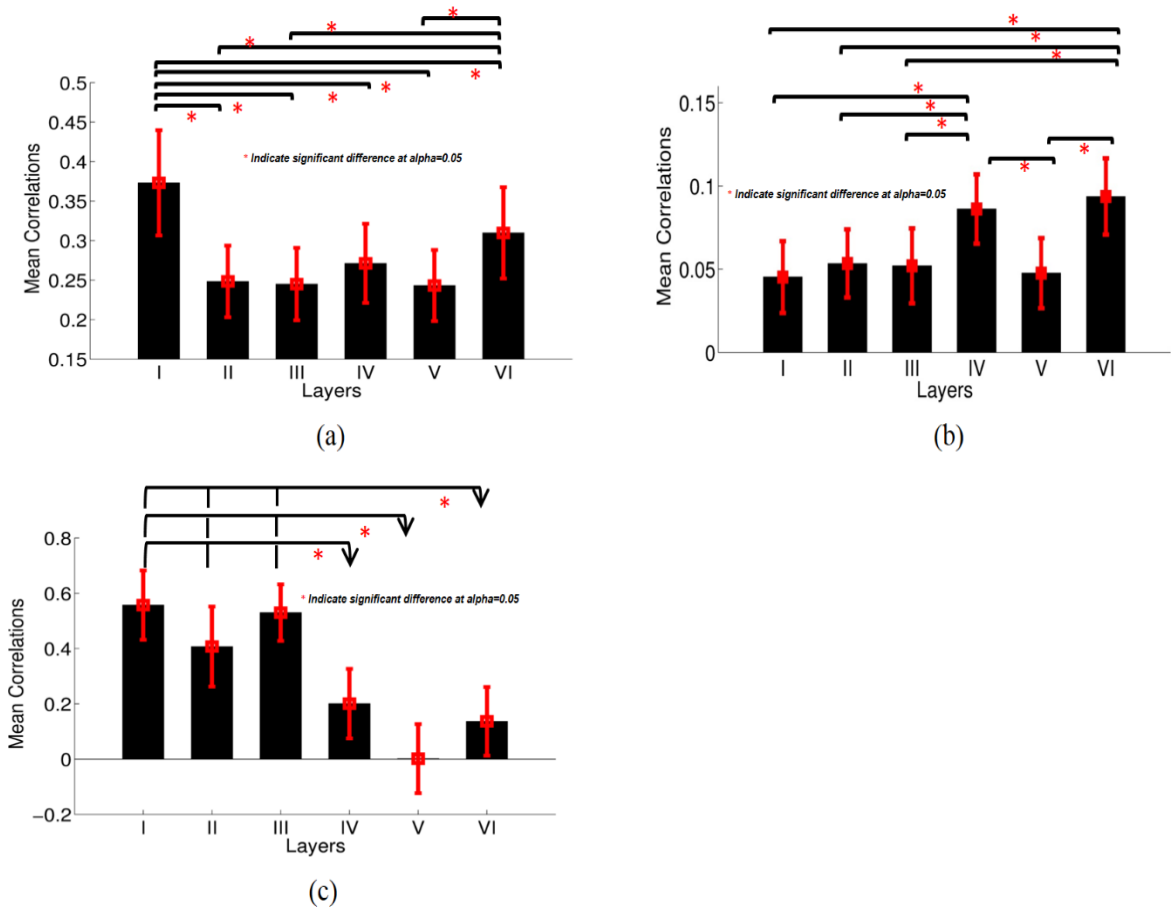

Figure 3.8 *(a) The mean thalamocortical FC values between the entire thalamus and cortical layers after blind deconvolution; (b) The mean FC between sensory core thalamus (VPL) and six different layers of primary somatosensory cortex after blind deconvolution; (c) The mean interhemispheric cortico-cortical laminar FC values after blind deconvolution. The * indicates significant difference with p (corrected)<0.05. The error bar indicates the calculated standard deviation.*

3.4 Discussion

In this study, we tested hypotheses involving thalamocortical and cortio-cortical layers specific circuits derived from previous invasive anatomical studies. The thalamocortical hypothesis is that FC between the entire thalamus and cortical layers I and VI must be significantly greater than that between the thalamus and other layers based on the fact that the regions across the cortex receive inputs to layer I from M-type thalamic neurons distributed in most nuclei of thalamus and receive corti-thalamic radiations from layer VI of the cortex [94]–[99]. Accordingly, we found that FC (estimated from latent neural variables) between the entire thalamus and layer I was indeed significantly greater than between the thalamus and layer II-VI, and FC between thalamus and layer VI was higher than between the thalamus and layers II, III, and V. Also, we found the FC between sensory core thalamus (i.e. VPL) and layer IV, VI of the primary somatosensory cortex, were higher than other layers. This follows from the fact that C-type thalamic neurons in VPL primarily target layer IV in the primary somatosensory cortex, and then corticothalamic pyramidal neurons in layer VI project back to C-type thalamic neurons in VPL [100], [101]. To a large extent, the results confirmed our hypotheses. The cortico-cortical hypothesis is that inter-hemispheric cortico-cortical FC in superficial layers (layer I-III) must be higher compared to deep layers (layer V-VI) following evidence in rodents that 80% of the cell bodies of those callosal projecting neurons are distributed in layer II and layer III, with only 20% in layers V and VI [102], [103]; [104]–[106]. Our results suggested that the interhemispheric FC was significantly higher in superficial layers than deeper layers. To our knowledge, this is the very first study to investigate the sensitivity of resting state fMRI connectivity at submillimeter spatial scale to the connectional architecture at the laminar level.

One common concern in laminar fMRI studies is the large signal amplitude on the pial surface, which could be potentially affected and contaminated by large veins on the cortical surface, or partial volume effects from large voxel sizes. Different methods have been employed to resolve the large vein problem. Simply avoiding the first layer compartment is the easiest way [24]. Indeed, if we did consider parts of our hypothesis by excluding the first layer, they would be confirmed by our results. Another alternative approach is restricting the laminar analysis to strongly activated clusters in each subject [25]. A novel pial vein pattern analysis by optical imaging was suggested by Chen et al to remove voxels associated with large veins, and the vein-free fMRI exhibited clear laminar specificity [36]. However, around 40% of activated voxels in the primary visual cortex was excluded for this study. Also, optical imaging technique used by Chen et al was invasive, and hence is not suitable for human studies. In this study, we approached this issue in terms of HRF differences across layers. We reasoned that any differences between BOLD signals across layers that have a vascular origin, must be reduced or eliminated if voxel (or vertex-specific) HRF was deconvolved from the BOLD data and connectivity estimation was performed in the latent neural space.

To investigate the variability of HRF across layers, we employed a simple but powerful blind deconvolution technique to recover the latent neural signal at each vertex. Our results showed that all three parameters of region-specific laminar HRF (response height, time-to-peak, and FWHM) varied in reference to cortical depths, and were significantly greater in superficial layers than deeper layers. This finding matches findings from previous HRF studies on animals. Tian et al found both the onset of BOLD response and the initial dip rely on cortical depth, and the fastest response was in deep layer within the rat primary somatosensory cortex [86]. Also, Yu et al showed the onsets at different layers coincided with the neural inputs with line-scanning fMRI

both in rat somatosensory cortex and motor cortex [84]. But importantly, we demonstrated that this is a general fact for almost all cortical regions. The comparison of functional connectivity before and after deconvolution showed the importance and necessity of recovering latent neural signals before any resting-state functional connectivity analysis is performed at the laminar level. The functional connectivity post-deconvolution in the latent neural space aligned more closely with the underlying anatomical connections compared to FC obtained on BOLD data.

Limitations and Future Work. There are a few limitations of present study, which need to be addressed in future layer-specific fMRI connectivity related research. First, different methods exist for identifying different cortical lamina from MRI data. The method we employed was to construct laminar profiles, which keeps a relatively fixed distance to the cortical boundaries (Figure 3. 1), the so-called equidistant laminae [25], [48], [49]. An alternate approach is the equipotentials method, wherein the equipotentials are computed between the inner white matter surface and pial surface with the Laplace equation, and then the cortical profiles can be constructed along the gradients [110]. However, the drawback with this approach is that the Laplacian equation may not match the anatomical layers observed from high-resolution MRI [111]. Recently a new model called equal-volume model for identifying cortical laminae was proposed by Waehnert and colleagues [111], and they claimed that it provides a better fit to observed cortical layering. In future, studies must compare the three different models for how well functional connectivity derived from layers constructed by them match the underlying anatomical predictions.

Second, the spatial laminar point spread function (SL-PSF) of the BOLD response presents a fundamental stumbling block for gaining laminar specificity in fMRI data. Lower layers always contribute signal to the upper layers, because the intracortical veins (ICV) are perpendicular to the surface, and the drain blood flows along the ICV into pial veins on the pial surface [89]. The

interpolation-averaging method, wherein the fMRI volume is interpolated at certain cortical depth and the surface profiles are averaged, has been proposed for addressing this issue [24], [25], [33], but a more precise method to extract laminar signal is needed. As we briefly mentioned in the introduction, this is especially true for gradient echo EPI based fMRI, which has a flatter PSF compared to spin-echo based EPI. Therefore, future studies may investigate whether spin echo EPI may be better for FC studies at the laminar level, even with the loss of sensitivity in spin echo compared to gradient echo. Recently, an extension of the Friston-Buxton hemodynamic model, which accounts for blood draining effects by coupling local hemodynamics across layers in dynamic causal models of fMRI during visual activation, was reported [59]. But, priors about two parameters controlling blood draining effects (the delay τ_d between the lower and upper layers, and λ_d that represents the strength of the blood draining effect from the lower to the upper layers) need further experimental validation in human resting state studies. Investigations into the laminar specificity of BOLD have invariably used task-based paradigms and cannot be readily generally to resting state given that neurovascular coupling likely operates under a different regime in resting state (see extension of Buxton's balloon model to resting state conditions in [90]. Therefore, further modeling and experimental work is needed in this area, which could potentially lead us to a reliable and accurate laminar time series that will allow a more fine-grained investigation of resting state FC at the laminar level.

Third, the hypotheses we chose to test provide only an initial demonstration of the sensitivity of resting state fMRI functional connectivity to layer-specific functional microcircuits in the human brain. However, further fine-grained investigations are possible. This could involve specific thalamocortical pathways from other thalamic nuclei, specifically in systems that are unique in humans and for which we do not have reliable homologues in animals, and hence are

not amenable to invasive investigations. For example, two parallel layer-specific pathways connect language-related thalamic nuclei to layer I and middle layers of Broca's area. The cortico-thalamic radiations from Broca's area in turn originate from cortical layers V and VI. Dysfunction in these pathways are important in aphasic patients with damage to the thalamic nuclei [112]. Our study opens the possibility of characterizing such layer-specific microcircuits, both in healthy and clinical populations, using ultra high field fMRI in the future.

Fourth, it is well recognized that functional connectivity cannot decipher the direction of information flow between regions where as many anatomical projections that we have based our hypothesis on, are in fact directional in nature. Therefore, the next logical steps would be to test whether directional connectivity models of fMRI such as dynamic causal modeling (DCM) [113] and Granger causality (GC) [114]–[117] are sensitive to directional-specific anatomical projections at the layer-level.

Finally, we employed a gradient echo EPI sequence optimized for SNR and spatial resolution. The sequence used for data acquisition for testing FC-related hypotheses at the laminar level could well be optimized in other ways. This includes using a spin echo sequence and trading sensitivity for a narrow SL-PSF, as well as using a multiband EPI sequence to obtain a shorter TR, possibly at the cost of SNR (but not spatial resolution). One way of increasing the spatial resolution further would be to restrict coverage to regions specifically relevant to the hypothesis being tested, but this would require a custom processing pipeline (other than the one in FreeSurfer) that does not require whole brain coverage. In summary, our seminal study offers a lot of possibilities for investigating the brain's functional connectome at a more fine-grained laminar spatial scale.

3.5 Supplementary Materials

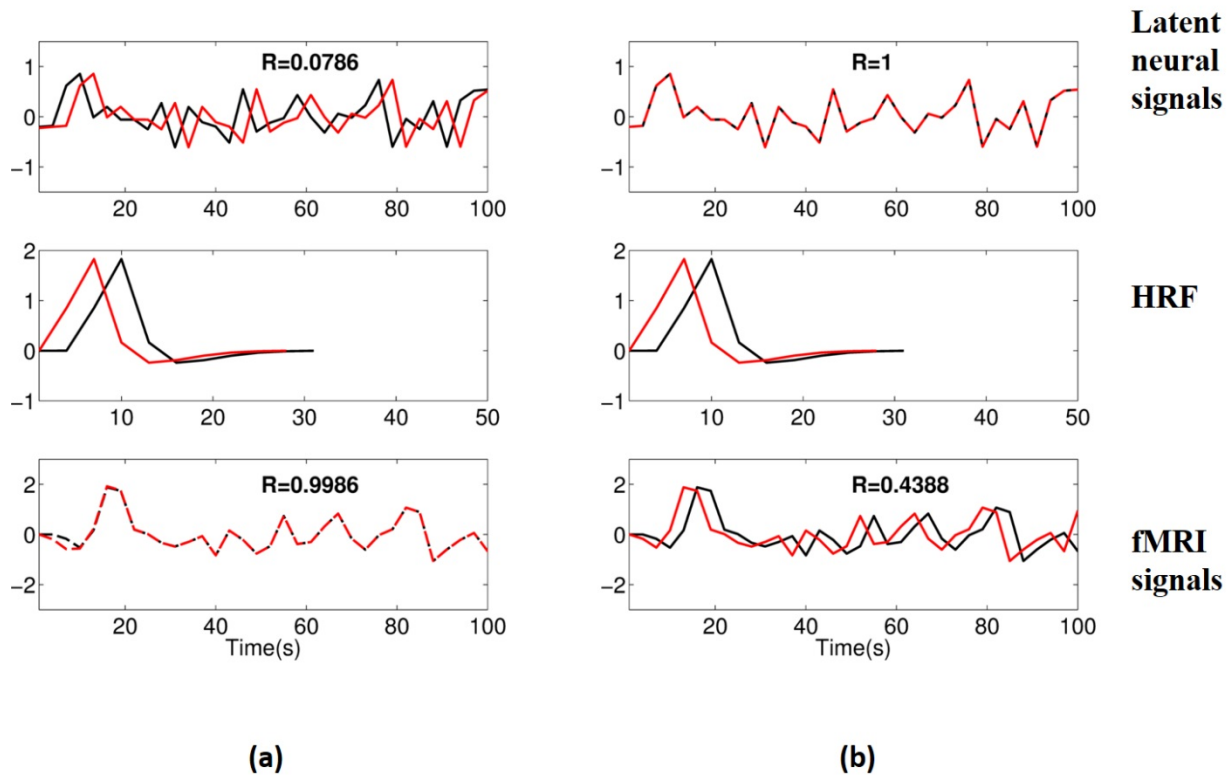

Figure S1 *The importance of performing hemodynamic deconvolution illustrated for two possible scenarios. (a) The fMRI signals are highly correlated (the bottom left panel), whereas the latent neural signals are not (the top left panel); (b) the underlying latent neural signals are highly synchronized (the top right panel), however, the correlation between fMRI signals are low (the bottom right panel). Both scenarios result from the fact that the HRFs corresponding to the two signals are not the same and have a delay between them. Therefore, when convolved with the latent neural signals, they can introduce or nullify the shifts in the resulting BOLD signal. The (a) scenario can cause false positives, and (b) scenario lead to false negatives.*

Chapter 4 A Framework for Investigating the Brain's Connectome at the Laminar Level using 7T fMRI: Illustration using Corticogeniculate Feedback Mechanism in the Human Visual System

4.1 Introduction

The lateral geniculate nucleus (LGN), a small subcortical structure that is part of the thalamus, is a very important relay center in the visual system. There is a dense network of feedforward and feedback projections between the LGN of the thalamus and primary visual cortex. In the feedforward pathway, three distinct classes of neurons in LGN – magnocellular, parvocellular and koniocellular neurons, receive signals from the retina and transmit them (in parallel) to layer IV and layer VI of the primary visual cortex. In the feedback pathway, the corticogeniculate neurons in layer VI of the primary visual cortex exert influence on those three classes of neurons within the LGN in parallel [118]–[124]. These feedforward and feedback parallel processing streams are recognized ubiquitously in the primate visual system, and are most prominent in the LGN, where three types of neurons (magnocellular, parvocellular and koniocellular neurons) are segregated into distinct strata. Previous studies about the physiology of magnocellular and parvocellular LGN have shown they have different spatial, temporal, luminance, and chromatic stimulus preference [125]–[129]. The magnocellular neurons respond well for monochromatic, low spatial frequency, high temporal frequency and high contrast visual stimuli with motion, compared with parvocellular neurons, which have a preference for color, high spatial

frequency, low temporal frequency, and low contrast. Consequently, the magnocellular pathway is useful for the perception of "where" information and is processed in the dorsal visual stream while the parvocellular pathway is useful for the perception of "what" information and is processed in the ventral visual stream (It is to be noted here that the segregation of magnocellular and parvocellular pathways and their preference for processing specific types of visual information is not mutually exclusive and a significant amount of cross-talk exists. See Merigan et al [130] for details. However, we only assume that the magnocellular pathway is recruited more than the parvocellular pathway for monochromatic, low spatial frequency, high temporal frequency and high contrast visual stimuli with motion. We do not intend to imply that the magnocellular pathway does not process other types of visual information). Our focus in this report is on the parts of the magnocellular pathway between LGN and the primary visual cortex.

The corticogeniculate neurons in layer VI of primary visual cortex are sensitive to visual stimulus orientation and direction of motion. Therefore, the dynamic influence of the feedback to the magnocellular neurons in LGN will depend on how the visual input drives the receptive fields of neurons in layer VI of the primary visual cortex [131]. Although magnocellular neurons in LGN are not selective for orientation or direction, they have circular concentric center-surround receptive fields in which responses from the stimulation of the central receptive field are antagonized by simultaneous stimulation of the surround receptive field [132]–[135]. In particular, the feedback from corticogeniculate neurons in layer VI of the primary visual cortex modulates the strength of this center-surround interaction for moving stimuli. Feedback can make this surround antagonism for moving stimuli stronger and reduce the response further [136]. The magnocellular neurons in LGN seem to be inhibited by projections from neurons in the primary

visual cortex via inhibitory neurons in the thalamus, while neurons that project from the LGN to the primary visual cortex are excitatory; in other words, this feedback loop is negative.

To date, most findings about feedforward and feedback pathways come from anaesthetized animals with invasive methods such as single electrodes recordings [119], [120], [137]–[141]. Though these studies have certainly increased our knowledge of corticogeniculate feedback mechanism, it is imperative that they be confirmed in conscious humans. Therefore, we propose an experimental paradigm employing non-invasive imaging methods such as high resolution functional magnetic resonance imaging (fMRI) at ultra-high fields (7T) coupled with an analysis framework which could potentially be generalized to investigate laminar-level circuitry in any part of the human brain. Recent non-invasive studies have successfully employed high-resolution fMRI to investigate the top-down feedback effects on laminar fMRI response in primary visual cortex [26], [34]. However, they infer the effects of feedback and feedforward pathways by clever manipulation of the experimental design by masking some of the effects to indirectly infer these mechanisms. In contrast, we propose a framework where in these effects can be directly tested using standard fMRI paradigms and use of advanced brain connectivity models. To the best of our knowledge, none of previous fMRI studies have directly investigated laminar-level feedback or feedforward pathways in the human brain. Here we pick the example of the magnocellular pathway between LGN and the primary visual cortex (layer IV and layer VI) in the human brain – the feedback from Layer VI to LGN, and the feedforward from LGN to layers VI and IV of the primary visual cortex as well as from layer IV to layer VI within the primary visual cortex – since the visual system in general and the lower level circuit involving the LGN and the primary visual cortex in specific, are largely similar in humans and animals [142]–[144]. This allows us to form hypotheses based on invasive animal literature that can be tested in humans. However, the proposed

framework in itself is generally applicable to any other brain system. This is important given the fact that the similarities between animal and human brains begin to diminish beyond sensory systems and hence, once our method is established in the visual system, it will pave the way for a fine-grained mechanistic understanding of the brain's laminar-level functional connectome in more complex domains such as cognition and language.

Our objective for this study is to investigate the magnocellular pathway between LGN and the primary visual cortex – the feedback path from corticogeniculate neurons in layer VI of primary visual cortex to magnocellular neurons in LGN, and the feedforward paths from LGN to layer VI and layer IV of the primary visual cortex, as well as from layer IV to layer VI within the primary visual cortex. We hypothesize that these functional pathways, known from invasive animal studies, can be inferred by employing the proposed analysis pipeline on data acquired noninvasively using functional magnetic resonance imaging (fMRI) in humans engaging in a visual motion task. In order to test this, we had to overcome three challenges. First, it is difficult to localize human magnocellular neurons of LGN (magnocellular LGN) because of the small size and deep location within the brain. In order to address this, we designed specific visual stimuli to evoke magnocellular LGN maximally. We used the typical building block of the visual stimulus in the field of visual neuroscience – Gabor Patch, which can efficiently activate and match the shape of receptive fields in the visual cortex, and therefore help detect the center-surround inhibition effects [145]–[149]. The choice of the Gabor patch sizes for center-surround inhibition effects is in reference to Murphy's work [133]. The Gabor patch in this study was specifically designed with characteristics, e.g., monochrome, high contrast, low spatial frequency, and high temporal frequency, in order to maximally activate magnocellular neurons within LGN and the corresponding corticogeniculate neurons in layer VI within the primary visual cortex [120], [150]–

[157]. We then performed the functional mapping of magnocellular LGN sub-region in the human brain using high resolution anatomical and functional MRI data acquired ultra-high field (7T). Second, we needed high-resolution imaging and advanced imaging processing techniques to resolve cortical layers. Recent advances in high-field functional MRI make it feasible to measure the blood oxygen level dependent (BOLD) signals with sub-millimeter resolution [25], [33], [158], [159]. Also, several models to construct laminar profiles have been proposed, including equidistant laminae model [24], equipotential method with Laplacian equation [110], and equal-volume model [111]. In this study, we adopted the equidistant laminae model, which keeps a relatively fixed distance to the cortical boundaries, because equidistant stratification contains a broad isocontour that follows the stria of Gennari everywhere in the cortex [24]. The drawback of equipotential model is that the Laplacian equation does not match the anatomical layers observed from high-resolution MRI. As regards the equal-volume model, it does not provide improvement over the equidistant model because of its weak estimation of curvature [111]. Third, we had to use a dynamic effective connectivity model to unveil the directional influences between layers in primary visual cortex and LGN. We used a state-of-the-art dynamic Granger causality [55], [114], [160]–[162] method to quantify dynamic feedforward and feedback pathways between magnocellular LGN and primary visual cortex.

Our results demonstrated that: (1) functional localization of magnocellular cells in LGN with high-resolution MRI is a feasible method; (2) the “enhanced center surround inhibition” effect on magnocellular cells within human LGN is salient and detectable using non-invasive high resolution functional MRI at 7T; (3) the feedforward and corticogeniculate feedback functional pathways can be inferred using dynamic directional connectivity models of fMRI and could potentially explain the mechanism underlying center-surround inhibition in the human visual

system; (4) our framework is domain-neutral and could potentially be employed to investigate the human brain's connectome at the laminar level in other systems related to cognition, memory and language.

4.2 Materials and Methods

4.2.1 Subjects

20 adult subjects (10 males, 10 females; 24.5±3.3 years of age) participated in this study. All subjects had normal eyesight or corrected-to-normal visual goggles. All subjects were provided informed consent, and the experimental protocols were approved by the Auburn University Institutional Review Board. All subjects were scanned in multiple sessions on a 7 Tesla Siemens MAGNETOM MRI scanner.

4.2.2 Visual Stimuli and Task

In this study, we designed specific visual stimuli—six different sizes of rightward moving sine wave gratings (Gabor patches), which can maximally elicit the BOLD response of magnocellular LGN and corticogeniculate neurons in layer VI of the primary visual cortex. Gabor patches can efficiently match the shape of receptive fields in the visual cortex and optimally show the enhanced center-surround inhibition effects on magnocellular LGN. The choice of the Gabor patch sizes for center-surround inhibition effects is in reference to the work by Murphy and colleagues[133].

The stimuli were generated on a Windows computer with MATLAB (The MathWorks Inc.). Then using E-prime (Psychology Software tools, Inc., https://www.pstnet.com/eprime.cfm) software, the stimuli were embedded into and event-related fMRI paradigm and displayed through an MR-compatible Avotec LCD projection system. The projector was located at the rear of the scanner room, and it projected the images onto a translucent screen attached to the inside of the bore. The subjects viewed the projected images via a mirror mounted over the subjects' eyes, with a total viewing distance of 113 to 115cm. Since the screen position inside the scanner was fixed, the possible variability was the distance from the mirror to the subjects' eyes. We measured the distance from the mirror to the center between eyes for each subject, and the estimated mean total viewing distance across all subjects was approximately 114cm. The up-down range (height) of the screen subtended 10.5º of visual angle, and the screen width subtended 13º of visual angle. The stimuli consisted of six different sizes of rightward drifting gratings and a white cross fixation. Six varying sizes of moving sine wave gratings (Gabor patch) [146] over the receptive field were used to localize magnocellular LGN cells and evaluate the feedback effects on magnocellular LGN cells. The drifting Gabor patch stimuli were 50% luminance contrast, vertical black and white sinusoid grating with a spatial frequency of 1 cpd (cycle per degree). To maintain the comparability, 60 Hz display refresh rate, 25 Hz frame rate, a constant stimulus horizontal velocity of 2.1º s^{-1} and constant screen brightness were used for all subjects. The outer borders of the patches faded into gray to avoid sharp edge effects. In order to get center-surround interaction, we had six varying sizes of patches corresponding to 0.25º, 0.5º, 0.75º, 1º, 2º, 3º of visual angle (illustration shown in Figure 4.1). A centered white cross fixation was used between the patch stimuli, and it subtended 0.1º of visual angle. The background was a gray screen. For each run, the display sequence of the six patches were randomized, and each patch size was repeated 6 times and shown for 5 seconds.

The interval time for fixation between patches was randomized between 9 and 12 seconds (Figure 4.1). A video of the stimulus is included as a supplementary file. In summary, for each subject, there were two runs, and 36 stimuli were shown in each run lasting around 10 minutes.

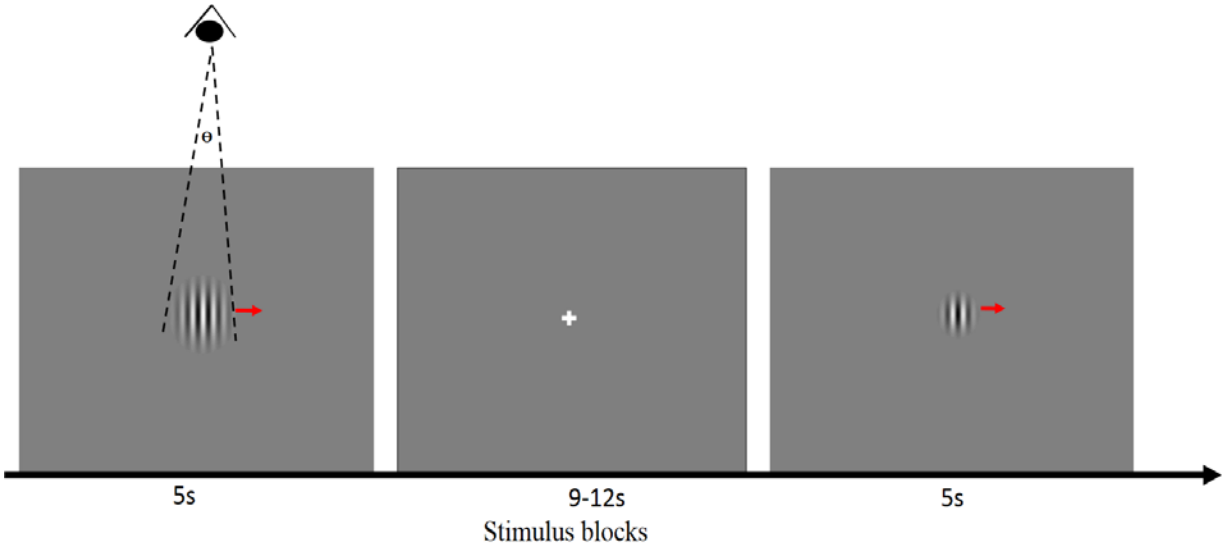

Figure 4.1 *An illustration of the experimental design. The visual stimuli consisted of six varying sizes of rightward drifting Gabor patches (θ = 0.25º, 0.5º, 0.75º, 1º, 2º, 3º) and a white cross fixation. Each Gabor patch was displayed for 5 seconds and the intervals were randomized to 9~12 seconds.*

4.2.3 MRI Data Acquisition

High-resolution whole-brain anatomical images were acquired on a 7T Siemens MAGNETOM scanner with a 32-channel head coil by Nova Medical. The whole-brain high resolution three-dimensional (3D) MPRAGE sequence used the following parameters: 256 slices, voxel size: 0.6mm×0.6mm×0.6mm, TR/TE: 2200/2.8ms, 7º flip angle, base/phase resolution: 384/100%, in-plane phase-encode acceleration factor (iPAT) GRAPPA acceleration factor of 2, FOV read/ phase: 240mm/100%, bandwidth: 270Hz/Px, ascending acquisition.

Two separate high-resolution BOLD runs were obtained with a T2* weighted single-shot multiband gradient-echo echo planar imaging (EPI) sequence with the following parameters: 45 slices acquired parallel to the AC-PC line, voxel size: 0.7 mm× 0.7 mm× 1.5 mm , TR/TE: 1500/31ms, 70º flip angle, FOV read 220mm, base/phase resolution of 260/100%, the anterior-to-posterior phase encoding direction, in-plane phase-encode acceleration factor (iPAT) GRAPPA acceleration factor of 3, multiband (MB) slice acceleration factor of 3, partial Fourier of 6/8, echo spacing of 1ms, interleaved acquisition, 366 measurements.

Before entering the scanner, the subjects were instructed to pay attention to the drifting of the Gabor patch. Inside the scanner, subjects laid their head in supine position with foam padding around the head to reduce head motion. To reduce fatigue effects, we gave the subjects 5 minutes rest with eyes closed inside the scanner between two fMRI runs. No data was acquired during this resting period.

4.2.4 Laminar surface reconstruction using high-resolution anatomical MRI

To extract laminar functional MRI data, we need to first obtain cortical laminar profiles from anatomical MRI since it could provide better brain structural information. A very popular way to reconstruct cortical surface is using FreeSurfer's (http://freesurfer.net/) automatic reconstruction pipeline [43]. However, this pipeline conforms the data to an isotropic resolution of $1mm^3$. Because our MRI data had an isotropic resolution of $0.6mm^3$, we applied Lüsebrink's method [47] to process our $0.6mm^3$ isotropic resolution data. This method avoids downsampling high-resolution MRI data ($<1mm^3$) through software modification of FreeSurfer's standard processing pipeline. We then reconstructed white matter surface and pial surface based on original

MRI resolution of 0.6mm^3. Laminar profiles were then extracted within the cortical gray matter surface. They were constructed at fixed relative distance between the white and pial surfaces, determined from cortical thickness [24]. Two intermediate laminar surfaces were located at 10% and 50% of cortical thickness away from the white matter surface (Figure 4.2(a)(b)), corresponding to layer VI and layer IV separately. The primary visual cortex was automatically identified with the FreeSurfer high-resolution data analysis pipeline [163]. The location of the primary visual cortex was predicted by the cortical folds in a surface coordinate system.

4.2.5 Functional MRI analysis

The pre-processing steps for fMRI data followed standard procedures routinely employed for task fMRI data. All functional volumes from each run were aligned to the first volume to correct head motion using FSL software's MCFLIRT functionality [37], [164]. Brain Extraction Tool (BET) was also used to remove non-brain tissues of functional images [165]. Then the time series from each voxel was detrended to remove low-frequency noise and slow drift using a high-pass temporal filtering (Gaussian-weighted least-squares straight line fitting, with sigma=45s).

The statistical analysis to detect activated brain regions was carried out using FILM (FMRIB's Improved Linear Model) functionality with local autocorrelation correction in FSL software [166]. The general linear modeling (GLM) method was used to estimate the response of each voxel to six different visual stimuli separately with a double-gamma HRF assumption for each single session. Z statistic images were thresholded using clusters determined by $Z>2.3$ and a (corrected) cluster significance threshold of $p<0.05$. The single-session first-level Z statistic maps were in each individual subject's coordinate space.

Since there were two separate task runs for each subject, we performed between-session higher-level analysis to estimate each subject's mean response. The estimated responses of each voxel in each subject's brain to the six different sizes of drifting Gabor patches corresponded to six distinct beta activation images (parameter estimate or PE images), respectively. The between-session mean PE maps for each subject is in standard MNI 1 mm^3 space. These between-session PE maps would only be used later to localize magnocellular neurons in LGN. Once the magnocellular LGN were localized, they were transformed to individual space and all further analysis was carried out in individual subject space.

4.2.6 Laminar functional data analysis in the primary visual cortex

To enable time series extraction or statistical analysis from these intermediate surfaces, it is essential to align the EPI volume to these surfaces. Here we employed boundary-based registration (BBR) method [50] in order to achieve this. It identified the boundary interface between gray matter and white matter from EPI volumes and then calculated a 12 degrees of freedom affine transformation, which registered the boundary interface in EPI to the corresponding white matter surface, reconstructed from high-resolution anatomical MRI data. Careful manual inspections were carried out to check the accuracy of the registration, and were manually edited when necessary.

The single-session thresholded Z statistic images obtained from all the six conditions were then transformed onto two intermediate reconstructed surfaces (they were located at 10% and 50% of the cortical thickness away from the white matter surface, corresponding to layers VI and IV, respectively) separately with the transformation matrix calculated above. Two corresponded z

statistic surfaces were then masked with the primary visual cortex region (Figure 4.2(c)), which was obtained from FreeSurfer [163].

For each session of each subject, two patches of cortical surface containing significantly activated clusters within the left or right primary visual cortex were identified and extracted from each intermediate surface, and flattened using a near-isometric flattening algorithm (Figure 4.2 (d) (e)) [167]. Then we were able to extract and analyze time series from each flat patch ROI on each intermediate surface within the primary visual cortex. In summary, we extracted time series from activated regions of left and right primary visual cortex separately for layer IV and layer VI. This analysis was performed in native subject space.

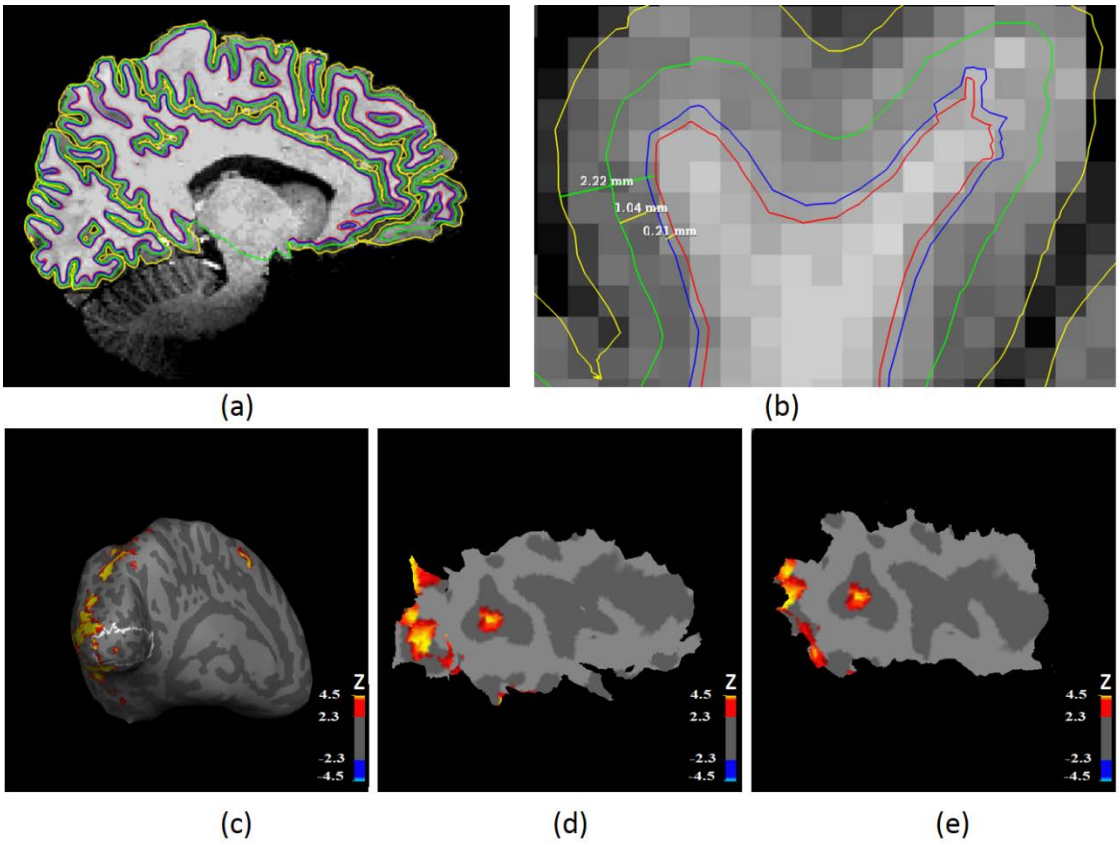

Figure 4.2 *Illustration of surface-based laminar analysis. (a) Four laminar profiles overlaid on the original volume: white matter surface (red contour), layer VI surface of primary visual cortex (blue contour), layer IV surface (green contour), pial surface (yellow contour). (b) A zoomed version of (b) illustrating the layers and their relative distances: the distance between white matter surface to other laminar surfaces was as follows – 0.21mm (from white matter to layer VI, 10% of the thickness), 1.04mm (from white matter to layer IV, 50% of the thickness), and 2.22mm (from white matter to pial surface, 100% of the thickness). (c) Significant activation (Z>2.3 and a corrected cluster significance threshold of p<0.05) overlaid on inflated surface. The white line shows the contour for left the primary visual cortex. (d) A flat patch consisting of significantly activated clusters (Z>2.3, threshold at corrected p<0.05) on layer VI within left primary visual cortex. (e) A flat patch consisting of significantly activated clusters (Z>2.3, threshold at corrected p<0.05) on layer IV within left primary visual cortex.*

4.2.7 LGN ROI definition and analysis

To investigate corticogeniculate feedback, localizing the LGN region of interest (ROI) is very important. This is not trivial since LGN is a very small subcortical region. We first defined an LGN mask based on the Juelich Histological Atlas in MNI152_T1_1mm_brain coordinate space, thresholded at 60% [168]. Because human histological studies have found that the magnocellular layers account for approximately 20% of LGN volumes on average [169] we defined the top 20% of activated voxels with the 1° visual angle stimulus condition to be our left or right magnocellular LGN ROI for each subject separately (Figure 4.4(a) (b)). This specific stimulus condition was chosen because previous invasive studies in animals have shown that the response for 1° is expected to be highest compared with stimuli subtending other angles as it corresponds to the size of the central receptive field for the magnocellular LGN neurons [133], [134], [141], [156], [170]–[173]. To assess the reliability of magnocellular LGN ROIs defined this way, the center coordinate of the left and right magnocellular LGN ROI for each subject was calculated in each spatial dimension (left-right, anterior-posterior, ventral-dorsal). These centers were in MNI152_T1_1mm_brain coordinate space. The relative spatial center (defined as D_x/M_x and D_y/M_y; please refer to Figure 4.4 (b) for a visual illustration of what these quantities mean), was then calculated and plotted as a proportion of the extent away from the center of the LGN mask for left and right brain separately (Figure 4.4 (c)). In principle, the magnocellular LGN center is expected to be close to the ventral direction. If the spatial center is more ventral, we could say the LGN ROI is more likely to be magnocellular LGN.

After the definition of our magnocellular LGN ROIs for each subject, we converted the activation beta (PE) values to percentage change in order to help interpret the results, and then

extracted the mean percentage changes corresponding to each visual stimulus condition (0.25°, 0.5°, 0.75°, 1°, 2° and 3°) from the defined magnocellular LGN ROIs for each subject. At last, the mean time series from magnocellular LGN ROIs was extracted.

4.2.8 Dynamic Granger causality analysis

Granger Causality is a technique used to quantify directional influences between brain regions [115], [174], [175]. The underlying principle is that directional causal influence from region A to region B can be inferred if past values of region A help predict the present and future values of region B [176]. One form of Granger Causality uses multivariate autoregressive models (MVAR) to characterize the predictive relationship between time series [117], [177]–[183]. In the "classical" form of Granger causality used in these previous studies, the model coefficients are independent of time, and hence, the model is "static". Consequently, it does not capture nonstationarities in fMRI time series [184], or the spatiotemporal dynamics of different layers under spontaneous cortical activity and evoked activity [13]. In addition, with static models, it is difficult to delineate the contributions of spontaneous and evoked activity towards the estimated connectivity value. Therefore, we employed a variation of the MVAR model wherein the model coefficients are a function of time[185]–[187]. This allowed us to calculate dynamic Granger causality (DGC) [188], [189]. Specifically, in DGC, coefficients $A(p)$ of the MVAR model are allowed to vary over time[190]–[192], therefore, giving $A(p,t)$ in the model as:

$$Y(t) = A(0,t)Y(t) + A(1,t)Y(t-1) + \cdots + A(p,t)Y(t-p) + E(t)$$

Where *Y(t)* is a matrix containing the *k* different time series, *p* is the model order, *t* is time and *E(t)* is the model error. The diagonal elements $A(0,t)$ are set to zero while the non-diagonal elements model the instantaneous influences between time series to compensate for zero-lag cross correlation effects [53]. The dynamic coefficients are estimated in a Kalman filter framework using variable parameter regression [193], [194]. The DGC is then estimated as [161], [162]:

$$DGC_{ij}(t) = \sum_{n=1}^{p} a'_{ij}(n,t)$$

Where $DGC_{ij}(t)$ is the effective connectivity value from ROI *i* to ROI *j* at a given time point *t*. a'_{ij} are the elements of matrix A.

Recent studies have shown that the variability of hemodynamic response across brain regions can be a confounding factor for Granger causality analysis using raw fMRI time series [52], [53]. Therefore, we performed blind hemodynamic deconvolution of raw BOLD time series to obtain latent neural signals and used them in DGC estimation. This approach has been employed and validated in multiple previous studies[52], [195]–[198]. We employed a recently validated framework based on the Cubature Kalman filter and smoother to invert a nonlinear hemodynamic model [55]. Even though this model is highly parameterized, recent research indicates that it does not overfit the data [56].

In this study, we had six ROIs including layer IV and layer VI of bilateral primary visual cortex, magnocellular LGN ROI for left and right brain separately. After the extraction of average time series from these 6 ROIs, they were deconvolved as mentioned above and input into the DGC model. We obtained a 6×6×366 connectivity matrix (366 time points) for every run of every subject by employing DGC. Finally, DGC values corresponding to specific conditions of interest were populated into different samples, e.g. we grouped all DGC values for 18 time points corresponding to 1º garbor patch condition (6×6×18 matrix) for each run. According to our data, 40 runs were included into our analysis. Therefore, we obtained a 6×6×18×40 connectivity matrix for each experimental condition.

The corticogeniculate feedback pathway from layer VI of primary visual cortex to lateral geniculate nucleus is our primary interest. Therefore, we extracted 720 (18×40) effective connectivity values for each condition. One sample t-test was carried out for each condition. Here we showed the pipeline of the data processing (Figure 4.3).

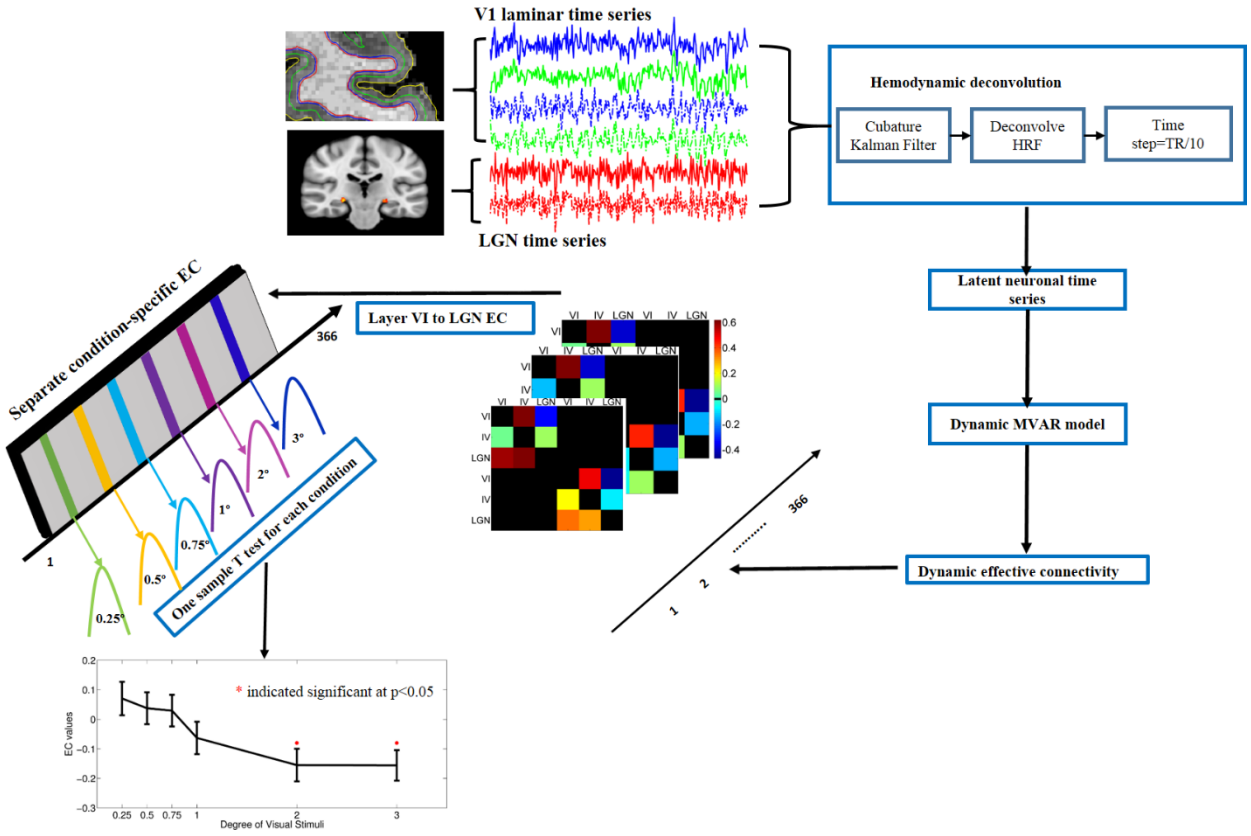

Figure 4.3 *An illustration of the data processing pipeline. First, we performed surface-based laminar analysis including laminar surface reconstruction and the registration of functional MRI data to the laminar surfaces. Second, we extracted mean time series from activated vertexes within each laminar surface and the magnocellular LGN ROIs. Third, blind deconvolution was performed to get latent neuronal time series. Fourth, we utilized the dynamic MVAR model to get dynamic effective connectivity (one directional connectivity matrix for each time point; the connectivity direction is from row to column). Fifth, separation of condition-specific effective connectivity (18×40 EC values for each condition) for a particular path. An example is shown for the path from layer VI to LGN. Finally, we performed one sample T test to determine paths whose strengths significantly differed from zero (red * indicates significant at corrected p<0.05).*

4.3 Results

4.3.1 The validity of the spatial localization of magnocellular neurons in LGN

To assess the reliability of functional location for magnocellular cells within LGN, we calculated the spatial center of magnocellular LGN ROIs in each spatial dimension (left-right, anterior-posterior, ventral-dorsal). These centers were in MNI152 coordinate space. The spatial center was then plotted as a proportion of the extent away from the center of the whole LGN mask (left-right, ventral-dorsal) for left and right brain of each subject separately.

As we can see from Figure 4.4 (c), the group averaged spatial center of activated magnocellular LGN cluster (green cross) is prone to be more ventral for both right and left brain, which is consistent with histological studies. To some extent, this means those activated neurons within LGN are more likely to be magnocellular neurons. So functional localization of magnocellular neurons in LGN with MRI is a feasible method since it matches histological findings obtained from the human LGN [120].

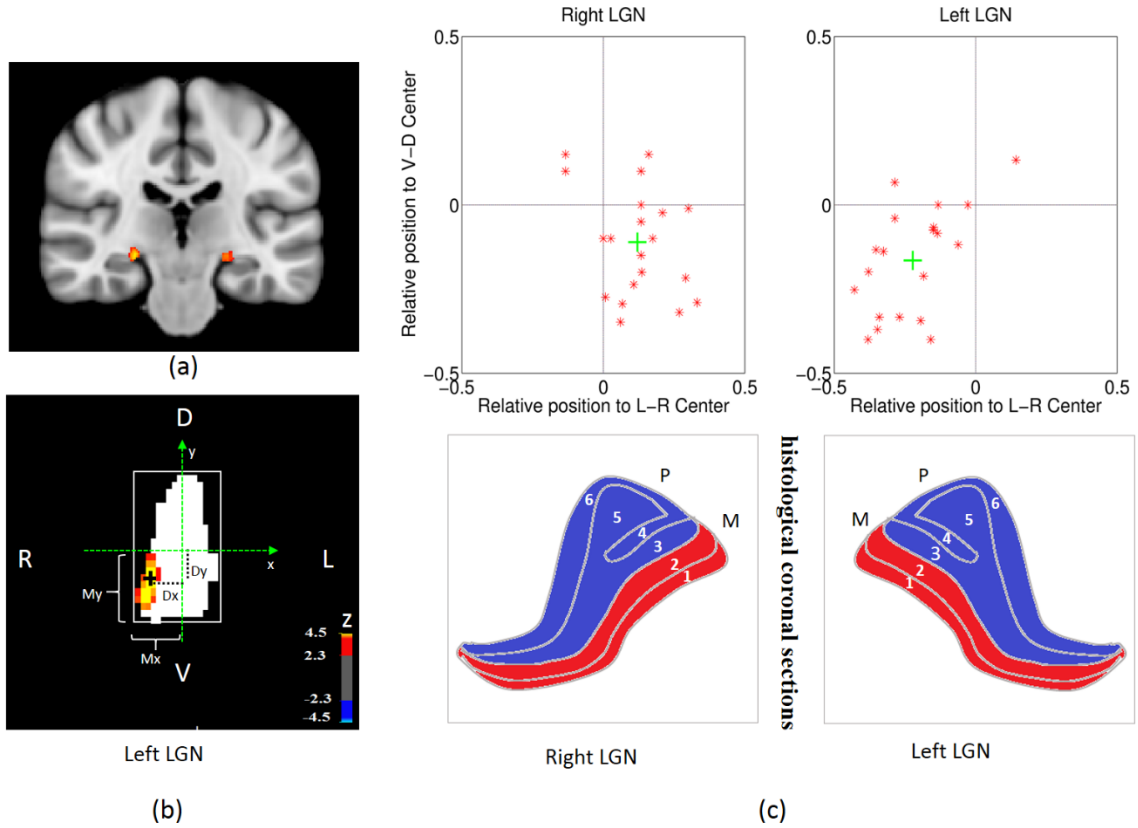

Figure 4.4 *LGN definition and spatial analysis of top 20% activated voxels in LGN. (a) LGN mask from Juelich Histological Atlas (thresholded at 60%) overlaid onto MNI brain template. (b) The top 20% of activated voxels obtained with the 1 ° visual angle stimulus overlaid on the left LGN mask (the white region in (b) corresponds to the LGN mask shown in (a)) for one subject. The relative position of activated voxels is calculated as Dx/Mx and Dy/My where these quantities are depicted in (b). (c)The top panel plots the relative position of Left and Right magnocellular LGN identified in (b) with respect to the center for 20 subjects (red star) and the associated group average (green cross); the bottom panel shows the histological coronal sections of human LGN, the red layers represents magnocellular LGN and blue parts for parvocellular LGN (referred and modified from* [120].

4.3.2 The enhanced center-surround inhibition effect on LGN

In our study, we found enhanced center-surround inhibition effect within human magnocellular LGN. The BOLD response in magnocellular LGN increased with the size of rightward moving Gabor patches until the stimulus tended a 1° angle and then decreased with subsequent increase in the size of the Gabor patch. Here it is noteworthy that a 1° stimulus corresponds to the size of the central receptive field for the magnocellular LGN neurons [133], [134], [173], [199], [200], and hence increasing the size of the patch beyond that meant that it breached in the surrounding receptive field. Consequently, if center-surround inhibition was in place, then increasing the size of the Gabor patch beyond 1 degree should decrease the BOLD response due to surround inhibition. As shown in Figure 4.5 (b) (d), this is exactly what we found. Statistical comparison of the BOLD response elicited from each condition is shown in Table 4.1 (we only show comparisons for $p<0.05$). The results showed that the responses within magnocellular LGN under both 0.75° and 1° visual stimuli were significantly greater than the responses under other conditions (Table 4.1). The maximum center-surround suppression (defined as the difference in BOLD response between 1°, and 2° or 3°, whichever is higher, as in previous studies [133], [134], [201]) at the individual subject level reached up to 59.67% for left magnocellular LGN (subject 4, shown in Figure 4.5(a) and Figure S2) and 78.42% for right magnocellular LGN (subject 13, Figure 4.5(c) and Figure S2). From Figure S2, more than 20% center-surround inhibition (the bigger difference between 1° and 2° or 3° condition) in both left and right magnocellular LGN was found from 13 out of 20 subjects. Previous invasive studies in animals found center-surround inhibition of approximately 20% in magnocellular neurons within the LGN in the absence of negative feedback from the primary visual cortex [157]. Therefore, 20% inhibition represents a null benchmark against which we could compare % inhibition obtained by

us. Though individual differences exist, by and large at the group level, the enhanced center-surround inhibition effect on magnocellular neurons within human LGN is salient and detectable using non-invasive methods such as functional MRI. To our knowledge, this is the first study to detect the enhanced center-surround inhibition in human LGN non-invasively using fMRI.

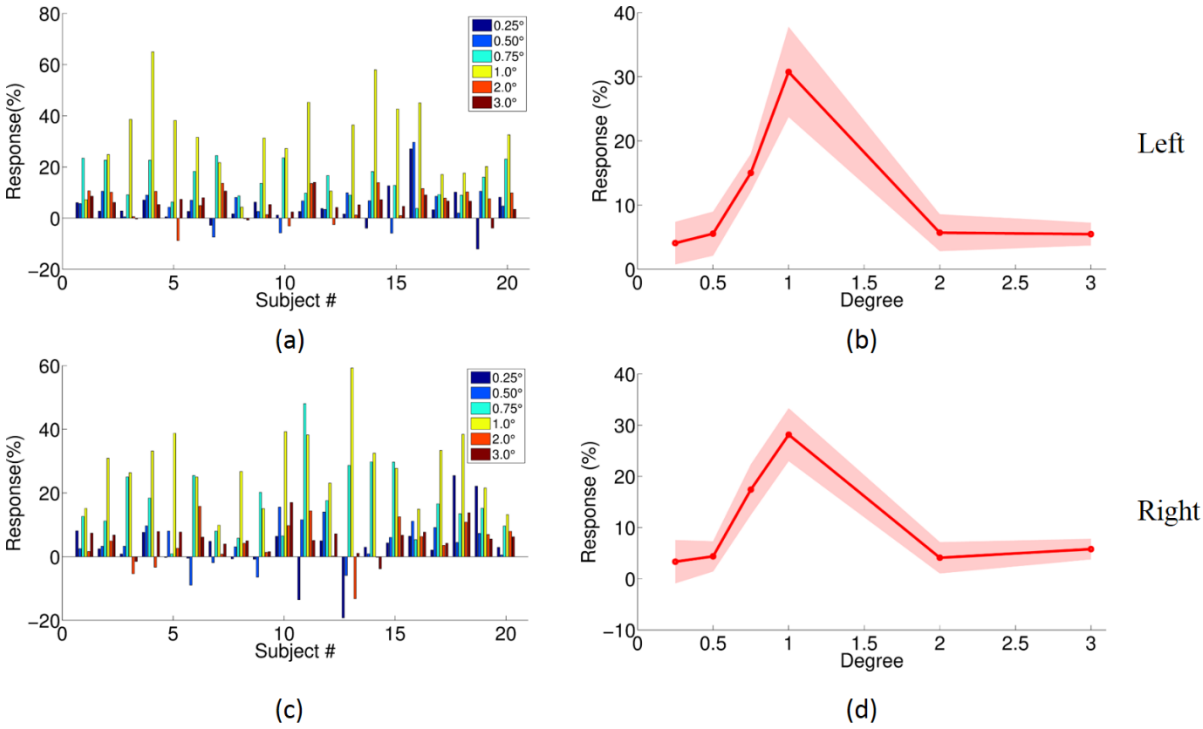

Figure 4.5 *The BOLD response in magnocellular LGN for Gabor patch stimuli. (a)-(b) correspond to left magnocellular LGN, and (c)-(d) right magnocellular LGN. (a, c) the responses of each subject for each visual stimuli (0.25º dark blue, 0.5º blue, 0.75º cyan, 1º yellow, 2º red, 3º dark red), x axis is subject number, and y axis is the response (the percentage of signal change); (b, d) the plot of the mean response over all subjects vs stimulus degree (red line), 95% confidence interval (red shade).*

Paired t test for condition A < condition B at alpha=0.05 in left M type LGN		
A	B	P value
0.25°	0.75°	2.40×10^{-3}
0.5°	0.75°	3.60×10^{-3}
1°	0.75°	3.00×10^{-3}
2°	0.75°	8.99×10^{-5}
3°	0.75°	9.32×10^{-4}
0.25°	1°	2.07×10^{-8}
0.5°	1°	2.07×10^{-8}
2°	1°	2.21×10^{-8}
3°	1°	3.07×10^{-8}

(a)

Paired t test for condition A < condition B at alpha=0.05 in right M type LGN		
A	B	P value
0.25°	0.75°	2.91×10^{-5}
0.5°	0.75°	1.34×10^{-4}
1°	0.75°	2.60×10^{-3}
2°	0.75°	8.86×10^{-5}
3°	0.75°	9.13×10^{-4}
0.25°	1°	2.07×10^{-8}
0.5°	1°	2.07×10^{-8}
2°	1°	2.24×10^{-8}
3°	1°	2.97×10^{-8}

(b)

Table 4.1 *Paired t test between the BOLD responses obtained from different conditions (condition A< condition B) for left (a) and right (b) magnocellular LGN, shown here only for comparisons for which corrected p<0.05. The results showed that the BOLD response within magnocellular LGN for 0.75° and 1° visual stimuli was significantly greater than the responses under other conditions.*

4.3.3 Center-surround inhibition effects in different layers of primary visual cortex

We also found center-surround inhibition in primary visual cortical neurons as shown in Figure 4.6(a) (c) and Table 4.2. The maximum center-surround inhibition (the larger of the difference in responses (1°-2°) or (1°- 3°)), reached up to 54.86% for layer IV, and 53.62 % for layer IV of left primary visual cortex (Figure 4.6 (b), subject 10), 29.92% for layer IV, and 27.84% for layer VI of right primary visual cortex (Figure 4.6(d), subject 11). More than 20% center-surround inhibition was found in 14 subjects within left primary visual cortex (Figure 4.6(b)), and in 10 subjects within right primary visual cortex (Figure 4.6(d)). A comparison of the BOLD response due to different stimulus conditions for layer VI (shown in Tables 4.2(a) and 4.3(a) for left and right primary visual cortex, respectively) and layer IV (shown in Tables 4.2(b) and 4.3(b) for left and right primary visual cortex, respectively) within primary visual cortex showed that the responses for 0.5°, 0.75°, and 1° conditions were significantly greater than the response for 0.25°, 2°, and 3° stimuli. Moreover, the fMRI response in layer IV was stronger than layer VI during the display of six different types of stimuli targeted at the magnocellular visual pathway (Table 4.2 (c) and Table 4.3(c)). In addition, with two-way ANOVA, we assessed the main effects of two different factors—visual stimuli and layer. We found the main effects are both significant, but the interaction between them is not (Table 4.4).

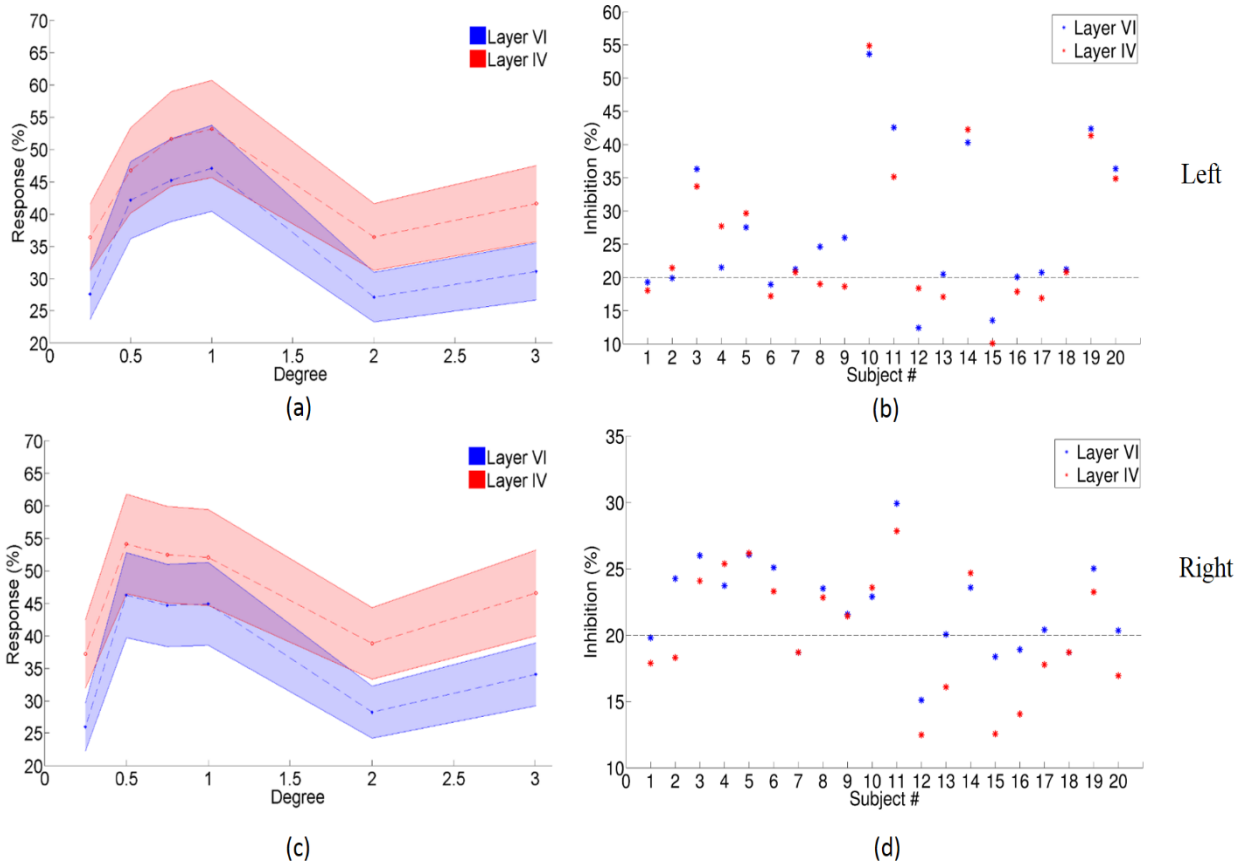

Figure 4.6 *Center-surround inhibition in different layers of the primary visual cortex. Panel (a) shows the results for left primary visual cortex and panel (c) for the right primary visual cortex. In both these panels, mean BOLD response across all subjects (dash line) is plotted on the y-axis and the stimulus degree on the x-axis. The 95% confidence interval is shown as the shadow around the dash line. Red represents layer IV, and blue represent layer VI. Panels (b) and (d) show the center-surround inhibition (the larger of the difference in responses (1°-2°) or (1°- 3°)) in each subject for left and right primary visual cortex, respectively. Here, the red * represents layer IV, and blue * for layer VI.*

Paired t test for condition A <condition B in layer VI of left primary visual cortex		
A	B	P value
0.25°	0.5°	1.98×10^{-7}
0.25°	0.75°	2.07×10^{-8}
0.25°	1°	2.39×10^{-8}
2°	0.5°	3.67×10^{-5}
2°	0.75°	2.07×10^{-4}
2°	1°	2.09×10^{-8}
3°	0.5°	7.18×10^{-6}
3°	0.75°	2.55×10^{-8}
3°	1°	1.87×10^{-7}

(a)

Paired t test for condition A <condition B in layer IV of left primary visual cortex		
A	B	P value
0.25°	0.5°	1.10×10^{-3}
0.25°	0.75°	6.37×10^{-7}
0.25°	1°	5.54×10^{-5}
2°	0.5°	1.00×10^{-4}
2°	0.75°	5.50×10^{-8}
2°	1°	4.06×10^{-6}
3°	0.5°	7.17×10^{-6}
3°	0.75°	2.10×10^{-3}
3°	1°	1.90×10^{-3}

(b)

P value of paired t test for Layer IV >Layer VI under six conditions					
0.25°	0.5°	0.75°	1°	2°	3°
4.71×10^{-12}	7.45×10^{-5}	3.53×10^{-8}	2.39×10^{-8}	5.54×10^{-12}	2.69×10^{-10}

(c)

Table 4.2 *Paired t test between the BOLD responses (corrected $p<0.05$) obtained from different conditions (condition A< condition B) for layer VI (a) and layer IV (b) within left primary visual cortex. (c) Paired t test of the BOLD responses obtained from layers IV and VI under each stimulus condition, within the left primary visual cortex. P-values correspond to paired t-tests conducted to test the following contrast: layer IV>VI at corrected $p<0.05$.*

Paired t-test for condition A < condition B in layer VI of right primary visual cortex		
A	B	p-value
0.25°	0.5°	2.07×10^{-8}
0.25°	0.75°	2.06×10^{-8}
0.25°	1°	2.06×10^{-8}
2°	0.5°	2.06×10^{-8}
2°	0.75°	2.06×10^{-4}
2°	1°	2.05×10^{-8}
3°	0.5°	2.08×10^{-6}
3°	0.75°	2.07×10^{-8}
3°	1°	3.10×10^{-7}

(a)

Paired t test for condition A <condition B in layer IV of right primary visual cortex		
A	B	p-value
0.25°	0.5°	2.44×10^{-8}
0.25°	0.75°	2.10×10^{-8}
0.25°	1°	2.28×10^{-6}
2°	0.5°	2.13×10^{-8}
2°	0.75°	4.87×10^{-7}
2°	1°	2.07×10^{-8}
3°	0.5°	1.19×10^{-4}
3°	0.75°	1.65×10^{-5}
3°	1°	4.60×10^{-3}

(b)

P-value of paired t test for Layer IV >Layer VI under six conditions					
0.25°	0.5°	0.75°	1°	2°	3°
1.50×10^{-14}	8.06×10^{-9}	1.49×10^{-9}	9.75×10^{-9}	1.24×10^{-14}	5.84×10^{-12}

(c)

Table 4.3 *Paired t test between the BOLD (corrected $p<0.05$) responses obtained from different conditions for layer VI (a) and layer IV (b) within right primary visual cortex. (c) Paired t test of the BOLD responses obtained from layers IV and VI under each stimulus condition, within the right primary visual cortex. P-values correspond to paired t-tests conducted to test the following contrast: layer IV>VI at corrected $p<0.05$.*

	Left Primary Visual Cortex	Right Primary Visual Cortex
Visual Stimuli Factor	3.02×10^{-14}	3.10×10^{-14}
Layer Factor	2.07×10^{-6}	9.97×10^{-20}
Interaction	0.87	0.40

Table 4.4. *Two-way ANOVA F test results (P value) for left and right primary visual cortex separately. The two main factors— visual stimuli, layer, are both significant, but the interaction between them is not.*

4.3.4 Dynamic effective connectivity

The major goal of this study was to determine whether the effective connectivity determined from layer-resolved fMRI in humans is sensitive to the negative feedback from layer VI of primary visual cortex to magnocellular LGN. This negative feedback has been previously indicated by invasive animal studies [133], [134], [173], [202], and is known to cause enhanced center-surround inhibition effect on magnocellular LGN (demonstrated in the previous section). Additionally, we also wanted to investigate the feedforward pathway from magnocellular LGN to layers IV and VI in the primary visual cortex as well as that from layer IV to layer VI within the primary visual cortex (shown in Figure 4.6). Therefore, we investigated whether these pathways can be inferred by employing dynamic effective connectivity modeling of layer-resolved human fMRI data.

As described in the methods section, we obtained 720 (18×40, 18 time points for each run, 40 runs) different effective connectivity values for each pathway under each condition. We specifically extracted all effective connectivity values for corticogeniculate feedback pathway and the three feedforward pathways under six conditions only in subjects who showed center-surround inhibition in their BOLD response above 20%. First, primary visual cortex layer VI to magnocellular LGN corticogeniculate feedback pathway was investigated under six different conditions. One sample t-tests (stimulus > rest) were conducted for all six conditions, however, we found this feedback pathway to be significantly negative only for the 2º and 3º conditions (Figure 4.7 (c)). Under 2º condition, mean connectivity was -0.155, $t(719) = -3.2142$, $p = 0.0014$; and under 3º condition, mean connectivity of -0.154, $t(719) = -2.6536$, $p = 0.0083$ were observed. This demonstrates that this negative feedback pathway is significantly enhanced when the receptive field of the visual stimuli exceed its center (which happens when the Gabor path tends an angle of 2º or more), and corroborates the sharp drop in BOLD response observed in magnocellular LGN (Figure 4.5).

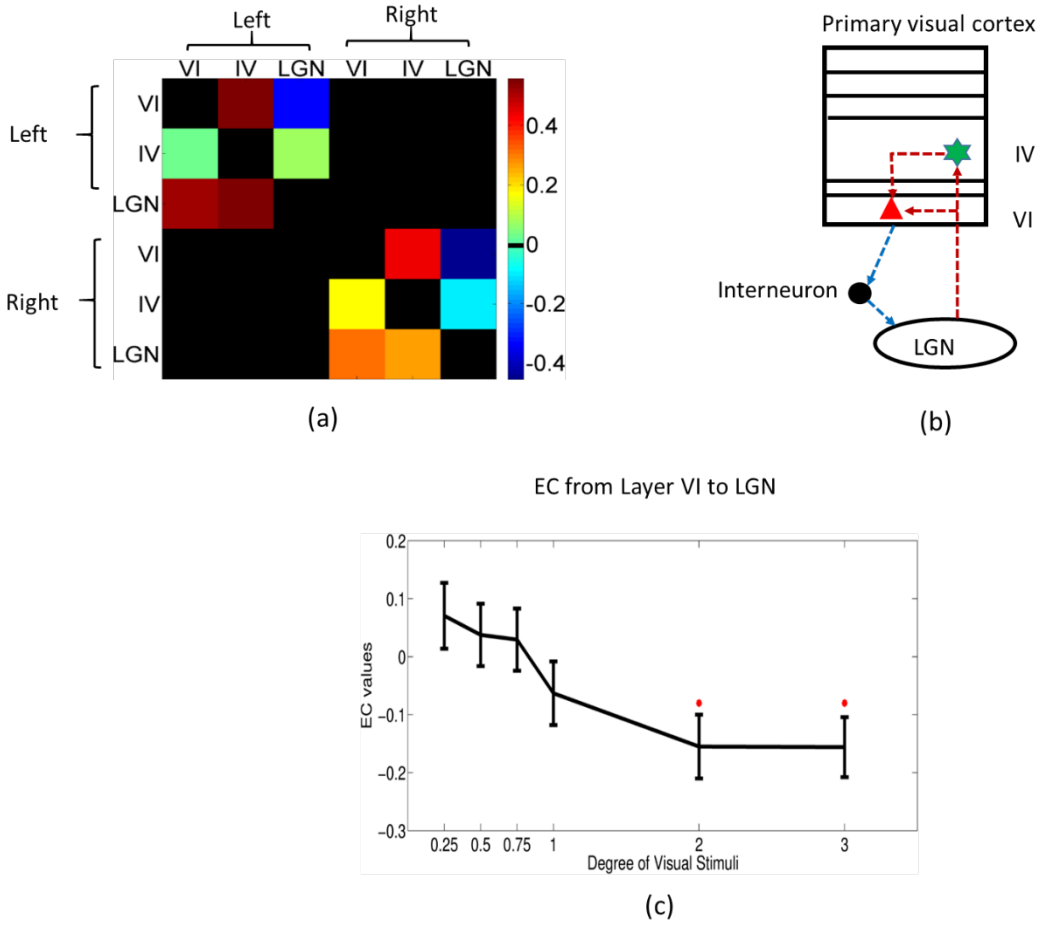

Figure 4.7 *Dynamic effective connectivity results. (a) One example of the connectivity matrix at a given time point, the direction is from row to column, e.g., the left corticogeniculate feedback pathway from layer VI to LGN corresponds to first row/third column, and the left feedforward pathway from layer VI to IV corresponds to first row/second column. (b) An illustration of the neuronal circuits involving LGN and primary visual cortex: the black round shape represents inhibitory interneuron, the red triangle is a neuron in layer VI of primary visual cortex, and the green star is a neuron in layer IV. The blue dotted line represents the negative feedback pathway, and the red dotted lines are the feedforward pathways (LGN→IV, LGN→VI, and IV→VI). (c) Mean/standard errors of effective connectivity values vs stimulus degree for corticogeniculate feedback pathway from layer VI to LGN. This pathway is only significantly smaller than zero under 2º and 3º conditions. The red star indicated significance at corrected p<0.05.*

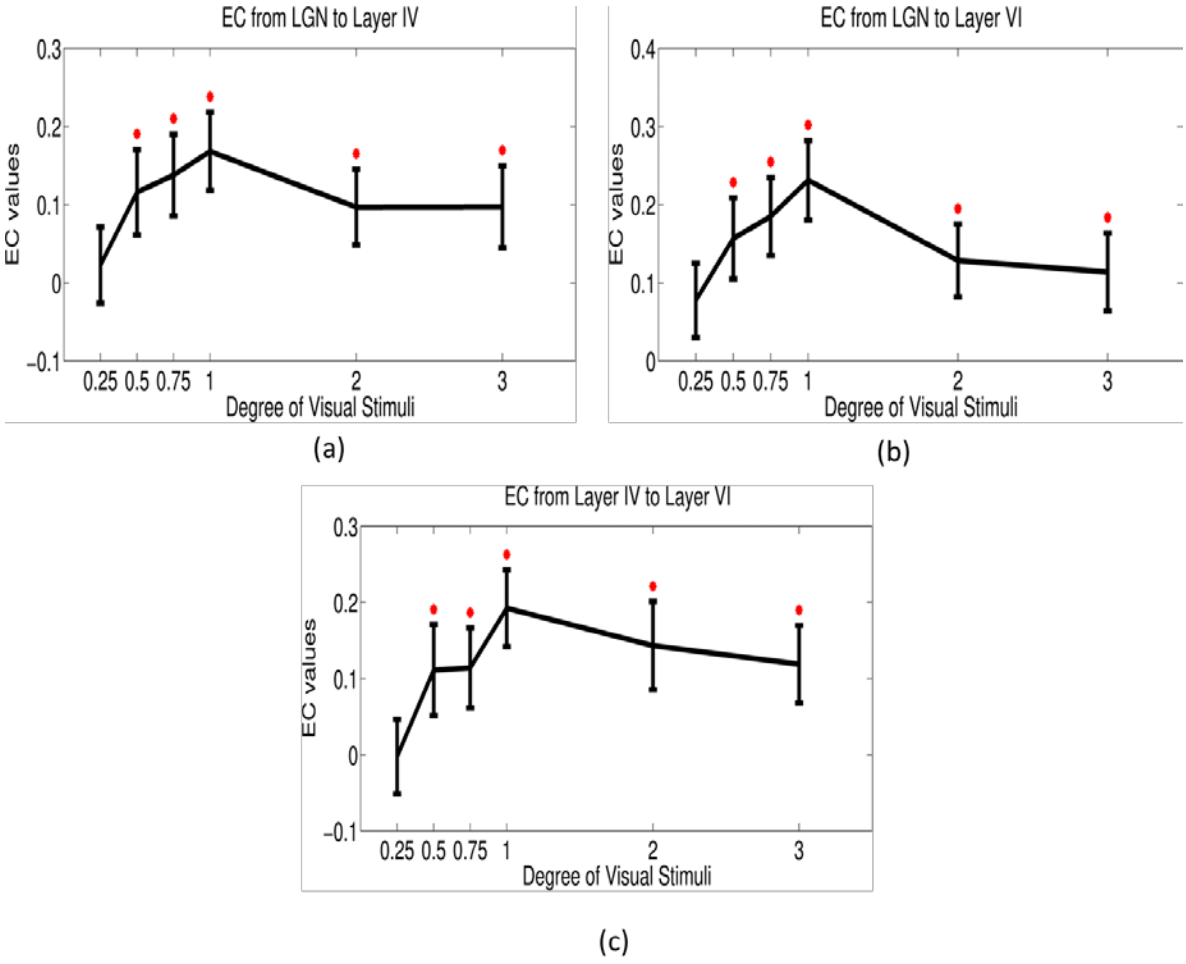

Figure 4.8 *Mean/standard errors of effective connectivity values vs stimulus degree for feedforward pathway from LGN to layer IV in the primary visual cortex (a), LGN to layer VI (b), and layer IV to VI (c).*

Subsequently, we performed a similar one sample t-test for the feedforward pathways – from LGN to layers IV and VI in the primary visual cortex, and from layer IV to VI within the primary visual cortex (Figure 4.8). We found these positive feedforward pathways to be significantly greater than zero for all conditions except 0.25º condition. This pattern mimicked that of the BOLD response within the magnocellular LGN and the primary visual cortex wherein the connectivity increased from 0.25 º condition onwards, peaking at 1 º condition and then decreasing.

4.4 Discussion

The results presented in the previous section point to the following conclusions that we will discuss here: (1) functional localization of magnocellular neurons in LGN with high-resolution (<1mm) fMRI has been demonstrated to be a feasible method; (2) the enhanced center-surround inhibition effect on magnocellular neurons within human LGN is salient and detectable using BOLD responses within the magnocellular LGN to moving Gabor patch stimuli of different sizes, being shown here for the first time in literature; (3) with high-resolution, layer-specific fMRI at ultra-high fields, the effective connectivity determined from laminar fMRI is sensitive to the corticogeniculate negative feedback pathway from layer VI of primary visual cortex to magnocellular LGN, and the-feedforward positive pathways from magnocellular LGN to layers IV and VI of the primary visual cortex as well as from layer IV to layer VI within the primary visual cortex. To our knowledge, this is the first study to investigate whether fMRI-based effective connectivity can be used to investigate the directional information flow between regions at submillimeter spatial scale (and more specifically in the corticogeniculate pathway).

Many previous studies have tried to use noninvasive methods such as fMRI to functionally localize small subcortical regions such as the LGN in the human brain [152], [203]–[209]. However, only few of those studies have been successful in identifying the magnocellular part of LGN [152], [208], [210]. These studies attempted to classify the magnocellular and parvocellular voxels in LGN based on the contrast sensitivity difference – magnocellular LGN response saturates under monochrome, high luminance contrast visual stimuli, and parvocellular LGN is more suited for visual stimuli with high color contrast and low luminance contrast [127]. Besides, the voxel size used in these studies was around 2 mm^3, which is pretty large compared to the size of M-type and P-type parcels within LGN. In this project, we designed specific visual stimuli, which could maximally activate, and help localize the magnocellular voxels in LGN with our whole-brain submillimeter fMRI data. We validated the location of magnocellular LGN using expected spatial position obtained from previous from histological findings [169].

Noticeably, this is the first study to detect enhanced center-surround inhibition effect in magnocellular neurons within human LGN using fMRI. The maximum center-surround inhibition could reach up to 59.67% for left magnocellular LGN and 78.42% for right magnocellular LGN in individual subject; however, the group mean center-surround suppression was only up to 26.52%. It did not reach up to 70% suppression observed in previous invasive animal studies [133], [211], in which single-unit recording was used to measure the inhibition from multiple neurons. In contrast, with ultra-high resolution fMRI, the inhibition is estimated from a small cluster, which may contain thousands of neurons. Therefore, the inability to accurately localize magnocellular neurons with fMRI (which is not surprising given that even the smallest voxel size achievable with fMRI is an order of magnitude larger than that needed to accurately localize magnocellular neurons) may have played a part in the magnitude of center-surround inhibition we observed. However, it

is still very impressive that we were able to observe enhanced center-surround inhibition in human magnocellular LGN using fMRI.

Previous invasive studies have found a dense network of feedforward and feedback projections between LGN and primary visual cortex [118]–[124], [137]–[141]. After neurons in LGN receive the visual input, feedforward pathways would relay it to layers IV and VI of the primary visual cortex. The feedback pathway consists of corticogeniculate neurons in layer VI projecting onto the magnocellular neurons in the LGN via inhibitory interneurons. In this work, we employed a dynamic effective connectivity model to reveal the directional information flow for the feedforward and feedback pathways, with high-resolution, layer-specific fMRI data. We found negative corticogeniculate feedback pathway from layer VI to magnocellular LGN (Figure 4.7) when the angle subtended by the Gabor patch stimulus was larger than the central visual field, thereby facilitating center-surround inhibition. This might explain the sharp drop in the BOLD response we observed in magnocellular LGN for larger Gabor patches (Figure 4.5).

We also found positive feedforward pathways from magnocellular LGN to layers IV and VI of the primary visual cortex as well as from layer IV to layer VI within the primary visual cortex (Figure 4.8). It is interesting to note that those feedforward pathways mimicked the center-surround pattern of BOLD response observed in LGN. Therefore, we speculate that this might be a mechanistic explanation for how the response in one brain region is propagated to another, specifically from LGN to primary visual cortex in our case.

These findings indicate that layer VI of the primary visual cortex has a crucial role in controlling the gain of brain activity involved with vision. The tuning of gain in the corticogeniculate control system is achieved by both feedback and feedforward pathways anchored by layer VI in the primary visual cortex. Similar conclusions about gain control by layer VI were

reached by Olsen et al by performing invasive electrical recordings in mice by using a technique that can selectively label neurons in layer VI [141]. It is very encouraging that it is now possible to derive mechanistic insights about cortical micro-circuits using fMRI that agree with the gold standard in neuroscience, viz. invasive single unit recordings.

Our framework is domain-neutral, i.e. the cortical laminar separation and subcortical segmentation are based on the whole brain for each individual. Further, the connectivity model was agnostic about the context in which it was applied and was not fine-tuned in any way to suit the network we were trying to characterize. The only part of the analysis pipeline that was not domain-neutral was the experimental and analysis paradigm used to localize magnocellular neurons in the LGN. Therefore, our framework could potentially be used investigate the laminar connectional architecture anywhere in the human brain as long as an experimental paradigm is developed to localize the regions/layers of interest using high resolution fMRI. For example, future studies could potentially investigate the laminar connections between Broca's area to language-related thalamic nuclei. Broca's area and language-related thalamic nuclei are connected in two parallel layer-specific pathways: one thalamic pathway targets the middle cortical layers in Broca's area, and the other project to cortical layer I. The feedback pathway from Broca's area to thalamic nuclei originate from cortical layers V and VI. Neuroimaging studies could investigate these pathways from aphasic patients with damage to the thalamic nuclei [112]. The language function is unique to humans (like many other social and cognitive functions), and therefore, it is not possible to investigate such layer-specific functional microcircuits with invasive studies in animals.

Limitations and Future Work

Laminar effective connectivity may provide novel insights into cortical microcircuits in the human brain connectome, however, a few limitations of this study need to be addressed in future laminar fMRI effective connectivity related research. First, different methods to differentiate cortical lamina from MRI exist. We can construct laminar surfaces by a method called equidistant laminae, which keeps a relatively fixed distance to cortical boundaries [25], [48], [49]. In this study, we employed this method. Laminar surfaces can also be constructed along equipotentials, which are computed between the inner white matter surface and pial surface with Laplace equation [110]. Moreover, a new model called equal-volume model for identifying cortical laminae was proposed by Waehnert and colleagues [111]. In future, studies must compare the three different models for how well connectivity derived from layers constructed by them match the underlying anatomical predictions.

Second, the spatial point spread function (PSF) of the BOLD response at different layers presents poor laminar specificity since the draining blood flows along the intracortical veins (ICV) (ICVs are perpendicular to the surface) into pial veins on the pial surface [89]. This shows that the lower layers always contribute signal to the upper layers. The traditional method to resolve this issue is to interpolate fMRI signal at certain cortical depth, and then average the surface profiles [24], [25], [33]. The fact that we performed hemodynamic deconvolution before connectivity analysis also helps in removing some of the contributions of vasculature. But we need to come up a better model to extract laminar signals to increase the spatial specificity of fMRI. Future studies may employ spin echo sequences to investigate whether it is better for laminar fMRI analysis since the PSF for spin-echo EPI is more localized than gradient-echo EPI [89]. While one may lose

sensitivity by using spin echo, the tradeoff between the sensitivity lost by spin echo and the spatial precision gained by its sharper PSF must be investigated.

Third, despite of the small size of LGN, the spatial organization of the magnocellular neurons in LGN in our study exhibited expected distribution from previous histological studies, i.e. the spatial center was distributed towards the ventral direction [169]. Previous studies have investigated the ability of fMRI to localize magnocellular regions within human LGN[152], [208], however, the spatial resolution of these fMRI studies was pretty coarse (>1mm). In this study, we acquired fMRI data with $0.7mm^2$ in plane resolution, and validated the reliability of magnocellular LGN distribution across 20 subjects. Still, there are some aspects that could be improved. Since our voxel size was not isotropic, the partial volume effects could be one confounding factor, i.e. a single voxel could potentially contain both magnocellular neurons and parvocellular/koniocellular neurons. In such a scenario, the response from one single voxel could be a mixture of signals from different types of neurons. Future studies need to use higher spatial resolution to reduce partial volume effects at 7T. This could potentially be done using approaches which restrict the field of view to include just the LGN and the primary visual cortex (more generally, just the structures of interest in the pathways being investigated). We did not use this approach because the FreeSurfer analysis pipeline for surface-based analysis requires whole brain coverage. However, it should be possible in principle to implement this pipeline using data with limited coverage and field of view. Also, we defined top 20% of activated voxels as our magnocellular neurons in this study. While this choice was indeed conservative, the proportion has been shown to vary across individuals [169], [212]. Therefore, future studies could potentially use multiple alternative MR contrasts such as susceptibility, proton density and myelination in order to fine-tune the functionally defined magnocellular LGN region.

Fourth, effective connectivity analysis using dynamic granger causality (DGC) suffers from the poor temporal resolution of fMRI. Although we performed hemodynamic deconvolution to recover the latent neuronal signals before applying Granger causality, it is still hard to infer neuronal latency from fMRI data, which is sampled coarsely in time. In future work, simultaneous EEG and fast laminar fMRI may be fused together to improve temporal precision of fMRI at the layer level. Recent studies have shown that it is possible to obtain EEG simultaneously with fMRI sampled at 600 ms using the multiband EPI sequence [213]. With higher acceleration factors, one could potentially acquire fMRI with sampling periods less than half a second and this will likely improve the performance of DGC [114] for inferring directional interactions within the human brain at the laminar level.

4.5 Supplementary Materials

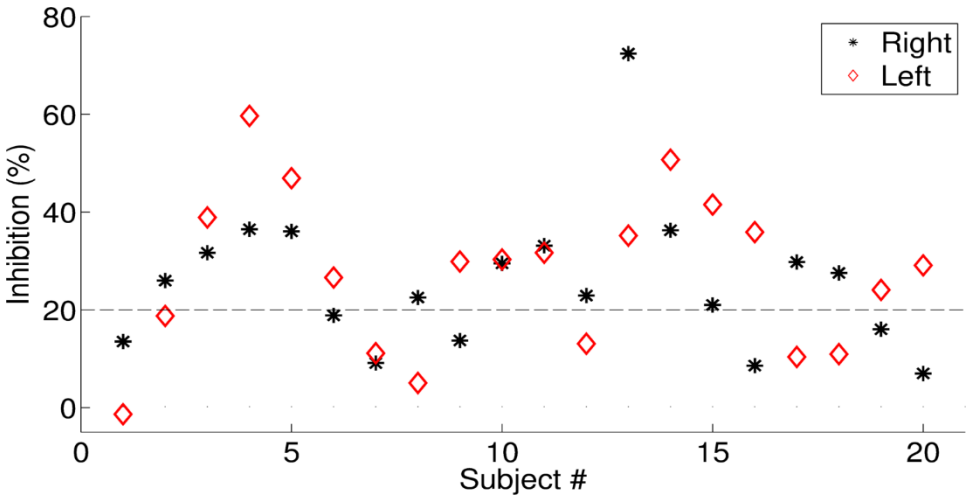

Figure S2 *The maximum center-surround inhibition of left (*) and right (◊) magnocellular LGN for each subject. More than 20% center-surround inhibition (the bigger difference between 1° and 2° or between 1°and 3º condition) in both left and right magnocellular LGN was found in 13 out of 20 subjects.*

Chapter 5 Conclusions

The purpose of this dissertation is to employ high-resolution fMRI to investigate the sensitivity of layer-specific connectivity methods to connectional architecture at sub-millimeter spatial scale under different brain states in human. We employed two different connectivity methods– functional connectivity and effective connectivity, to successfully uphold the fact that layer-specific connectivity analysis with high-resolution functional MRI can be a potential and powerful technique to unveil the connectional architecuture in human brain at laminar level.

For layer-specific functional connectivity analysis under resting state, we applied a surface-based laminar analysis pipeline available in FreeSurfer to process high-resolution anatomical data with a 0.6mm isotropic resolution and to delineate the six layers of the cortex. To investigate whether FC is sensitive to layer-specific connectional architecture, we examined this aspect with high-resolution resting state fMRI data (voxels with 0.85mm in-plane resolution) obtained at 7T. A simple blind deconvolution technique was used to obtain the latent neural signals for each vertex from each layer. Specifically, we tested two hypotheses derived from previous invasive anatomical studies: 1) FC between the entire thalamus and cortical layers I and VI was significantly stronger than between the thalamus and other layers. Further, FC between somatosensory thalamus (ventral posterolateral nucleus, VPL) and layers IV, VI of the primary somatosensory cortex were stronger than with other layers; 2) Inter-hemispheric cortico-cortical FC (i.e. between the left and right brain regions of the same area) in superficial layers (layer I-III) must be higher compared to deep layers (layer V-VI). We found that resting state functional connectivity at the laminar level, to a great extent, were in sync with the hypotheses stated above. To our knowledge, this is the very

first study to successfully investigate the sensitivity of resting state fMRI connectivity at submillimeter spatial scale to the connectional architecture at the laminar level.

For layer-specific effective connectivity analysis under different visual conditions, we proposed an experimental and analysis framework, which enables noninvasive functional characterization of layer-specific cortical microcircuits. Specifically, we illustrate this framework by characterizing layer-specific functional pathways in the corticogeniculate network of the human visual system by obtaining sub-millimeter fMRI at 7T using a task that engages the magnocellular pathway between LGN and the primary visual cortex. Our results showed that: (1) functional localization of magnocellular neurons in LGN with high-resolution (<1mm) fMRI has been demonstrated to be a feasible method; (2) the enhanced center-surround inhibition effect on magnocellular neurons within human LGN is salient and detectable using BOLD responses within the magnocellular LGN to moving Gabor patch stimuli of different sizes, being shown here for the first time in literature; (3) with high-resolution, layer-specific fMRI at ultra-high fields, the effective connectivity determined from laminar fMRI is sensitive to the corticogeniculate negative feedback pathway from layer VI of primary visual cortex to magnocellular LGN, and the feedforward positive pathways from magnocellular LGN to layers IV and VI of the primary visual cortex as well as from layer IV to layer VI within the primary visual cortex. To our knowledge, this is the first study to investigate whether fMRI-based effective connectivity can be used to investigate the directional information flow between regions at submillimeter spatial scale (and more specifically in the corticogeniculate pathway).

Bibliography

[1] S. Ogawa, T. M. Lee, A. R. Kay, and D. W. Tank, “Brain magnetic resonance imaging with contrast dependent on blood oxygenation.,” *Proc. Natl. Acad. Sci. U. S. A.*, vol. 87, no. 24, pp. 9868–72, 1990.

[2] N. K. Logothetis, “The neural basis of the blood-oxygen-level-dependent functional magnetic resonance imaging signal,” *Philos. Trans. R. Soc. B Biol. Sci.*, vol. 357, no. 1424, pp. 1003–1037, 2002.

[3] G. K. Aguirre, E. Zarahn, and M. D’esposito, “The variability of human, BOLD hemodynamic responses.,” *Neuroimage*, vol. 8, no. 4, pp. 360–9, Nov. 1998.

[4] V. B. Mountcastle, “The columnar organization of the neocortex.,” *Brain*, vol. 120, no. 4, pp. 701–722, 1997.

[5] R. J. Douglas and K. A. C. Martin, “Neuronal Circuits of the Neocortex,” *Annu. Rev. Neurosci.*, vol. 27, no. 1, pp. 419–451, 2004.

[6] I. Ferrer, I. Fabregues, and E. Condom, “A Golgi study of the sixth layer of the cerebral cortex. I. The lissencephalic brain of Rodentia, Lagomorpha, Insectivora and Chiroptera.,” *J. Anat.*, vol. 145, pp. 217–234, 1986.

[7] C. D. Gilbert, “Microcircuitry of the visual cortex.,” *Annu. Rev. Neurosci.*, vol. 6, pp. 217–247, 1983.

[8] D. H. Hubel and T. N. Wiesel, “Receptive fields, binocular interaction and functional architecture in the cays visual cortex.,” *J. Physiol.*, vol. 160, pp. 106–154, 1962.

[9] Z. W. Zhang and M. Deschênes, “Intracortical axonal projections of lamina VI cells of the primary somatosensory cortex in the rat: a single-cell labeling study.,” *J. Neurosci.*, vol. 17, no. 16, pp. 6365–6379, Aug. 1997.

[10] L. C. Katz, “Local circuitry of identified projection neurons in cat visual cortex brain slices.,” *J. Neurosci.*, vol. 7, no. 4, pp. 1223–1249, 1987.

[11] S. R. Olsen, D. S. Bortone, H. Adesnik, and M. Scanziani, “Gain control by layer six in cortical circuits of vision,” *Nature*, vol. 483, no. 7387, pp. 47–52, Feb. 2012.

[12] R. R. Johnson and A. Burkhalter, “Microcircuitry of forward and feedback connections within rat visual cortex,” *J. Comp. Neurol.*, vol. 368, no. 3, pp. 383–398, 1996.

[13] S. Sakata and K. D. Harris, “Laminar Structure of Spontaneous and Sensory-Evoked Population Activity in Auditory Cortex,” *Neuron*, vol. 64, no. 3, pp. 404–418, 2009.

[14] A. Maier, G. K. Adams, C. Aura, and D. A. Leopold, “Distinct superficial and deep laminar domains of activity in the visual cortex during rest and stimulation.,” *Front. Syst. Neurosci.*, vol. 4, 2010.

[15] M. Tsodyks, T. Kenet, a Grinvald, and a Arieli, “Linking spontaneous activity of single cortical neurons and the underlying functional architecture.,” *Science*, vol. 286, no. 5446, pp. 1943–1946, 1999.

[16] C. D. Gilbert, “Microcircuitry of the Visual Cortex,” *Annu. Rev. Neurosci.*, vol. 6, no. 1, pp. 217–247, Mar. 1983.

[17] B. Y. D. H. Hubel and a D. T. N. Wiesel, “Receptive feilds, binocular interaction and functional architecture in the cat’s visual cortex,” *J. physiol.*, vol. 160, pp. 106–154, 1962.

[18] K. Cheng, R. a Waggoner, and K. Tanaka, “Human ocular dominance columns as revealed by high-field functional magnetic resonance imaging.,” *Neuron*, vol. 32, no. 2, pp. 359–374, 2001.

[19] E. Yacoub, N. Harel, and K. Ugurbil, “High-field fMRI unveils orientation columns in humans.,” *Proc. Natl. Acad. Sci. U. S. A.*, vol. 105, no. 30, pp. 10607–12, 2008.

[20] K. Uğurbil, G. Adriany, P. Andersen, W. Chen, M. Garwood, R. Gruetter, P.-G. Henry, S.-G. Kim, H. Lieu, I. Tkac, T. Vaughan, P.-F. Van De Moortele, E. Yacoub, and X.-H. Zhu, “Ultrahigh field magnetic resonance imaging and spectroscopy,” *Magn. Reson. Imaging*, vol. 21, no. 10, pp. 1263–1281, 2003.

[21] E. Yacoub, N. Harel, and K. Ugurbil, “High-field fMRI unveils orientation columns in humans.,” *Proc. Natl. Acad. Sci. U. S. A.*, vol. 105, no. 30, pp. 10607–12, Jul. 2008.

[22] P. J. Koopmans, S. Orzada, M. Barth, and D. G. Norris, “Distinguishing pial and laminar gradient-echo BOLD signals at 7 Tesla,” *Proc. Int. Soc. Magn. Reson. Med.*, vol. 2009, p. 4064, 2009.

[23] E. Yacoub, K. Ugurbil, and C. Olman, “Feasibility of detecting differential layer specific activations in humans using SE BOLD fMRI at 7 T,” *Proc. 17th Sci. Meet. Int. Soc. Magn. Reson. Med.*, vol. Honolulu, p. 1607, 2009.

[24] J. R. Polimeni, B. Fischl, D. N. Greve, and L. L. Wald, “Laminar analysis of 7T BOLD using an imposed spatial activation pattern in human V1,” *Neuroimage*, vol. 52, no. 4, pp.

1334–1346, 2010.

[25] C. A. Olman, N. Harel, D. A. Feinberg, S. He, P. Zhang, K. Ugurbil, and E. Yacoub, “Layer-specific fmri reflects different neuronal computations at different depths in human V1,” *PLoS One*, vol. 7, no. 3, p. e32536, Mar. 2012.

[26] P. Kok, L. J. Bains, T. Van Mourik, D. G. Norris, and F. P. De Lange, “Selective activation of the deep layers of the human primary visual cortex by top-down feedback,” *Curr. Biol.*, vol. 26, no. 3, pp. 371–376, Feb. 2016.

[27] L. Muckli, F. De Martino, L. Vizioli, L. S. Petro, F. W. Smith, K. Ugurbil, R. Goebel, and E. Yacoub, “Contextual Feedback to Superficial Layers of V1,” *Curr. Biol.*, vol. 25, no. 20, pp. 2690–2695, 2015.

[28] A. Klein and J. Tourville, “101 Labeled Brain Images and a Consistent Human Cortical Labeling Protocol,” *Front. Neurosci.*, vol. 6, p. 171, 2012.

[29] R. S. Desikan, F. Ségonne, and B. Fischl, “An automated labeling system for subdividing the human cerebral cortex on MRI scans into gyral based regions of interest,” *Neuroimage*, vol. 31, no. 3, pp. 968–80, 2006.

[30] B. Fischl, A. Van Der Kouwe, C. Destrieux, E. Halgren, F. Ségonne, D. H. Salat, E. Busa, L. J. Seidman, J. Goldstein, D. Kennedy, V. Caviness, N. Makris, B. Rosen, and A. M. Dale, “Automatically Parcellating the Human Cerebral Cortex,” *Cereb. Cortex*, vol. 14, no. 1, pp. 11–22, 2004.

[31] C. Destrieux, B. Fischl, A. Dale, and E. Halgren, “Automatic parcellation of human cortical gyri and sulci using standard anatomical nomenclature,” *Neuroimage*, vol. 53, no. 1, pp. 1–

15, 2010.

[32] R. Turner and S. Geyer, “Comparing like with like: the power of knowing where you are.,” *Brain Connect.*, vol. 4, no. 7, pp. 547–57, 2014.

[33] P. J. Koopmans, M. Barth, and D. G. Norris, “Layer-specific BOLD activation in human V1.,” *Hum. Brain Mapp.*, vol. 31, no. 9, pp. 1297–304, Sep. 2010.

[34] L. Muckli, F. De Martino, L. Vizioli, L. S. Petro, F. W. Smith, K. Ugurbil, R. Goebel, and E. Yacoub, “Contextual Feedback to Superficial Layers of V1,” *Curr. Biol.*, vol. 25, no. 20, pp. 2690–2695, 2015.

[35] P. Bandettini, “The BOLD plot thickens: sign-and layer-dependent hemodynamic changes with activation,” *Neuron*, vol. 76, no. 3, pp. 468–469, 2012.

[36] G. Chen, F. Wang, J. C. Gore, and A. W. Roe, “Layer-specific BOLD activation in awake monkey V1 revealed by ultra-high spatial resolution functional magnetic resonance imaging,” *Neuroimage*, vol. 64, no. 1, pp. 147–155, 2013.

[37] M. Jenkinson, C. F. Beckmann, T. E. J. Behrens, M. W. Woolrich, and S. M. Smith, “FSL,” *NeuroImage*, vol. 62, no. 2. pp. 782–790, 15-Aug-2012.

[38] R. Sladky, K. J. Friston, J. Tröstl, R. Cunnington, E. Moser, and C. Windischberger, “Slice-timing effects and their correction in functional MRI.,” *Neuroimage*, vol. 58, no. 2, pp. 588–94, Sep. 2011.

[39] R. Henson, C. Buechel, O. Josephs, and K. Friston, “The slice-timing problem in event-related fMRI,” *Neuroimage*, 1999.

[40] M. F. Glasser, S. N. Sotiropoulos, J. A. Wilson, T. S. Coalson, B. Fischl, J. L. Andersson,

J. Xu, S. Jbabdi, M. Webster, J. R. Polimeni, D. C. Van Essen, and M. Jenkinson, “The minimal preprocessing pipelines for the Human Connectome Project,” *Neuroimage*, vol. 80, pp. 105–124, 2013.

[41] J. Ashburner and K. Friston, “Rigid Body Registration,” in *Human Brain Function: Second Edition*, 2003, pp. 635–653.

[42] M. Jenkinson and S. Smith, “A global optimisation method for robust affine registration of brain images,” *Med. Image Anal.*, vol. 5, no. 2, pp. 143–156, 2001.

[43] B. Fischl, “FreeSurfer,” *NeuroImage*, vol. 62, no. 2. pp. 774–781, 15-Aug-2012.

[44] A. M. Dale, B. Fischl, and M. I. Sereno, “Cortical Surface-Based Analysis: I. Segmentation and Surface Reconstruction,” *Neuroimage*, vol. 9, no. 2, pp. 179–194, 1999.

[45] B. Fischl, “FreeSurfer,” *NeuroImage*, vol. 62, no. 2. pp. 774–781, 2012.

[46] B. Fischl, D. H. Salat, E. Busa, M. Albert, M. Dieterich, C. Haselgrove, A. Van Der Kouwe, R. Killiany, D. Kennedy, S. Klaveness, A. Montillo, N. Makris, B. Rosen, and A. M. Dale, “Neurotechnique Whole Brain Segmentation: Automated Labeling of Neuroanatomical Structures in the Human Brain,” *Neuron*, vol. 33, pp. 341–355, 2002.

[47] F. Lüsebrink, A. Wollrab, and O. Speck, “Cortical thickness determination of the human brain using high resolution 3T and 7T MRI data,” *Neuroimage*, vol. 70, pp. 122–131, 2013.

[48] M. I. Sereno, A. Lutti, N. Weiskopf, and F. Dick, “Mapping the human cortical surface by combining quantitative T1 with retinotopy,” *Cereb. Cortex*, vol. 23, no. 9, pp. 2261–2268, 2013.

[49] R. Trampel, P.-L. Bazin, A. Schäfer, R. M. Heidemann, D. Ivanov, G. Lohmann, S. Geyer,

and R. Turner, “Laminar-specific fingerprints of different sensorimotor areas obtained during imagined and actual finger tapping,” *Proc Intl Soc Mag Reson Med*, vol. 20, p. 663, 2012.

[50] D. N. Greve and B. Fischl, “Accurate and robust brain image alignment using boundary-based registration.,” *Neuroimage*, vol. 48, no. 1, pp. 63–72, 2009.

[51] D. A. Handwerker, J. M. Ollinger, and M. D’Esposito, “Variation of BOLD hemodynamic responses across subjects and brain regions and their effects on statistical analyses,” *Neuroimage*, vol. 21, no. 4, pp. 1639–1651, 2004.

[52] O. David, I. Guillemain, S. Saillet, S. Reyt, C. Deransart, C. Segebarth, and A. Depaulis, “Identifying neural drivers with functional MRI: an electrophysiological validation.,” *PLoS Biol.*, vol. 6, no. 12, pp. 2683–2697, 2008.

[53] G. Deshpande, K. Sathian, and X. Hu, “Assessing and compensating for zero-lag correlation effects in time-lagged granger causality analysis of fMRI,” *IEEE Trans. Biomed. Eng.*, vol. 57, no. 6, pp. 1446–1456, 2010.

[54] G.-R. Wu, W. Liao, S. Stramaglia, J.-R. Ding, H. Chen, and D. Marinazzo, “A blind deconvolution approach to recover effective connectivity brain networks from resting state fMRI data.,” *Med. Image Anal.*, vol. 17, no. 3, pp. 365–74, 2013.

[55] M. Havlicek, J. Jan, M. Brazdil, and V. D. Calhoun, “Dynamic Granger causality based on Kalman filter for evaluation of functional network connectivity in fMRI data,” *Neuroimage*, vol. 53, no. 1, pp. 65–77, 2010.

[56] K. R. Sreenivasan, M. Havlicek, and G. Deshpande, “Nonparametric hemodynamic

deconvolution of fMRI using homomorphic filtering," *IEEE Trans. Med. Imaging*, vol. 34, no. 5, pp. 1155–1163, 2015.

[57] K. J. Friston, "Functional and effective connectivity: a review.," *Brain Connect.*, vol. 1, no. 1, pp. 13–36, 2011.

[58] G. L. Gerstein and D. H. Perkel, "Simultaneously recorded trains of action potentials: analysis and functional interpretation.," *Science*, vol. 164, no. 3881, pp. 828–30, May 1969.

[59] J. Heinzle, P. J. Koopmans, H. E. M. M. den Ouden, S. Raman, and K. E. Stephan, "A hemodynamic model for layered BOLD signals," *Neuroimage*, vol. 125, pp. 556–570, 2016.

[60] P. J. Koopmans, M. Barth, S. Orzada, and D. G. Norris, "Multi-echo fMRI of the cortical laminae in humans at 7 T.," *Neuroimage*, vol. 56, no. 3, pp. 1276–85, Jun. 2011.

[61] J. R. Polimeni, B. Fischl, D. N. Greve, and L. L. Wald, "Laminar-specific output- to input-layer connections between cortical areas V1 and MT observed with high-resolution resting-state fMRI," in *Proceedings of the International Society for Magnetic Resonance in Medicine*, 2010, vol. 18, p. 3471.

[62] R. Turner and S. Geyer, "Comparing like with like: the power of knowing where you are.," *Brain Connect.*, vol. 4, no. 7, pp. 547–57, Sep. 2014.

[63] B. Biswal, F. Z. Yetkin, V. M. Haughton, and J. S. Hyde, "Functional connectivity in the motor cortex of resting human brain using echo-planar MRI.," *Magn. Reson. Med.*, vol. 34, no. 4, pp. 537–541, 1995.

[64] M. Lehmann, C. Madison, P. M. Ghosh, Z. A. Miller, M. D. Greicius, J. H. Kramer, G. Coppola, B. L. Miller, W. J. Jagust, M. L. Gorno-Tempini, W. W. Seeley, and G. D.

Rabinovici, “Loss of functional connectivity is greater outside the default mode network in nonfamilial early-onset Alzheimer’s disease variants,” *Neurobiol. Aging*, vol. 36, no. 10, pp. 2678–2686, 2015.

[65] M. A. Fernández-Seara, E. Mengual, M. Vidorreta, G. Castellanos, J. Irigoyen, E. Erro, and M. A. Pastor, “Resting state functional connectivity of the subthalamic nucleus in Parkinson’s disease assessed using arterial spin-labeled perfusion fMRI,” *Hum. Brain Mapp.*, vol. 36, no. 5, pp. 1937–1950, May 2015.

[66] Q. Yu, E. A. Allen, J. Sui, M. R. Arbabshirani, G. Pearlson, and V. D. Calhoun, “Brain connectivity networks in schizophrenia underlying resting state functional magnetic resonance imaging.,” *Curr. Top. Med. Chem.*, vol. 12, no. 21, pp. 2415–25, 2012.

[67] K. Wang, M. Liang, L. Wang, L. Tian, X. Zhang, K. Li, and T. Jiang, “Altered functional connectivity in early Alzheimer’s disease: a resting-state fMRI study.,” *Hum. Brain Mapp.*, vol. 28, no. 10, pp. 967–78, Oct. 2007.

[68] M. R. Brier, J. B. Thomas, A. M. Fagan, J. Hassenstab, D. M. Holtzman, T. L. Benzinger, J. C. Morris, and B. M. Ances, “Functional connectivity and graph theory in preclinical Alzheimer’s disease,” *Neurobiol. Aging*, vol. 35, no. 4, pp. 757–768, 2014.

[69] M. Plitt, K. A. Barnes, G. L. Wallace, L. Kenworthy, and A. Martin, “Resting-state functional connectivity predicts longitudinal change in autistic traits and adaptive functioning in autism.,” *Proc. Natl. Acad. Sci. U. S. A.*, vol. 112, no. 48, pp. E6699-706, Dec. 2015.

[70] H. Jia, X. Hu, and G. Deshpande, “Behavioral relevance of the dynamics of the functional brain connectome.,” *Brain Connect.*, vol. 4, no. 9, pp. 741–59, Nov. 2014.

[71] X. J. Dubois, “Brain Age : A State-Of-Mind ? On the Stability of Functional Connectivity across Behavioral States,” *J. Neurosci.*, vol. 36, no. 8, pp. 2325–2328, Feb. 2016.

[72] M. S. Koyama, A. Di Martino, X.-N. Zuo, C. Kelly, M. Mennes, D. R. Jutagir, F. X. Castellanos, and M. P. Milham, “Resting-state functional connectivity indexes reading competence in children and adults.,” *J. Neurosci.*, vol. 31, no. 23, pp. 8617–24, Jun. 2011.

[73] Y. Adachi, T. Osada, O. Sporns, T. Watanabe, T. Matsui, K. Miyamoto, and Y. Miyashita, “Functional connectivity between anatomically unconnected areas is shaped by collective network-level effects in the macaque cortex,” *Cereb. Cortex*, vol. 22, no. 7, pp. 1586–1592, 2012.

[74] M. P. van den Heuvel, L. H. Scholtens, E. Turk, D. Mantini, W. Vanduffel, and L. Feldman Barrett, “Multimodal analysis of cortical chemoarchitecture and macroscale fMRI resting-state functional connectivity,” *Hum. Brain Mapp.*, vol. 37, no. 9, pp. 3103–3113, Sep. 2016.

[75] C. J. Honey, O. Sporns, L. Cammoun, X. Gigandet, J. P. Thiran, R. Meuli, and P. Hagmann, “Predicting human resting-state functional connectivity from structural connectivity,” *Proc. Natl. Acad. Sci.*, vol. 106, no. 6, pp. 2035–2040, Feb. 2009.

[76] E. Turk, L. H. Scholtens, and M. P. van den Heuvel, “Cortical chemoarchitecture shapes macroscale effective functional connectivity patterns in macaque cerebral cortex,” *Hum. Brain Mapp.*, vol. 37, no. 5, pp. 1856–1865, 2016.

[77] K. Shen, R. M. Hutchison, G. Bezgin, S. Everling, and A. R. McIntosh, “Network structure shapes spontaneous functional connectivity dynamics.,” *J. Neurosci.*, vol. 35, no. 14, pp. 5579–88, 2015.

[78] M. Senden, R. Goebel, and G. Deco, “Structural connectivity allows for multi-threading during rest: the structure of the cortex leads to efficient alternation between resting state exploratory behavior and default mode processing.,” *Neuroimage*, vol. 60, no. 4, pp. 2274–84, May 2012.

[79] J. M. Segall, E. A. Allen, R. E. Jung, E. B. Erhardt, S. K. Arja, K. Kiehl, and V. D. Calhoun, “Correspondence between structure and function in the human brain at rest.,” *Front. Neuroinform.*, vol. 6, p. 10, 2012.

[80] S. Rane, S. Kose, J. C. Gore, and S. Heckers, “Altered Functional and Structural Connectivity in a Schizophrenia Patient With Complete Agenesis of the Corpus Callosum,” *Am. J. Psychiatry*, vol. 170, no. 1, pp. 122–123, Jan. 2013.

[81] J. R. Polimeni, M. Mianciardi, B. Keil, and L. L. Wald, “Cortical depth dependence of physiological fluctuations and whole-brain resting-state functional connectivity at 7T,” *Proc. Int. Soc. Magn. Reson. Med.*, vol. 23, no. 2010, p. 592, 2015.

[82] A. Vasireddi, A. Vazquez, D. Whitney, M. Fukuda, and S.-G. Kim, “Functional Connectivity of Resting Hemodynamic Signals in Submillimeter Orientation Columns of the Visual Cortex,” *Brain Connect.*, p. brain.2015.0414, Jul. 2016.

[83] J. C. W. Siero, N. Petridou, H. Hoogduin, P. R. Luijten, and N. F. Ramsey, “Cortical depth-dependent temporal dynamics of the BOLD response in the human brain,” *J. Cereb. Blood Flow Metab.*, vol. 31, no. 10, pp. 1999–2008, Oct. 2011.

[84] X. Yu, C. Qian, D. Chen, S. J. Dodd, and A. P. Koretsky, “Deciphering laminar-specific neural inputs with line-scanning fMRI.,” *Nat. Methods*, vol. 11, no. 1, pp. 55–8, Nov. 2014.

[85] J. C. W. Siero, N. F. Ramsey, H. Hoogduin, D. W. J. Klomp, P. R. Luijten, and N. Petridou, “BOLD Specificity and Dynamics Evaluated in Humans at 7 T: Comparing Gradient-Echo and Spin-Echo Hemodynamic Responses,” *PLoS One*, vol. 8, no. 1, p. e54560, 2013.

[86] P. Tian, I. C. Teng, L. D. May, R. Kurz, K. Lu, M. Scadeng, E. M. C. Hillman, A. J. De Crespigny, H. E. D’Arceuil, J. B. Mandeville, J. J. A. Marota, B. R. Rosen, T. T. Liu, D. A. Boas, R. B. Buxton, A. M. Dale, and A. Devor, “Cortical depth-specific microvascular dilation underlies laminar differences in blood oxygenation level-dependent functional MRI signal,” *Proc. Natl. Acad. Sci.*, vol. 107, no. 34, pp. 15246–15251, 2010.

[87] T. Jin and S.-G. Kim, “Cortical layer-dependent dynamic blood oxygenation, cerebral blood flow and cerebral blood volume responses during visual stimulation.,” *Neuroimage*, vol. 43, no. 1, pp. 1–9, 2008.

[88] R. M. S. Panchuelo, D. Schluppeck, J. Harmer, R. Bowtell, and S. Francis, “Assessing the Spatial Precision of SE and GE-BOLD Contrast at 7 Tesla,” *Brain Topogr.*, vol. 28, no. 1, pp. 62–65, 2014.

[89] I. Markuerkiaga, M. Barth, and D. G. Norris, “A cortical vascular model for examining the specificity of the laminar BOLD signal.,” *Neuroimage*, vol. 132, pp. 491–498, 2016.

[90] J. E. Chen and G. H. Glover, “BOLD fractional contribution to resting-state functional connectivity above 0.1 Hz.,” *Neuroimage*, vol. 107, pp. 207–18, Feb. 2015.

[91] G. Deshpande, K. Sathian, and X. Hu, “Effect of hemodynamic variability on Granger causality analysis of fMRI,” *Neuroimage*, vol. 52, no. 3, pp. 884–896, 2010.

[92] D. Rangaprakash, G. Wu, D. Marinazzo, X. Hu, and G. Deshpande, “Impact of Undesirable

Hemodynamic Variability on fMRI Functional Connectivity," *IEEE Trans. Biomed. Eng.*, p. In press, 2016.

[93] G.-R. Wu, W. Liao, S. Stramaglia, J.-R. Ding, H. Chen, and D. Marinazzo, "A blind deconvolution approach to recover effective connectivity brain networks from resting state fMRI data.," *Med. Image Anal.*, vol. 17, no. 3, pp. 365–74, 2013.

[94] P. Rubio-Garrido, F. Pérez-De-Manzo, C. Porrero, M. J. Galazo, and F. Clascá, "Thalamic input to distal apical dendrites in neocortical layer 1 is massive and highly convergent," *Cereb. Cortex*, vol. 19, no. 10, pp. 2380–2395, 2009.

[95] S. Cruikshank, O. Ahmed, and T. Stevens, "Thalamic control of layer 1 circuits in prefrontal cortex," *J. Neurosci.*, vol. 32, no. 49, pp. 17813–23, 2012.

[96] E. Kuramoto, S. Ohno, T. Furuta, T. Unzai, Y. R. Tanaka, H. Hioki, and T. Kaneko, "Ventral medial nucleus neurons send thalamocortical afferents more widely and more preferentially to layer 1 than neurons of the ventral anterior-ventral lateral nuclear complex in the rat," *Cereb. Cortex*, vol. 25, no. 1, pp. 221–235, 2015.

[97] A. J. Lee, G. Wang, X. Jiang, S. M. Johnson, E. T. Hoang, F. Lanté, R. L. Stornetta, M. P. Beenhakker, Y. Shen, and J. Julius Zhu, "Canonical Organization of Layer 1 Neuron-Led Cortical Inhibitory and Disinhibitory Interneuronal Circuits.," *Cereb. cortex*, vol. 25, no. 8, pp. 2114–26, 2015.

[98] M. Garcia-Munoz and G. W. Arbuthnott, "Basal ganglia—thalamus and the 'crowning enigma,'" *Front. Neural Circuits*, vol. 9, p. 71, 2015.

[99] M. M. Roth, J. C. Dahmen, D. R. Muir, F. Imhof, F. J. Martini, and S. B. Hofer, "Thalamic

nuclei convey diverse contextual information to layer 1 of visual cortex," *Nat. Neurosci.*, vol. 19, no. 148.26, p. 148, 2015.

[100] B. B. Theyel, C. C. Lee, and S. M. Sherman, "Specific and nonspecific thalamocortical connectivity in the auditory and somatosensory thalamocortical slices.," *Neuroreport*, vol. 21, no. 13, pp. 861–4, Sep. 2010.

[101] S. J. Cruikshank, O. J. Ahmed, T. R. Stevens, S. L. Patrick, A. N. Gonzalez, M. Elmaleh, and B. W. Connors, "Thalamic control of layer 1 circuits in prefrontal cortex.," *J. Neurosci.*, vol. 32, no. 49, pp. 17813–23, 2012.

[102] F. Aboitiz and J. Montiel, "One hundred million years of interhemispheric communication: The history of the corpus callosum," *Brazilian Journal of Medical and Biological Research*, vol. 36, no. 4. pp. 409–420, 2003.

[103] F. Scicchitano, C. M. van Rijn, and G. van Luijtelaar, "Unilateral and Bilateral Cortical Resection: Effects on Spike-Wave Discharges in a Genetic Absence Epilepsy Model.," *PLoS One*, vol. 10, no. 8, p. e0133594, 2015.

[104] D. C. Van Essen, W. T. Newsome, and J. L. Bixby4, "The pattern of interhemispheric connections and its relationship to extrastriate visual areas in the macaque monkey.," *J. Neurosci ence*, vol. 2, no. 3, pp. 265–283, 1982.

[105] D. J. Felleman and D. C. Van Essen, "Distributed hierarchical processing in the primate cerebral cortex.," *Cereb. Cortex*, vol. 1, no. 1, pp. 1–47, 1991.

[106] D. Feldmeyer, J. Lübke, R. A. Silver, and B. Sakmann, "Synaptic connections between layer 4 spiny neurone-layer 2/3 pyramidal cell pairs in juvenile rat barrel cortex: physiology and

anatomy of interlaminar signalling within a cortical column.," *J. Physiol.*, vol. 538, no. Pt 3, pp. 803–22, Feb. 2002.

[107] F. Lusebrink, A. Wollrab, and O. Speck, "Cortical thickness determination of the human brain using high resolution 3T and 7T MRI data," *Neuroimage*, vol. 70C, pp. 122–131, 2012.

[108] E. Tagliazucchi, P. Balenzuela, D. Fraiman, and D. R. Chialvo, "Criticality in large-scale brain fmri dynamics unveiled by a novel point process analysis," *Front. Physiol.*, 2012.

[109] A. T. Lee, G. H. Glover, and C. H. Meyer, "Discrimination of large venous vessels in time-course spiral blood- oxygen-level-dependent magnetic-resonance functional neuroimaging," *Magn. Reson. Med.*, vol. 33, no. 6, pp. 745–754, 1995.

[110] S. E. Jones, B. R. Buchbinder, and I. Aharon, "Three-dimensional mapping of cortical thickness using Laplace's equation," *Hum. Brain Mapp.*, vol. 11, no. 1, pp. 12–32, 2000.

[111] M. D. Waehnert, J. Dinse, M. Weiss, M. N. Streicher, P. Waehnert, S. Geyer, R. Turner, and P. L. Bazin, "Anatomically motivated modeling of cortical laminae," *Neuroimage*, vol. 93, pp. 210–220, 2014.

[112] H. Barbas, M. Á. García-Cabezas, and B. Zikopoulos, "Frontal-thalamic circuits associated with language.," *Brain and language*, vol. 126, no. 1. pp. 49–61, 2013.

[113] K. J. Friston, L. Harrison, and W. Penny, "Dynamic causal modelling," *Neuroimage*, vol. 19, no. 4, pp. 1273–1302, 2003.

[114] Y. Wang, S. Katwal, B. Rogers, J. Gore, and G. Deshpande, "Experimental Validation of Dynamic Granger Causality for Inferring Stimulus-evoked Sub-100ms Timing Differences from fMRI.," *IEEE Trans. Neural Syst. Rehabil. Eng.*, Jul. 2016.

[115] G. Deshpande and X. Hu, “Investigating effective brain connectivity from fMRI data: past findings and current issues with reference to Granger causality analysis,” *Brain Connect.*, vol. 2, no. 5 PG-235-245, pp. 235–245, 2012.

[116] G. Deshpande, P. Santhanam, and X. Hu, “Instantaneous and causal connectivity in resting state brain networks derived from functional MRI data.,” *Neuroimage*, vol. 54, no. 2, pp. 1043–52, Jan. 2011.

[117] G. Deshpande, S. LaConte, G. A. James, S. Peltier, and X. Hu, “Multivariate granger causality analysis of fMRI data,” *Hum. Brain Mapp.*, vol. 30, no. 4, pp. 1361–1373, Apr. 2009.

[118] F. Briggs and W. M. Usrey, “Emerging views of corticothalamic function,” *Current Opinion in Neurobiology*, vol. 18, no. 4. NIH Public Access, pp. 403–407, Aug-2008.

[119] F. Briggs and W. M. Usrey, “Parallel Processing in the Corticogeniculate Pathway of the Macaque Monkey,” *Neuron*, vol. 62, no. 1, pp. 135–146, Apr. 2009.

[120] F. Briggs and W. M. Usrey, “Corticogeniculate feedback and visual processing in the primate.,” *J. Physiol.*, vol. 589, no. Pt 1, pp. 33–40, Jan. 2011.

[121] A. E. Hendrickson, J. R. Wilson, and M. P. Ogren, “The neuroanatomical organization of pathways between the dorsal lateral geniculate nucleus and visual cortex in Old World and New World primates,” *J Comp Neurol*, vol. 182, no. 1, pp. 123–136, 1978.

[122] J. M. Ichida and V. A. Casagrande, “Organization of the feedback pathway from striate cortex (V1) to the lateral geniculate nucleus (LGN) in the owl monkey (aotus trivirgatus),” *J. Comp. Neurol.*, vol. 454, no. 3, pp. 272–283, 2002.

[123] J. S. Lund, R. D. Lund, a E. Hendrickson, a H. Bunt, and a F. Fuchs, “The origin of efferent pathways from the primary visual cortex, area 17, of the macaque monkey as shown by retrograde transport of horseradish peroxidase.,” *J. Comp. Neurol.*, vol. 164, no. 3, pp. 287–303, 1975.

[124] M. Conley and D. Raczkowski, “Sublaminar organization within layer VI of the striate cortex in Galago,” *J. Comp. Neurol.*, vol. 302, no. 2, pp. 425–436, 1990.

[125] W. H. Merigan, L. M. Katz, and J. H. Maunsell, “The effects of parvocellular lateral geniculate lesions on the acuity and contrast sensitivity of macaque monkeys.,” *J. Neurosci.*, vol. 11, no. 4, pp. 994–1001, 1991.

[126] M. Livingstone and D. Hubel, “Segregation of Depth: Form, Anatomy, Color, Physiology, and Movement, and Perception,” *Sci. New Ser.*, vol. 240, no. 4853, pp. 740–749, 1988.

[127] A. M. Derrington and P. Lennie, “Spatial and temporal contrast sensitivities of neurones in lateral geniculate nucleus of macaque.,” *J. Physiol.*, vol. 357, pp. 219–240, 1984.

[128] P. H. Schiller and N. K. Logothetis, “The color-opponent and broad-band channels of the primate visual system,” *Trends Neurosci.*, vol. 13, no. 10, pp. 392–398, 1990.

[129] J. J. Nassi and E. M. Callaway, “Parallel processing strategies of the primate visual system.,” *Nat. Rev. Neurosci.*, vol. 10, no. 5, pp. 360–372, 2009.

[130] W. H. Merigan and J. H. Maunsell, “How parallel are the primate visual pathways?,” *Annu. Rev. Neurosci.*, vol. 16, no. 1, pp. 369–402, Mar. 1993.

[131] K. L. Grieve and A. M. Sillito, “Differential properties of cells in the feline primary visual cortex providing the corticofugal feedback to the lateral geniculate nucleus and visual

claustrum.," *J. Neurosci.*, vol. 15, no. 7 Pt 1, pp. 4868–74, 1995.

[132] H. E. Jones, I. M. Andolina, K. L. Grieve, W. Wang, T. E. Salt, J. Cudeiro, and A. M. Sillito, "Responses of primate LGN cells to moving stimuli involve a constant background modulation by feedback from area MT," *Neuroscience*, vol. 246, pp. 254–264, Aug. 2013.

[133] P. C. Murphy and a M. Sillito, "Corticofugal feedback influences the generation of length tuning in the visual pathway.," *Nature*, vol. 329, no. 6141, pp. 727–729, Oct. 1987.

[134] A. M. Sillito and H. E. Jones, "Corticothalamic interactions in the transfer of visual information.," *Philos. Trans. R. Soc. Lond. B. Biol. Sci.*, vol. 357, no. 1428, pp. 1739–52, Dec. 2002.

[135] B. A. Wandell, J. Winawer, and K. N. Kay, "Computational Modeling of Responses in Human Visual Cortex," in *Brain Mapping*, Elsevier, 2015, pp. 651–659.

[136] A. M. Sillito, J. Cudeiro, and H. E. Jones, "Always returning: feedback and sensory processing in visual cortex and thalamus," *Trends in Neurosciences*, vol. 29, no. 6. pp. 307–316, Jun-2006.

[137] A. Angelucci and K. Sainsbury, "Contribution of feedforward thalamic afferents and corticogeniculate feedback to the spatial summation area of macaque V1 and LGN," *J. Comp. Neurol.*, vol. 498, no. 3, pp. 330–351, 2006.

[138] I. M. Andolina, H. E. Jones, W. Wang, and a. M. Sillito, "Corticothalamic feedback enhances stimulus response precision in the visual system.," *Pnas*, vol. 104, no. 5, pp. 1685–1690, 2007.

[139] F. Briggs, C. W. Kiley, E. M. Callaway, and W. M. Usrey, "Morphological Substrates for

Parallel Streams of Corticogeniculate Feedback Originating in Both V1 and V2 of the Macaque Monkey," *Neuron*, vol. 90, no. 2, pp. 388–399, 2016.

[140] F. Briggs and W. M. Usrey, "A fast, reciprocal pathway between the lateral geniculate nucleus and visual cortex in the macaque monkey.," *J. Neurosci.*, vol. 27, no. 20, pp. 5431–6, May 2007.

[141] S. R. Olsen, D. S. Bortone, H. Adesnik, and M. Scanziani, "Gain control by layer six in cortical circuits of vision," *Nature*, vol. 483, no. 7387, pp. 47–52, 2012.

[142] R. F. Hevner, "Development of connections in the human visual system during fetal mid-gestation: a DiI-tracing study.," *J. Neuropathol. Exp. Neurol.*, vol. 59, no. 5, pp. 385–92, 2000.

[143] L. Krubitzer, "The magnificent compromise: cortical field evolution in mammals.," *Neuron*, vol. 56, no. 2, pp. 201–8, Oct. 2007.

[144] C. F. Stevens, "An evolutionary scaling law for the primate visual system and its basis in cortical function," *Nature*, vol. 411, no. 6834, pp. 193–195, May 2001.

[145] J. G. Daugman, "Two-dimensional spectral analysis of cortical receptive field profiles," *Vision Res.*, vol. 20, no. 10, pp. 847–856, 1980.

[146] D. Gabor, "Theory of communication," *J. Institute of Electr. Eng.*, vol. 93. pp. 429–457, 1946.

[147] J. P. Jones and L. A. Palmer, "An evaluation of the two-dimensional Gabor filter model of simple receptive fields in cat striate cortex.," *J. Neurophysiol.*, vol. 58, no. 6, pp. 1233–1258, 1987.

[148] J. P. Jones and L. A. Palmer, “The two-dimensional spatial structure of simple receptive fields in cat striate cortex.,” *J. Neurophysiol.*, vol. 58, no. 6, pp. 1187–211, 1987.

[149] R. E. Fredericksen, P. J. Bex, and F. a Verstraten, “How big is a Gabor patch, and why should we care?,” *J. Opt. Soc. Am. A. Opt. Image Sci. Vis.*, vol. 14, no. 1, pp. 1–12, 1997.

[150] H. J. Alitto, B. D. Moore, D. L. Rathbun, and W. M. Usrey, “A comparison of visual responses in the lateral geniculate nucleus of alert and anaesthetized macaque monkeys.,” *J. Physiol.*, vol. 589, no. Pt 1, pp. 87–99, 2011.

[151] H. J. Alitto and W. M. Usrey, “Origin and Dynamics of Extraclassical Suppression in the Lateral Geniculate Nucleus of the Macaque Monkey,” *Neuron*, vol. 57, no. 1, pp. 135–146, 2008.

[152] R. N. Denison, A. T. Vu, E. Yacoub, D. A. Feinberg, and M. A. Silver, “Functional mapping of the magnocellular and parvocellular subdivisions of human LGN,” *Neuroimage*, vol. 102, no. P2, pp. 358–369, Nov. 2014.

[153] E. Kaplan and E. Benardete, “The dynamics of primate retinal ganglion cells,” in *Progress in Brain Research*, 2001, vol. 134, pp. 17–34.

[154] J. a Mazer, W. E. Vinje, J. McDermott, P. H. Schiller, and J. L. Gallant, “Spatial frequency and orientation tuning dynamics in area V1.,” *Proc. Natl. Acad. Sci. U. S. A.*, vol. 99, no. 3, pp. 1645–1650, 2002.

[155] M. P. Sceniak, M. J. Hawken, and R. Shapley, “Contrast-dependent changes in spatial frequency tuning of macaque V1 neurons: effects of a changing receptive field size.,” *J. Neurophysiol.*, vol. 88, no. 3, pp. 1363–1373, 2002.

[156] A. M. Sillito, J. Cudeiro, and P. C. Murphy, “Orientation sensitive elements in the corticofugal influence on centre-surround interactions in the dorsal lateral geniculate nucleus,” *Exp. Brain Res.*, vol. 93, no. 1, pp. 6–16, 1993.

[157] W. Wang, H. E. Jones, I. M. Andolina, T. E. Salt, and A. M. Sillito, “Functional alignment of feedback effects from visual cortex to thalamus,” *Nat. Neurosci.*, vol. 9, no. 10, pp. 1330–1336, Oct. 2006.

[158] D. A. Feinberg, S. Moeller, S. M. Smith, E. Auerbach, S. Ramanna, M. F. Glasser, K. L. Miller, K. Ugurbil, and E. Yacoub, “Multiplexed echo planar imaging for sub-second whole brain fmri and fast diffusion imaging,” *PLoS One*, vol. 5, no. 12, 2010.

[159] E. Yacoub, N. Harel, and K. Ugurbil, “High-field fMRI unveils orientation columns in humans.,” *Proc. Natl. Acad. Sci. U. S. A.*, vol. 105, no. 30, pp. 10607–12, 2008.

[160] G. Bellucci, S. Chernyak, M. Hoffman, G. Deshpande, O. Dal Monte, K. M. Knutson, J. Grafman, and F. Krueger, “Effective connectivity of brain regions underlying third-party punishment: Functional MRI and Granger causality evidence.,” *Soc. Neurosci.*, pp. 1–11, Mar. 2016.

[161] B. M. Hampstead, M. Khoshnoodi, W. Yan, G. Deshpande, and K. Sathian, “Patterns of effective connectivity during memory encoding and retrieval differ between patients with mild cognitive impairment and healthy older adults,” *Neuroimage*, vol. 124, pp. 997–1008, 2016.

[162] C. Feng, G. Deshpande, C. Liu, R. Gu, Y. J. Luo, and F. Krueger, “Diffusion of responsibility attenuates altruistic punishment: A functional magnetic resonance imaging effective connectivity study,” *Hum. Brain Mapp.*, vol. 37, no. 2, pp. 663–677, 2016.

[163] O. P. Hinds, N. Rajendran, J. R. Polimeni, J. C. Augustinack, G. Wiggins, L. L. Wald, H. Diana Rosas, A. Potthast, E. L. Schwartz, and B. Fischl, "Accurate prediction of V1 location from cortical folds in a surface coordinate system," *Neuroimage*, vol. 39, no. 4, pp. 1585–1599, 2008.

[164] M. Jenkinson, P. Bannister, M. Brady, and S. Smith, "Improved Optimization for the Robust and Accurate Linear Registration and Motion Correction of Brain Images," *Neuroimage*, vol. 17, no. 2, pp. 825–841, 2002.

[165] S. M. Smith, "Fast Robust Automated Brain Extraction," *Hum. Brain Mapp.*, vol. 17, pp. 143–155, 2002.

[166] M. W. Woolrich, B. D. Ripley, M. Brady, and S. M. Smith, "Temporal autocorrelation in univariate linear modeling of FMRI data.," *Neuroimage*, vol. 14, no. 6, pp. 1370–86, 2001.

[167] M. Balasubramanian, J. R. Polimeni, and E. L. Schwartz, "Near-isometric flattening of brain surfaces," *Neuroimage*, vol. 51, no. 2, pp. 694–703, 2010.

[168] U. Bürgel, T. Schormann, A. Schleicher, and K. Zilles, "Mapping of Histologically Identified Long Fiber Tracts in Human Cerebral Hemispheres to the MRI Volume of a Reference Brain: Position and Spatial Variability of the Optic Radiation," *Neuroimage*, vol. 10, no. 5, pp. 489–499, 1999.

[169] L. D. L. Selemon, A. Begovic, A. Begovic´, A. Begovic, A. Begovic´, and A. Begovic, "Stereologic analysis of the lateral geniculate nucleus of the thalamus in normal and schizophrenic subjects," *Psychiatry Res.*, vol. 151, no. 1–2, pp. 1–10, May 2007.

[170] J. Bolz, J. Bolz, C. D. Gilbert, and C. D. Gilbert, "Generation of end-inhibition in the visual

cortex via interlaminar connections.," *Nature*, vol. 320, no. 6060, pp. 362–365, 1986.

[171] P. C. Murphy, S. G. Duckett, and A. M. Sillito, "Feedback Connections to the Lateral Geniculate Nucleus and Cortical Response Properties," *Science (80-.).*, vol. 286, no. 5444, pp. 1552–1554, 1999.

[172] A. M. Sillito, J. Cudeiro, and H. E. Jones, "Always returning: feedback and sensory processing in visual cortex and thalamus," *Trends in Neurosciences*, vol. 29, no. 6. pp. 307–316, 2006.

[173] L. Spillmann, "Receptive fields of visual neurons: The early years," *Perception*, vol. 43, no. 11, pp. 1145–1176, 2014.

[174] G. Deshpande, K. Sathian, X. Hu, and J. a Buckhalt, "A rigorous approach for testing the constructionist hypotheses of brain function.," *Behav. Brain Sci.*, vol. 35, no. 3, pp. 148–9, 2012.

[175] G. Deshpande, X. Hu, R. Stilla, and K. Sathian, "Effective connectivity during haptic perception: A study using Granger causality analysis of functional magnetic resonance imaging data," *Neuroimage*, vol. 40, no. 4, pp. 1807–1814, 2008.

[176] C. W. J. Granger, "Investigating Causal Relations by Econometric Models and Cross-spectral Methods," *Econometrica*, vol. 37, no. 3, pp. 424–438, 1969.

[177] G. Deshpande, X. Hu, S. Lacey, R. Stilla, and K. Sathian, "Object familiarity modulates effective connectivity during haptic shape perception," *Neuroimage*, vol. 49, no. 3, pp. 1991–2000, 2010.

[178] B. M. Hampstead, A. Y. Stringer, R. F. Stilla, G. Deshpande, X. Hu, A. B. Moore, and K.

Sathian, “Activation and effective connectivity changes following explicit-memory training for face-name pairs in patients with mild cognitive impairment: a pilot study,” *Neurorehabil Neural Repair*, vol. 25, no. 3, pp. 210–222, 2011.

[179] S. Lacey, H. Hagtvedt, V. M. Patrick, A. Anderson, R. Stilla, G. Deshpande, X. Hu, J. R. Sato, S. Reddy, and K. Sathian, “Art for reward’s sake: Visual art recruits the ventral striatum,” *Neuroimage*, vol. 55, no. 1, pp. 420–433, 2011.

[180] F. Krueger, S. Landgraf, E. Van Der Meer, G. Deshpande, and X. Hu, “Effective connectivity of the multiplication network: A functional MRI and multivariate granger causality mapping study,” *Hum. Brain Mapp.*, vol. 32, no. 9, pp. 1419–1431, 2011.

[181] F. Preusse, van der Meer Elke, G. Deshpande, F. Krueger, and I. Wartenburger, “Fluid intelligence allows flexible recruitment of the parieto-frontal network in analogical reasoning.,” *Front. Hum. Neurosci.*, vol. 5, no. March, p. 22, 2011.

[182] K. Sathian, S. Lacey, R. Stilla, G. O. Gibson, G. Deshpande, X. Hu, S. LaConte, and C. Glielmi, “Dual pathways for haptic and visual perception of spatial and texture information,” *Neuroimage*, vol. 57, no. 2, pp. 462–475, 2011.

[183] M. Strenziok, F. Krueger, G. Deshpande, R. K. Lenroot, E. Van der meer, and J. Grafman, “Fronto-parietal regulation of media violence exposure in adolescents: A multi-method study,” *Soc. Cogn. Affect. Neurosci.*, vol. 6, no. 5, pp. 537–547, 2011.

[184] B. Gaschler-Markefski, F. Baumgart, C. Tempelmann, F. Schindler, D. Stiller, H. J. Heinze, and H. Scheich, “Statistical methods in functional magnetic resonance imaging with respect to nonstationary time-series: auditory cortex activity,” *Magn Reson Med*, vol. 38, no. 5, pp. 811–820, 1997.

[185] D. Kapogiannis, G. Deshpande, F. Krueger, M. P. Thornburg, and J. H. Grafman, “Brain networks shaping religious belief.,” *Brain Connect.*, vol. 4, no. 1, pp. 70–9, 2014.

[186] K. Sathian, G. Deshpande, and R. Stilla, “Neural changes with tactile learning reflect decision-level reweighting of perceptual readout.,” *J. Neurosci.*, vol. 33, no. 12, pp. 5387–98, 2013.

[187] M. M. Grant, D. White, J. Hadley, N. Hutcheson, R. Shelton, K. Sreenivasan, and G. Deshpande, “Early life trauma and directional brain connectivity within major depression,” *Hum. Brain Mapp.*, vol. 35, no. 9, pp. 4815–4826, 2014.

[188] M. D. Wheelock, K. R. Sreenivasan, K. H. Wood, L. W. Ver Hoef, G. Deshpande, and D. C. Knight, “Threat-related learning relies on distinct dorsal prefrontal cortex network connectivity,” *Neuroimage*, vol. 102, no. P2, pp. 904–912, 2014.

[189] S. Lacey, R. Stilla, K. Sreenivasan, G. Deshpande, and K. Sathian, “Spatial imagery in haptic shape perception,” *Neuropsychologia*, vol. 60, no. 1, pp. 144–158, 2014.

[190] M. M. Grant, K. Wood, K. Sreenivasan, M. Wheelock, D. White, J. Thomas, D. C. Knight, and G. Deshpande, “Influence of Early Life Stress on Intra- and Extra-Amygdaloid Causal Connectivity.,” *Neuropsychopharmacology*, vol. 40, no. 7, pp. 1–12, 2015.

[191] L. E. Libero, T. P. DeRamus, A. C. Lahti, G. Deshpande, and R. K. Kana, “Multimodal neuroimaging based classification of autism spectrum disorder using anatomical, neurochemical, and white matter correlates,” *Cortex*, vol. 66, pp. 46–59, 2015.

[192] N. L. Hutcheson, K. R. Sreenivasan, G. Deshpande, M. A. Reid, J. Hadley, D. M. White, L. Ver Hoef, and A. C. Lahti, “Effective connectivity during episodic memory retrieval in

schizophrenia participants before and after antipsychotic medication," *Hum. Brain Mapp.*, vol. 36, no. 4, pp. 1442–1457, 2015.

[193] C. Büchel and K. J. Friston, "Dynamic changes in effective connectivity characterized by variable parameter regression and Kalman filtering," in *Human Brain Mapping*, 1998, vol. 6, no. 5–6, pp. 403–408.

[194] M. Arnold, W. H. R. Miltner, H. Witte, R. Bauer, and C. Braun, "Adaptive AR modeling of nonstationary time series by means of kaiman filtering," *IEEE Trans. Biomed. Eng.*, vol. 45, no. 5, pp. 545–552, 1998.

[195] S. Ryali, T. Chen, K. Supekar, T. Tu, J. Kochlka, W. Cai, and V. Menon, "Multivariate dynamical systems-based estimation of causal brain interactions in fMRI: Group-level validation using benchmark data, neurophysiological models and human connectome project data," *J. Neurosci. Methods*, vol. 268, pp. 142–53, Aug. 2016.

[196] S. Ryali, Y. Y. I. Shih, T. Chen, J. Kochalka, D. Albaugh, Z. Fang, K. Supekar, J. H. Lee, and V. Menon, "Combining optogenetic stimulation and fMRI to validate a multivariate dynamical systems model for estimating causal brain interactions," *Neuroimage*, vol. 132, pp. 398–405, May 2016.

[197] S. Ryali, K. Supekar, T. Chen, and V. Menon, "Multivariate dynamical systems models for estimating causal interactions in fMRI," *Neuroimage*, vol. 54, no. 2, pp. 807–823, Jan. 2011.

[198] K. Goodyear, R. Parasuraman, S. Chernyak, E. de Visser, P. Madhavan, G. Deshpande, and F. Krueger, "An fMRI and effective connectivity study investigating miss errors during advice utilization from human and machine agents," *Soc. Neurosci.*, pp. 1–12, Jul. 2016.

[199] S. O. Dumoulin and B. A. Wandell, “Population receptive field estimates in human visual cortex,” 2007.

[200] J. C. Horton and H. Sherk, “Receptive field properties in the cat’s lateral geniculate nucleus in the absence of on-center retinal input.,” *J. Neurosci.*, vol. 4, no. 2, pp. 374–380, 1984.

[201] K. L. Grieve and A. M. Sillito, “The length summation properties of layer VI cells in the visual cortex and hypercomplex cell end zone inhibition.,” *Exp. brain Res.*, vol. 84, no. 2, pp. 319–25, 1991.

[202] J. Bolz, J. Bolz, C. D. Gilbert, and C. D. Gilbert, “Generation of end-inhibition in the visual cortex via interlaminar connections.,” *Nature*, vol. 320, no. 6060, pp. 362–365, 1986.

[203] W. Chen and X. H. Zhu, “Correlation of activation sizes between lateral geniculate nucleus and primary visual cortex in humans,” *Magn. Reson. Med.*, vol. 45, no. 2, pp. 202–205, 2001.

[204] K. A. Schneider and S. Kastner, “Effects of sustained spatial attention in the human lateral geniculate nucleus and superior colliculus,” *J Neurosci*, vol. 29, no. 6, pp. 1784–1795, 2009.

[205] K. A. Schneider, “Subcortical mechanisms of feature-based attention.,” *J. Neurosci.*, vol. 31, pp. 8643–8653, 2011.

[206] K. Uğurbil, X. Hu, W. Chen, X. H. Zhu, S. G. Kim, and A. Georgopoulos, “Functional mapping in the human brain using high magnetic fields.,” *Philos. Trans. R. Soc. Lond. B. Biol. Sci.*, vol. 354, no. 1387, pp. 1195–213, 1999.

[207] K. Wunderlich, K. A. Schneider, and S. Kastner, “Neural correlates of binocular rivalry in the human lateral geniculate nucleus.,” *Nat. Neurosci.*, vol. 8, no. 11, pp. 1595–602, 2005.

[208] K. A. Schneider, M. C. Richter, and S. Kastner, “Retinotopic organization and functional subdivisions of the human lateral geniculate nucleus: A high-resolution functional magnetic resonance imaging study,” *J. Neurosci.*, vol. 24, no. 41, pp. 8975–8985, 2004.

[209] D. H. F. Chang, R. F. Hess, and K. T. Mullen, “Color responses and their adaptation in human superior colliculus and lateral geniculate nucleus,” *Neuroimage*, vol. 138, pp. 211–220, 2016.

[210] P. Zhang, W. Wen, X. Sun, and S. He, “Selective reduction of fMRI responses to transient achromatic stimuli in the magnocellular layers of the LGN and the superficial layer of the SC of early glaucoma patients.,” *Hum. Brain Mapp.*, vol. 37, no. 2, pp. 558–69, Feb. 2016.

[211] P. Li, C.-H. Jin, S. Jiang, M.-M. Li, Z.-L. Wang, H. Zhu, C.-Y. Chen, and T.-M. Hua, “Effects of surround suppression on response adaptation of V1 neurons to visual stimuli.,” *Dongwuxue. Yanjiu.*, vol. 35, no. 5, pp. 411–9, Sep. 2014.

[212] T. J. Andrews, S. D. Halpern, and D. Purves, “Correlated size variations in human visual cortex, lateral geniculate nucleus, and optic tract.,” *J. Neurosci.*, vol. 17, no. 8, pp. 2859–2868, 1997.

[213] S. Kyathanahally, A. Franco-Watkins, X. Zhang, V. Calhoun, and G. Deshpande, “A realistic framework for investigating decision-making in the brain with high spatio-temporal resolution using simultaneous EEG/fMRI and joint ICA,” *IEEE J. Biomed. Heal. Informatics*, vol. 2194, no. c, pp. 1–1, Jul. 2016.